Schriftenreihe des Energie-Forschungszentrums Niedersachsen

efzn
Energie-Forschungszentrum
Niedersachsen

TU Clausthal

Rotor Angle Stability of Multiconverter Based Autonomous Microgrid with 100% VISMA Control

Kamilu Alabi Sanusi

Promotion an der Technischen Universität Clausthal

Band 84

Cuvillier Verlag Göttingen

Rotor Angle Stability of Multiconverter Based Autonomous Microgrid with 100% VISMA Control

Rotor Angle Stability of Multiconverter Based Autonomous Microgrid with 100% VISMA Control

Dissertation

To be awarded the degree

Doctor of Engineering (Dr.-Ing.)

submitted by

Kamilu Alabi Sanusi, M.Engr.

approved by the Faculty of Energy and Economic sciences at Clausthal University of Technology.

Date of the oral examination
20.09.2024

Dean

Prof. Dr. rer. pol. Ingeborg Wulf

Chairperson of the Board of Examiners
Prof. Dr. mont. Dr. rer. nat. Michael J. Fischlschweiger

Supervising tutor
Prof. Dr.-Ing. Hans-Peter Beck

Reviewer
Prof. Dr. rer. nat. Marc Timme, TU Dresden

Bibliographical information held by the German National Library

The German National Library has listed this book in the Deutsche Nationalbibliografie (German national bibliography); detailed bibliographic information is available online at http://dnb.d-nb.de.

1st edition - Göttingen: Cuvillier, 2024

Also in: (TU) Clausthal, Univ., 2024

Nonnenstieg 8, 37075 Göttingen

Telephone: +49 (0)551-54724-0

Telefax: +49 (0)551-54724-21

www.cuvillier.de

Dieses Dokument unterliegt der Lizenz Open Access CC BY 4.0

Diese Veröffentlichung wurde aus Mitteln des Publikationsfonds Niedersachsen-Open, gefördert aus zukunft.niedersachsen, unterstützt

1st edition, 2024

This publication is printed on acid-free paper.

ISBN 978-3-68952-855-3

eISBN 978-3-68952-856-0

"The strong is not the one who overcomes the people by his strength, but the strong is the one who controls himself while in anger." [Bukhari:6114]

"Make things easy for the people, and do not make it difficult for them, and make them calm (with glad tidings) and do not repulse (them)." [Bukhari:6125]

ABSTRACT

Autonomous microgrids are known to lack appropriate inertia and damping for grid stabilization. Due to this, a virtual synchronous machine (VISMA) has been introduced to provide necessary ancillary services through the control of power converters. In a multi-VISMA (*n*-VISMA) microgrid, relative rotor angle stability of the power system is dependent on the active power balance after a small perturbation. Using relevant analytical models is an essential issue for microgrid stability analysis. In this PhD dissertation, a comprehensive small-signal stability analysis to study the inherent electromechanical oscillations in the virtual rotors is presented. The subsystems of the microgrid consisting of VISMAs, network, loads and the outer power controller were all modelled in Synchronously-rotating Reference Frame. The small-signal model was tested on IEEE-9 bus system with VISMA replacing the electromechanical synchronous machines on the network. To validate the developed numerical analytics, dynamic responses of the small-signal model are compared with those of the nonlinear system dynamics and the results reveal that the developed linearized small-signal model is sufficient to accurately characterize behaviour of the VISMA microgrid when operated in autonomous mode. Eigenvalues analysis and parameter sensitivities of the critical modes were investigated. Oscillatory participations of the VISMAs and steady state stability limit of the microgrid have also been investigated.

However, before starting the stability analysis of the multiconverter based power system with VISMA control, it is necessary to obtain the steady-state operating points (SSOPs) of all dynamic nodes in the network. Modified traditional iterative schemes using the concept of droop bus technique in an islanded microgrid are not feasible for load flow analysis of VISMA microgrid incorporating non-control dynamics. This dissertation thus proposes a closed-form steady-state, fundamental-frequency models for autonomous/islanded VISMA microgrid using the concept of *virtual swing bus*. In this technique, the virtual internal buses of all VISMAs in the network are governed by the swing equation. The voltage at all buses is variable except the virtual buses in which the pole wheel voltages are prespecified. The algorithm was extended by a droop control localized to each VISMA. The suitability of the proposed algorithm to obtain SSOPs of VISMA was tested on IEEE-9 bus system with VISMA replacing electromechanical synchronous machines and also on a 2-VISMA low voltage distribution system. To validate the applicability of the proposed algorithm and prove its accuracy, the case study systems were also modeled in the

SIMULINK environment for detailed time domain analysis. The algorithm was found to be computationally effective for a load flow analysis of the VISMA microgrid. The results also reveal that the addition of external droop control improves the frequency stability of the system.

Kurzfassung

Es ist bekannt, dass einem autonomen Mikronetz eine angemessene Trägheit und Dämpfung zur Netzstabilisierung fehlt. Aus diesem Grund wurde die virtuelle Synchronmaschine (VISMA) eingeführt, um die erforderlichen Hilfsdienste durch die Steuerung von Stromrichtern bereitzustellen. In einem Multi-VISMA (*n*-VISMA) -Mikronetz hängt die relative Rotorwinkelstabilität des Stromnetzes von der Wirkleistungsbilanz nach einer kleinen Störung ab. Die Verwendung relevanter analytischer Modelle ist für die Stabilitätsanalyse von Mikronetzen unerlässlich. In dieser Dissertation wird eine umfassende Kleinsignal-Stabilitätsanalyse zur Untersuchung der inhärenten elektromechanischen Schwingungen in den virtuellen Rotoren vorgestellt. Die Teilsysteme des Mikronetzes, bestehend aus den VISMAs, dem Netz, den Lasten und dem äußeren Leistungsregler, wurden alle in einem synchron rotierenden Referenzrahmen modelliert. Das Kleinsignalmodell wurde auf einem IEEE-9-Bussystem getestet, wobei VISMA die elektromechanischen Synchronmaschinen im Netz ersetzten. Zur Validierung der entwickelten numerischen Analyse werden die dynamischen Reaktionen des Kleinsignalmodells mit denen der nichtlinearen Systemdynamik verglichen. Die Ergebnisse zeigen, dass das entwickelte linearisierte Kleinsignalmodell ausreicht, um das Verhalten des VISMA-Mikronetzes beim Betrieb im autonomen Modus genau zu charakterisieren. Die Eigenwertanalyse und die Parameterempfindlichkeiten der kritischen Modi wurden untersucht. Die Oszillationsbeteiligung der VISMAs und die Stabilitätsgrenze des Mikronetzes im eingeschwungenen Zustand wurden ebenfalls untersucht. Bevor jedoch die Stabilitätsanalyse des auf einem Multi-Umrichter basierenden Stromnetzes mit VISMA-Steuerung beginnt, müssen die stationären Betriebspunkte (SSOPs) aller dynamischen Knoten im Netz ermittelt werden. Modifizierte herkömmliche iterative Verfahren, die das Konzept der Pufferbus-Technik in einem Insel-Mikronetz verwenden, sind für die Lastflussanalyse eines VISMA-Mikronetzes mit ungeregelter Dynamik nicht praktikabel. In dieser Dissertation wird daher ein stationäres Grundfrequenzmodell in geschlossener Form für ein autonomes/inselnahes VISMA-Mikronetz vorgeschlagen, das das Konzept des virtuellen Pendelbusses verwendet. Bei dieser Technik werden die virtuellen internen Busse aller VISMAs im Netz durch die Swing-Gleichung geregelt. Die Spannung an allen Bussen ist variabel, mit Ausnahme der virtuellen Busse, bei denen die Polradspannungen vorgegeben sind. Der Algorithmus wurde um eine Pufferregelung erweitert, die für jede VISMA lokalisiert ist. Die Eignung des vorgeschlagenen Algorithmus zur Ermittlung der SSOPs von VISMA wurde an einem

IEEE-9-Bus-System mit VISMA als Ersatz für elektromechanische Synchronmaschinen sowie an einem 2-VISMA-Niederspannungsverteilungssystem getestet. Um die Anwendbarkeit des vorgeschlagenen Algorithmus zu validieren und seine Genauigkeit zu beweisen, wurden die Fallstudiensysteme auch in der SIMULINK-Umgebung für eine detaillierte Zeitbereichsanalyse modelliert. Der Algorithmus erwies sich als rechnerisch effizient für eine Lastflussanalyse des VISMA-Mikronetzes. Die Ergebnisse zeigen auch, dass die Hinzufügung einer externen Pufferregelung die Frequenzstabilität des Systems verbessert.

Übersetzt mit DeepL.com (kostenlose Version).

Table of Contents

List of Figures

List of Tables

Formula Symbols and Abbreviations

AVR	Automatic voltage regulator
BFS	Backward/forward sweep
CPL	Constant power load
CPL_droop	Constant power load for droop control extended algorithm
CVSM	Cascaded virtual synchronous machine
CZL	Constant impedance load
CZL_droop	Constant impedance load for droop control extended algorithm
DDSRF	Double-decoupled-synchronous-reference-frame
DER	Distributed energy resources
DFIG	Doubly fed induction generator
DG	Distributed generator
ESM	Electromechanical synchronous machine
GFL	Grid following inverter
GFM	Grid forming inverter
HV	High voltage
IBG	Inverter Based Generation
IEE	Institut für Elektrische Energietechnik und Energiesysteme
IEEE	Institute of Electrical Electronics Engineering
IGBT	Insulated gate bipolar transistor
IM	Islanded microgrid
IMNR	Improved Modified Newton-Raphson
KHI	Kawasaki heavy industry

LPF	Low pass filter
LS	Linearized small-signal
LV	Low voltage
NL	Non-linear
PCC	Point of common coupling
PF	Participation factor
PI	Proportional controller
PLC	Power loop controller
PLL	Phase locked loop
PSO	Power system operators
PWM	Pulse width modulation
PZ-map	Pole-zero map
RE	Renewable energy
RHS	Right hand side
SIV-VISMA	Simplified Current–Voltage abc VISMA
SPC	Synchronous power controller
SPC-CND	Synchronous power controller-configurable natural droop
SPC-PI	Synchronous power controller- proportional controller
SPC-SG	Synchronous power controller-synchronous generator
SRF	Synchronously-rotating reference frame
SSOP	Steady state operating point
SVI-VISMA	Simplified Voltage–Current abc VISMA
VISMA	Virtual synchronous machine
VSG	Virtual synchronous generator

VSYNC	Virtual synchronous control
WECC	Western Electricity Coordinating Council

1 Introduction

1.1 Background of the study

Energiewende is a political statement initiated by the German national government with the objective of reducing the problems caused by the traditional energy systems in the area of ecological, social and health challenges. For many decades renewable energy (RE) has been seen as the preferred alternative to energy independence by every nation of the world [1]. *Energiewende* enhances the nation's economy by fully internalising the possible expenditure on the external costs. The ongoing war between Russia and Ukraine has further consolidated on the need to reduce energy imports, the effects on the German economy would have been much more devastating if not the massive progress that has been achieved in renewable energy integration.

According to [2], renewable energy productive capacity grew by 17 GW in 2023 to an aggregate of just below 170 GW. This implies a year-on-year growth of 12% which is largely dominated by both solar and wind. These two sources are in the forefront of replacing the conventional synchronous generation. Germany's growth in solar capacity in 2023 amounted to 14.1 GW, nearly double that in the year 2022. This was exclusively due to personalized ground-mounted and commercially installed rooftop solar capacity. Bavaria had the highest number of solar capacity in 2023, with 3.5 GW. At the end of 2023, installed solar capacity in Germany totalled 81.7 GW. This shows that 19 GW of fresh productive capacity will be required each year from now on if the goal of reaching 215 GW is to be met by the year 2030, please see Fig. 1.1 for the projection of solar power generation in Germany. In the wind energy technology, growth in onshore wind capacity in 2023 was 2.9 GW higher than in the previous year. Figure 1.2 comprises new capacity put into operation minus the capacity taken out of operation. Installed onshore wind capacity totalled 60.9 GW at the end of 2023. The target for 2030 is 115 GW of installed capacity. Germany will need 7.7 GW of new capacity each year to meet this target. Figure 1.2 illustrates the projection of wind energy installation (both for onshore and offshore).

The share of RE generation has risen from 24.7% to 54.9% of the net electricity generation between year 2013 and the year 2023, representing a significance boost and total commitment of German government in achieving self-sustenance in the energy sector.

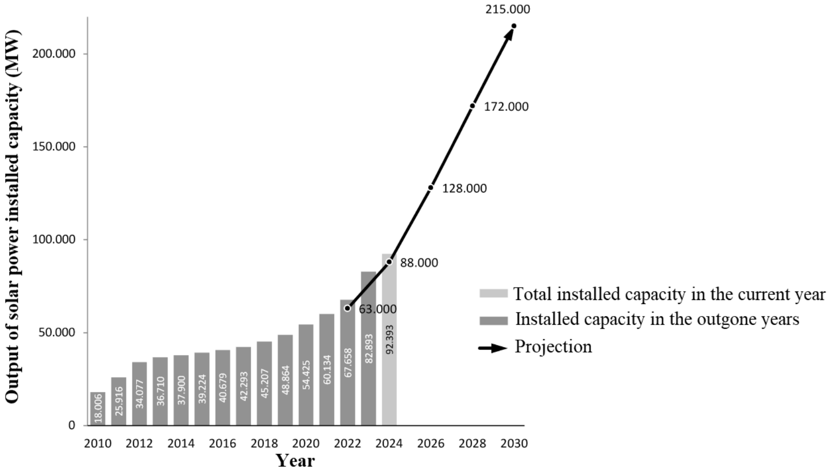

Figure 1.1. Solar power generation capacity in Germany [3]

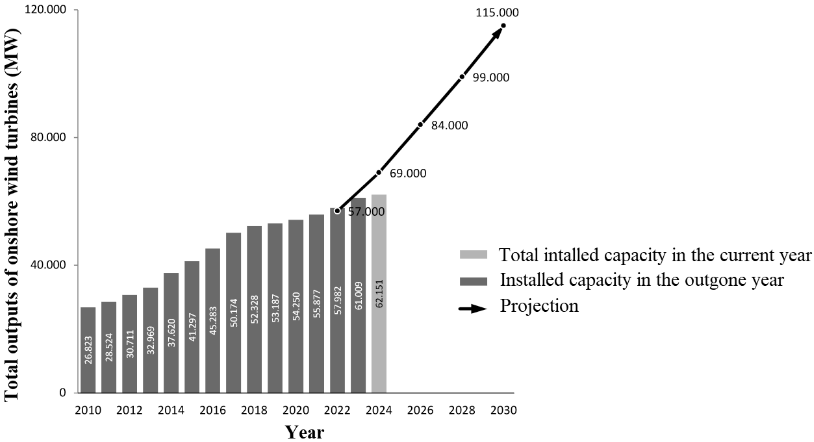

Figure 1.2. Onshore wind power generation capacity in Germany [3]

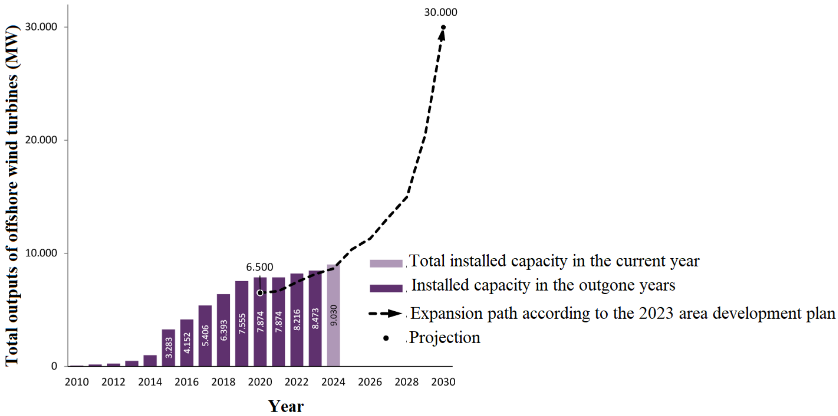

Figure 1.3. Offshore wind power generation capacity in Germany [3]

Fig. 1.4 illustrates the share of renewable energies in total net electricity generation between 1990 and 2023, the fell in the year 2021 was as a result of weather situation. It is evident from Figures 1.1-1.4 that renewable generation will continue to rise exponentially while it is expected that the fossil-fuel type will continue to be depleted year in year out. Before the introduction of RE into power grids, electromechanical synchronous machine (ESM) rules the domain of electrical power generation devices, they are characterized with the ability to provide excellent inertia and damping responses which guarantee stability of the grid frequency and regulate the power imbalance in the system [4, 5]. Due to the progressive development in renewable energy integration into the grid and the strong determination to have 100% inverter based generation (IBG) in the near future, there have been remarkable achievements in the control algorithm development for the interface power converters, the famous of which is the droop control [6].

Droop controls are decentralized control schemes and are suitable for both grid and isolated operations [7]. In the grid connected inverter, they are implemented to regulate the exchange of active and reactive power with the utility, in order to keep the grid voltage amplitude and frequency within a normal range. In the autonomous mode, the droop control-based inverters can provide voltage support and share load power according to their power ratings. . They do not require communication control lines, they are reliable and highly responsive, and are very suitable in both grid and isolated operations [7]. Despite the wide acceptability of droop control, it suffers from inertia issues and thus cannot ensure system frequency stability during disturbances. Inadequate reactive power sharing, sensitivity to faults and poor voltage regulations are other issues associated with droop control microgrids [8-10].

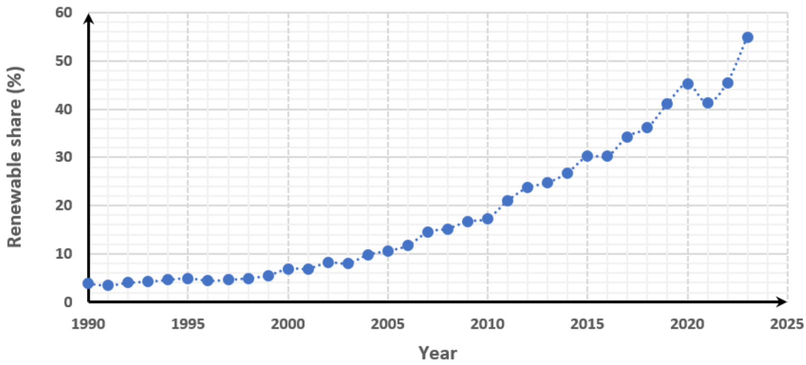

Figure 1.4. Share of renewable energies in total net electricity generation [11]

An electrical power system with zero inertia is unstable, experiences power quality issues, and is vulnerable to blackouts [12]. If there is a change in load demand, then the system frequency also tends to change. The frequency fluctuations can be mitigated by the presence of sufficient rotating masses on the grid, which act like a shock absorber. Therefore, the increasing penetration level of distributed energy resources (DER) will have enormous effects on the dynamic response and power system stability [13]. Examples of the most recent power system instability scenarios are those of South Australian Black out which occurred on the 28th of September, 2016 [14] and that of the European continental power failure that occurred on the 8th of January, 2021 [15]. Heterogeneous frequency traces seen as a result of the European continental power failure are shown in Fig. 1.5.

In order to provide ancillary services needed by the distributed generators (DGs) for a stable operation of power systems, **Vi**rtual **S**ynchronous **Ma**chines (VISMA) technology, also called **V**irtual **S**ynchronous **G**enerator (VSG) [16] has been proposed in the literature as a suitable idea for controlling inverters by mimicking the behaviour of conventional ESM [17]. Generally, VISMA have the capability to reproduce the static and dynamic properties of ESM on a power electronic interface converter faster. VISMA is a special controlled inverter that is able to integrate different forms of RE sources into the grid, this is shown by the elementary structure shown in Fig. 1.6.

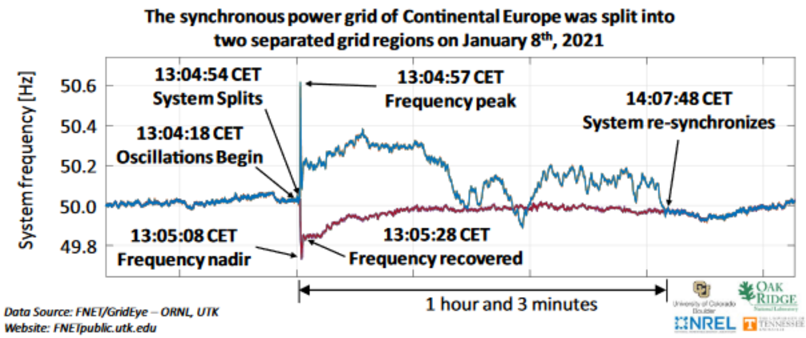

Figure 1.5. Frequency traces of the European synchronized continental power network failure [15]

Some of the important features of VISMA are i) ability to initiate inertia response to resist change in grid frequency ii) ability to effectively damp out rotor oscillations during disturbances, thereby improving transient stability iii) ability to independently and bidirectionally control the active and reactive power at the grid. The fundamental concept of VISMA technology is the simulation of an ESM on the basis of an inverter in combination with an energy storage unit and a microcomputing unit for determining the electrical, magnetic and mechanical machine parameters using a mathematical representation of synchronous generator in real time.

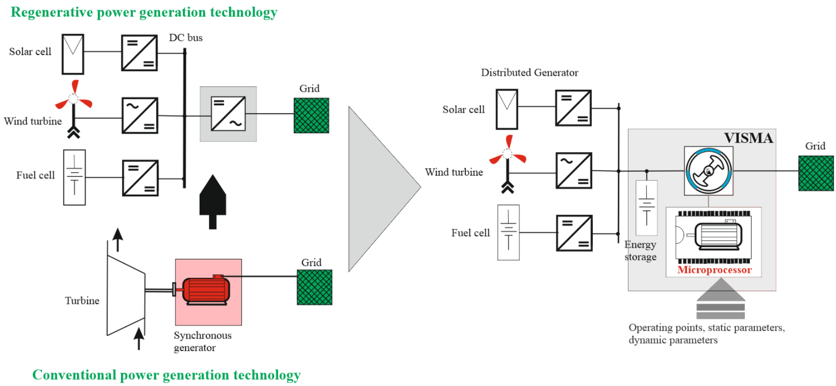

Figure 1.6. Basic structure of VISMA [18]

1.2 Power system stability category

The evolution of smart grids over the past two decades has posed several technical challenges to the power system operations. New instability scenarios now appear in the power system, and according to reports, the most prevalent are the low-frequency oscillations that occur due

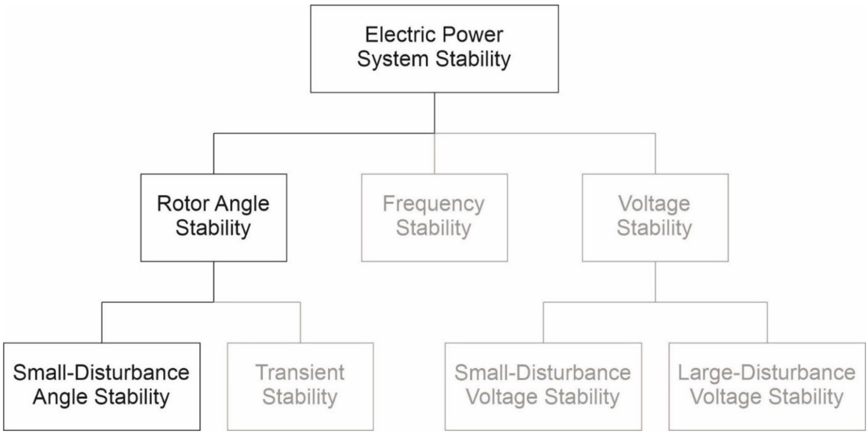

Figure 1.7. Classifications of power system stability [19]

to weak grid. Depending on the network configuration, circumstances surrounding the system operation, nature of disturbances and time lapse of fault, varieties of instabilities may evolve. Power system stability is basically categorized into rotor angle stability, frequency stability and voltage stability, [16, 20-24], and it is schematically represented in Fig. 1.7. A detailed explanation of each category and sub-category of power system stability is provided in Ref. [19].

1.3 Motivation and research objectives

Due to the deep structural transformation of the global energy sector from the well-known centralized generation to now decarbonized, digitalized and decentralized power systems, it is necessary that power equilibrium is maintained between generation and load if the grid frequency is to be kept within the acceptable stability margins. When the grid voltage is affected by a perturbation, such as imbalances, transients, or harmonics, which is normal in power grids, conventional grid inverters find it difficult to remain appropriately synchronized with the grid voltage [25]. Power mismatches can lead to uncontrolled power flows which may result in severe fluctuations in frequency and voltage amplitude, thereby negatively impacting grid stability [8, 10]. Grid stability is a paramount issue in power system operations, it has a crucial role to ensuring a safe, reliable and optimal operation of high order multivariable modern power system whose dynamic response is dictated by several components with distinctive properties. To allow seamless deployment of inverter-based generation and meet stringent demand of the power system operators (PSO), the overall performance of the electrical power system needs to be enhanced by providing solutions to dynamic stability and control challenges. The deployment of novel technologies and controls has led to several questions being asked regarding the microgrid responses to perturbations [13, 26]. In a multi-VISMA (*n*-VISMA) microgrid, the ability to re-establish balance between the opposing forces is ensured by the rotor angle stability of each VISMA. Rotor angle stability is the ability of the VISMA to remain in synchronism with the network after being subjected to disturbance caused by torque imbalances in the system. Stable synchronized operation of VISMA rotor angles is thus a critical stability problem for a secured microgrid. According to Fig. 1.7, angle stability is categorized into a small-disturbance and large disturbance stability. Stability analysis in traditional power grids is long-established using the classical models of ESM, speed-governors and the excitation systems of different orders designed to solve a specific kind of problem. In the modern inverter-based power grid with high level of distributed energy resources, there is no specific analytical standard because of different control strategies/synthesis which are continuously evolving. Different VSGs require different computational models to understand the interactions between different units in the microgrid system.

This dissertation aims to consider a special case of *n*-VISMA microgrid in autonomous operation with a specific focus on *small-disturbance rotor angle stability.* If the rotor oscillation as a result of a perturbation is not resolved in due time, it can lead to severe damage of the power plant [27]. For traditional power systems, synchronization dominated by rotor motions occurs in a physical sense. However, in the VISMA based microgrid, synchronization between VISMAs corresponds to their virtual rotor vectors and it is necessary that the transient induced in the network following a small perturbation is damped out such that their kinetic energy is dissipated within a relatively short period. All the VISMAs in the network must at the same time regain their identical speed. In a network of *n*-VISMA, a synchronous state is described in equation (1.1) [28].

$$\dot{\delta}_1 = \dot{\delta}_2 \ldots.\ldots\ldots. = \dot{\delta}_n = w_s \tag{1.1}$$

Where δ, is the load angle and w_s, is the synchronous speed.

1.4 Research contribution

Since 2007, different topologies of VSG controls have been proposed [29] and many are still continuously evolving. Due to these different control strategies, small-signal stability analysis techniques also differ. After extensive review of literature, it was found that most of the stability analysis scenarios of VSG control converters are based on a single machine grid-connected system or sometimes on multimachine model under mixed configurations involving both synchronous generators and inverted systems [30, 31]. Studies of general multi-VSG systems with 100% power electronic devices are rare. In addition, not much work has been done on the stability analysis (either small-signal or large signal) of VISMA model from IEE TU-Clausthal, Germany, and the most recent work by [32, 33] was carried out at system level. The traditional VISMA model presented in [29] does not incorporate outer power controllers, the active and reactive power regulations were respectively achieved by setting the model parameters virtual torque and virtual excitation as it was similarly done in [34]. Also, most of the stability analytical model of VSG control schemes are cumbersome and computationally intensive like that developed by [35] for a single machine which may not be easily realizable for multimachine analysis. Those models that are simpler are not suitable for operation in autonomous mode. The contributions of this thesis are summarized as follows:

1. Full flexibility of operation is achieved by adding a two-loop power controller localized to each VISMA on the grid. The automatic voltage regulator (AVR) in closed loop form ensures that the adjusted pole wheel voltage based on system operating conditions (E_{po}^{*}) is kept equal to the VISMA voltage set-point (E_0). The control structure makes it possible to set the respective ancillary services in a desired manner as shown in Fig. 6.1. In the multi-VISMA microgrid presented, each VISMA unit is designed to have an independent control so that fundamental, active and reactive powers can be shared based on individualized static droop coefficients.
2. New approach into small-signal synchronous stability of multi-VISMA microgrid system in the absence of an infinitely swing bus.
3. A novel closed-form steady-state, fundamental-frequency model for an autonomous/islanded VISMA microgrid using the concept of *virtual swing bus* was developed to obtain the stationary operating points of all the dynamic nodes in the system. This proposed concept employs the use of constant amplitude of virtual excitation and virtual torque localized to each VISMA unlike the droop bus approach that uses active and reactive power coefficients as major constant control parameters.
4. Eigenvalues and parametric sensitivities stability analysis of multi-VISMA system.

1.5 Thesis outline

This dissertation is structured as follows:

Chapter 1 presents the general background on the study, motivation and objectives of the research and major contributions of the study. Chapter 2 provides a review about different kinds of grid inertia control system available in literature. A more comprehensive analytical detail regarding the sub-units of abc simplified VISMA control technology invented by TU-Clausthal, Germany is also presented. Per-unitization of analytical variables is also highlighted. In Chapter 3, relevant mathematical tools necessary for the stability analysis of modern power systems are presented with special focus on selective modal analysis, transition matrix and linearized small-signal model. Chapter 4 discusses a closed-form steady-state, fundamental-frequency model for islanded/autonomous VISMA microgrid using the concept of virtual swing bus. In Chapter 5, linearized small-signal rotor angle stability of uncontrolled multi-VISMAs in autonomous operation is presented while Chapter 6 investigates rotor angle stability of multi-virtual synchronous machines with an outer active power loop controller (PLC). A summary of the key findings and suggested recommendations follows in Chapter 7.

2 VISMA and other Variants of Virtual Inertia Control Technologies

2.1 Introduction

The responsive nature of a power electronic interface converter to grid disturbances is dependent on its control configurations. The control scheme is responsible for monitoring and balancing of the generated power, output voltage, frequency with their corresponding set points [36]. Conventionally, two major classes of controls have been proposed for the grid connected converter and these are; grid following (GFL) and grid forming converters (GFM). GFL converters synchronize with the grid by means of phase locked loop (PLL), which always tracks the grid voltage and its angle to inject or absorb active or reactive power from the grid [37]. GFL are characterized with a highly responsive current control loop and as such they are treated as controlled current source inverter [38]. GFM behave in a similar version like conventional synchronous machines and are often called voltage-controlled source inverters. GFL do not have the capability to provide instantaneous grid support services, such as inertia, voltage regulation, and frequency response, especially during disturbances [37]. This chapter is devoted to providing details of different kinds of grid inertia control systems that are prominent in literature as illustrated in Fig. 2.1. A more detailed analytical model necessary for the stability of VISMA control technology proposed by TU-Clausthal, Germany is further presented. Per-unitization of analytical variables is also presented.

2.2 Per-unitization

To simplify analysis and facilitate comparison among the inverters on the microgrid in relation to the loads and transmission lines, the entire system investigation is carried out in per unit. The base values are generally real numbers and angles are represented in their normal standard units of rad or degree [39], [40]. In the per-unitization of system variables, it is necessary that a single base power S_{base}, is selected for the complete system not minding whether some sections of the power systems are magnetically coupled through transformers or not. The base quantities are defined as follows:

Rated voltage (line-line, RMS) $= U_b$ (KV)

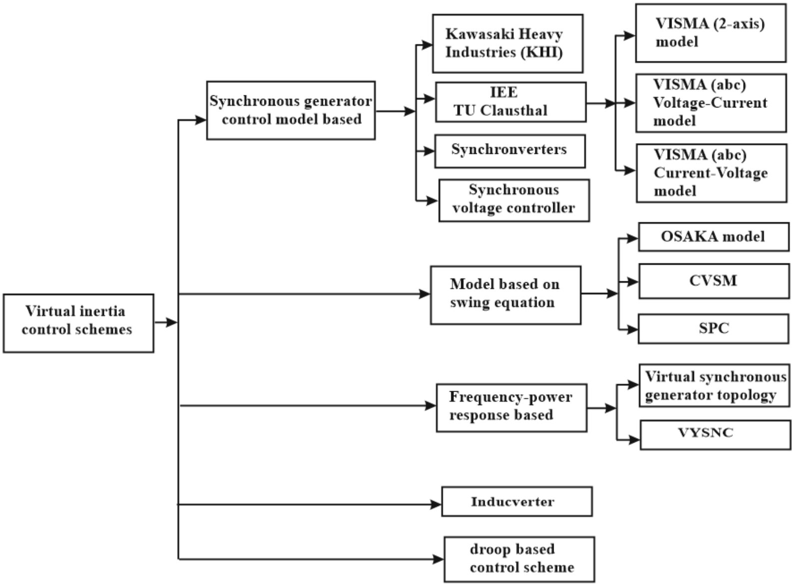

Figure 2.1. Virtual Inertia Control Topologies, modified from reference [41]

Rated power = S_b (MVA)

Rated frequency = f_b (Hz)

Base angular frequency $w_b = 2 * \pi * f_b$ (elect.rad/sec)

Base impedance $Z_b = \frac{U_b^2}{S_b}$ (Ω)

Base inductance $L_b = \frac{Z_b}{w_b}$ (Henry)

Per unit inductance $L_{pu} = \frac{Actual\ inductance\ L_a\ (Henry)}{L_b}$

Base capacitance $C_b = \frac{1}{Z_b w_b}$ (Farad)

Per unit capacitance $C_{pu} = \frac{Actual\ inductance\ C_a\ (Farad)}{C_b}$

Active and reactive powers P and Q in per unit, $P_{pu}\ or\ Q_{pu} = \frac{Actual\ P\ or\ Q\ in\ MW}{S_b(MVA)}$

Base torque $T_b = \frac{S_b(W)}{w_b}$ *(Watt/(rad/sec) or Nm)*

Base damping coefficient $K_{d,b} = \frac{T_b}{w_b}$ (*Nm*/(*rad/sec*))

Damping coefficient in per unit = $K_{d,pu} = \frac{Damping\ in\ SI\ units\ of\ (Nm/(rad/sec))}{K_{d,b}}$

The quantity H normalized to the VA base of that particular machine is defined as

Virtual inertia; $H_{mach} = \frac{stored\ kinetic\ enegy\ at\ rated\ synchronous\ speed\ (MW.s)\ or\ Joule}{S_b(MW)}$ [39]

However, this inertia has to be revised for use when dealing with system studies by transforming from the individual machine VA base to the system VA base. This is computed as follows [42]:

$$H_{sys} = H_{mach}\left(\frac{S_{B3mach}}{S_{B3sys}}\right)\ \text{sec}$$

Where $\mathrm{H_{mach,sys}}$ = individual machine inertia on the system base

$\mathrm{S_{B3mach}}$ = Three phase VA base of the particular machine

$\mathrm{S_{B3sys}}$ = Three phase VA base of the entire system

Static droop factors m_p and m_q are calculated in per-unit values as follows:

$$m_{p,pu} = m_p \frac{S_b}{w_b}$$

$$m_{q,pu} = m_q \frac{S_b}{U_b}$$

2.3 VISMA models

VISMA is a specially controlled inverter that can serve as a grid connection element for various electrical direct current sources. It enables the inverter to mimic the behaviour of an electromechanical synchronous machine (ESM) on the grid. The objective is to maintain the electrical power quality despite increasing number of decentralized energy producers. The properties of a VISMA are essentially dependent on the machine model implemented in it, which simulates the operating behaviour of a synchronous machine in real time at a given voltage and then specifies the reference value of the impressed multiphase alternating current for the inverter control [18]. The maiden VISMA [17] was modelled using two axis d-q coordinate system of the ESM. This model has the disadvantages of requiring high computing efforts for the real time solution of differential equation which increases efforts for implementation and programming. The optimization of all machine parameters is a time-consuming task due to the non-linear coupling of the equations. This time behaviour characteristics impacts on the overall operating dynamics of the VISMA. The simplified models named SVI-VISMA and SIV-VISMA were modelled in *abc* stationary coordinate system [20]. The two simplified models have the following generic advantages; fewer parameters and easier adjustment of the parameters, less computational effort, robustness against asymmetrical mains voltages, direct coupling with the measured mains voltage signals without additional filtering, and weaker coupling between active and reactive power setting [18]. However, the major difference between SVI-VISMA and SIV-VISMA is that the former is a voltage-current model while the latter is a current-voltage model. SIV-VISMA is an inverse model of SVI-VISMA which often requires the need to use a differentiator and could lead to an instability (the use of differentiator makes the model vulnerable to amplifying noises and harmonics). Though a low pass filter (LPF) has been recommended to serve as an interface between the grid measurement and the machine model, it does have undesirable consequences on the general dynamic behaviour of the system including the bandwidth of the controller [43]. The schematic representations of SVI-VISMA and SIV-VISMA are combined in Fig. 2.2, these two VISMA models are deployable to operate in either grid connected or autonomous mode and they can ensure active and reactive power sharing in a similar fashion as droop controlled microgrid [21]. Based on this model, v_{abc}^* is the reference voltage generated from grid current i_{abc} while i_{abc}^* is the VISMA output current generated from grid voltage v_{abc}.

Figure 2.2. Simplified VISMA configuration based on current–voltage (voltage–current) model of

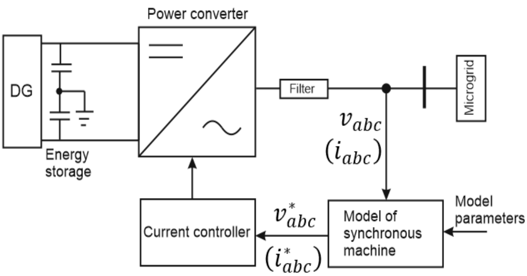

ESM [20]

2.3.1 Voltage-Current VISMA Modelling

Between the two simplified VISMA configurations from IEE TU-Clausthal, the Voltage–Current abc VISMA (SVI-VISMA) model has been considered for stability analysis in this dissertation, this is because of its simplicity in implementation, strong robustness, low parameter dependency, an inherent overcurrent protection, and fast responses that enhance the dynamic performance of the grid converters [44, 45]. The major problem associated with the hysteresis control is the fluctuating nature of frequency with loads which leads to high switching losses, and unwarranted complexities in the design of the output filter. For better utilization of the power converter throughout the entire operating range, the solution is to allow the tolerance band to be variable i.e. tolerance band is adjusted via a control loop so that the average switching frequency remains constant [46]. A three-phase schematic representation of VISMA connected to a point of common coupling (PCC) is depicted in Fig. 2.3. The reference inverter current i^*_{abc} and the actual inverter current i_{abc} are compared and

the switching pulses are produced according to the error. The structure of VISMA machine model in Fig. 2.3 is represented by the control shown in Fig. 4.2. The switching logic is expressed as follows:

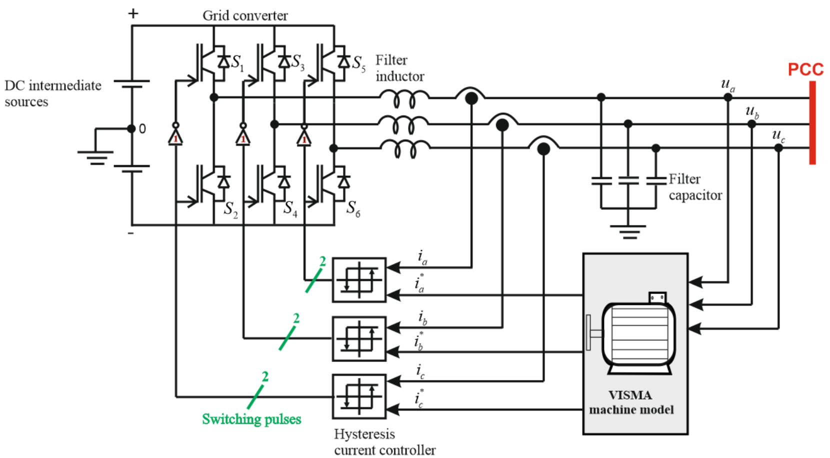

Figure 2.3. *Three phase circuit representation of VISMA controlled inverter*

$$S_{w,abc} = \begin{cases} -1, i_{abc} \geq i^*_{abc} + i_\delta \\ +1, i_{abc} \geq i^*_{abc} - i_\delta \end{cases} \qquad (2.1)$$

Where $S_{w,abc}$ is the switching signal for the six switches, +1 means upper insulated gate bipolar transistor (IGBT) is ON, -1 means lower IGBT is ON, and i_δ is the hysteresis tolerance band. Normally i_{abc} is made to track the i^*_{abc} by forcing the i_{abc} to stay within the hysteresis band.

2.3.1.1 Derivation of the equivalent circuit

If the load star point *N* of a grid connected system is to be connected to the intermediate point 0 between the two DC sources shown in Fig. 2.3, then the three phase controllers would behave like single-phase two-point controllers. But, because of the open star point, they influence each other because each phase voltage depends on all three switch positions and therefore every switching action affects all three bridge branches [46]. To derive the equivalent circuit, only a single two-point controller may be necessary and for simplicity, only phase ‘a’ has been considered for analysis as shown in Fig. 2.4. If the setpoint current

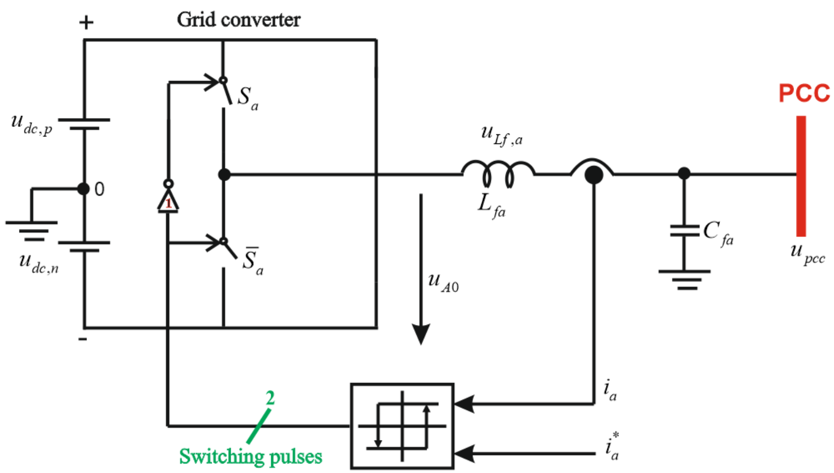

Figure 2.4. *Single-phase phase current control with two-point controller function.*

i_a^* and the instantaneous voltage at the PCC are assumed to be sinusoidal then the following equations are valid:

$$i_a^* = \hat{\imath}_a^*.\sin(w_1 t) \tag{2.2}$$

$$e_{pcc} = \hat{u}_{pcc}.\sin(w_1 t + \varphi_e) \tag{2.3}$$

The instantaneous output phase voltage of the converter on the left side of the filter inductance L_{fa} in terms of modulation function m when S_a is closed with the circuit is given by:

$$u_{A,0} = u_{dc,p} m = u_{Lf,a} + u_{pcc} \tag{2.4}$$

Where $m = M.\sin(w_1 t + \varphi_m)$, and $M,$ is the modulation index, $u_{Lf,a} =$ Voltage drop across the filter inductance and u_{pcc} is the voltage at the PCC.

The results of the SIMULINK simulation of Fig. 2.3 is shown in Fig. 2.5. The idea is to demonstrate the switching process of the phase current control. The 1 & 2 vertical lines in Fig. 2.5 (a) represent the horizontal zoomed points depicted in Fig. 2.5 (b) for only phase 'a' scenario. If the actual current i_a exceeds the upper limit of the tolerance band i_δ the lower switch is closed, while the upper switch is opened. The inductor L_{fa} is then discharged and the current drops accordingly. Only when the lower limit of the tolerance band is reached is the lower switch opened again and the upper switch closed. In this case the choke is charged and the current increases again. The two switches therefore always work in push-pull [41]. With constant inductance, the speed at which the current decreases or increases depends on the current voltage difference between the DC voltages $U_{dc,p}$, $U_{dc,n}$ and the counter voltage, among other things. In the enlarged section (Fig. 2.5 b), the duration of the discharge t_1 is shorter than that of the charge t_2 because the voltage difference Δu is greater when discharging than when charging. The sum of t_1 and t_2 then represents the switching period T_{sw}. Its reciprocal value is referred to as the instantaneous switching frequency f_{sw}. Fig. 2.5 (c) illustrates the switching pulses of the three phase legs of the inverter shown in Fig. 2.3. Each 2-point controller produces a pulse train and each pulse train controls two switches in the same phase. The black, blue and the orange colour pulses of Fig. 2.5 (c) depicts the switching scenario at phase leg 'a' (S_5 & S_6), phase leg 'b' (S_3 & S_4), and phase leg 'c' (S_1

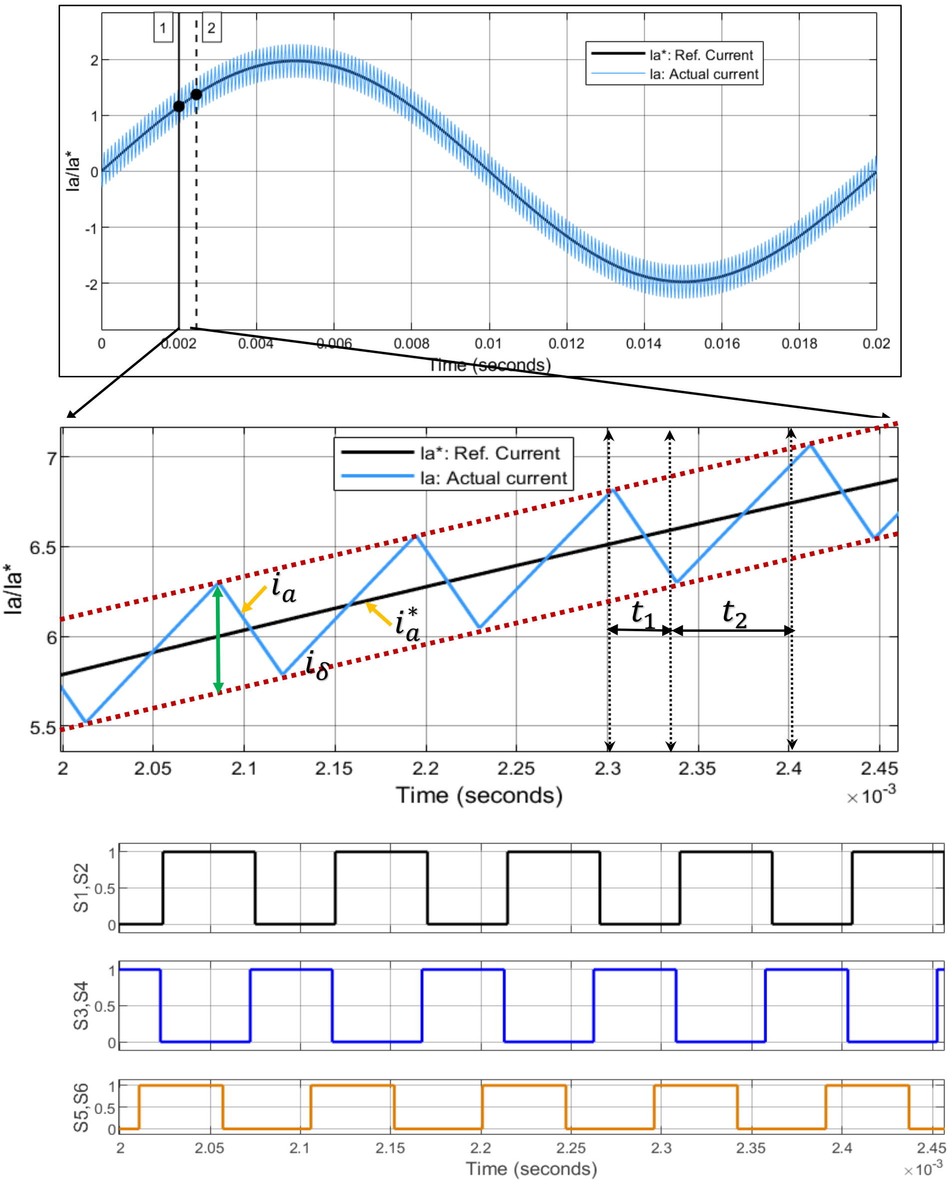

Ia*: Ref. Current
Ia: Actual current
Ia/Ia*
Time (seconds)
1
2
i_a
i_a^*
i_δ
t_1
t_2
$\times 10^{-3}$
S1,S2
S3,S4
S5,S6

(a)

(b)

(c)

Figure 2.5. Simulation of hysteresis current controller (a) Phase current curve, actual and reference (b) Zoomed actual phase current curve (c) Switching pulses for the three phase legs

& S_2). The ON and OFF states of the upper and lower switches of each phase leg are complementary in nature. From the voltage expression in (2.4), the equivalent circuit illustrated in Fig. 2.6 can be drawn when the inverter is in islanded/autonomous mode.

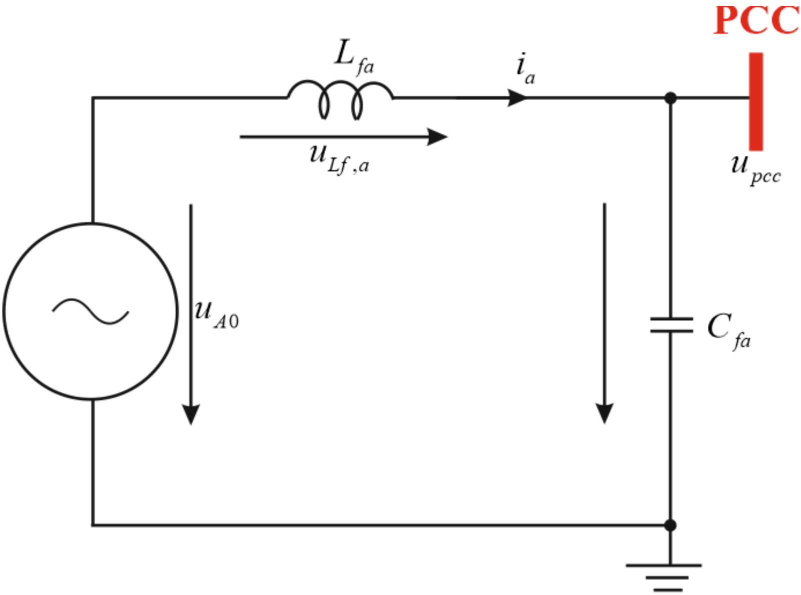

Figure 2.6. Per phase equivalent of VISMA inverter in autonomous mode with half-bridge

2.3.1.2 2-point controller with grid filter

Due to the control method deployed for SVI-VISMA, it is called a current source model. When this VISMA inverter is in the grid connected mode, connection of capacitor at its terminal is not necessary because it is already recognized as a current source model. If the inverter is in autonomous mode, then SVI-VISMA wouldn't have the capability to provide grid forming function (i.e. behaves as a real electromechanical synchronous machine), because zero current flows through the filter inductor and as such proper operation of the phase current controller is not guaranteed. Therefore, sufficiently large capacitors (> 20% of the rated inverter power) must be connected to the output of VISMA inverter as depicted in Fig. 2.3. The current controller can keep the fundamental oscillation (wave) of the output current exactly at the setpoint (Figure 2.5 a) so that $i_a = i_a^*$ [47]. The equivalent circuit diagram in Fig. 2.7 is obtained by replacing the current control loop with a controllable current source [29]. Thus, only filter capacitance remains and of which its dynamic response

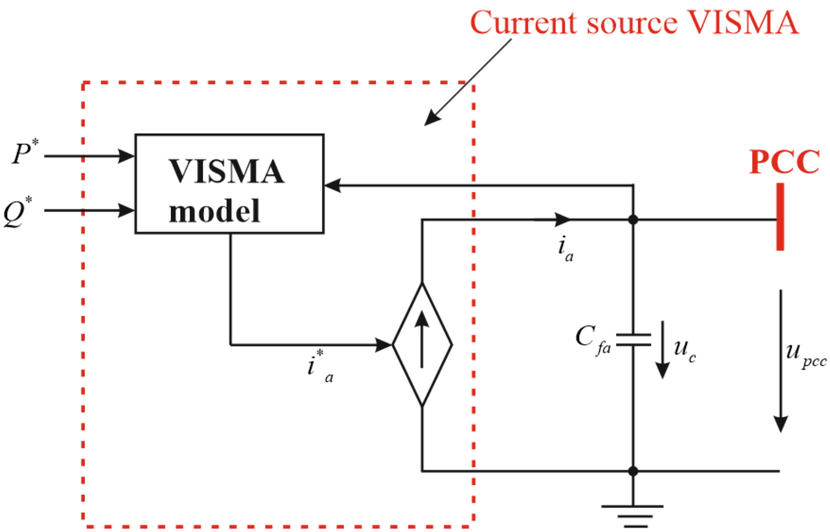

Figure 2.7. Single-phase current control with a two-position controller [29]

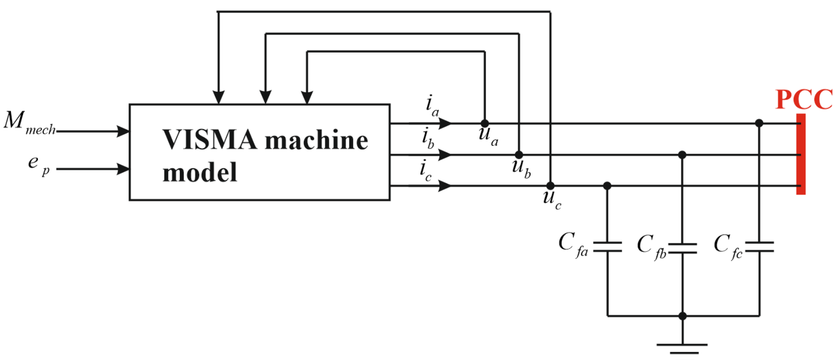

Figure 2.8. Equivalent circuit of the converter with VISMA model, modified based on reference [48]

has negligible effect on the steady state stability. If the fundamental output voltage of the grid inverter is examined more closely, the corresponding circuit of the converter with VISMA model can be drawn as illustrated in Figure 2.8 where filter inductance L_{fa} is eliminated due to the sufficiently fast hysteresis current controller (rise time < 1 ms) [48].

2.3.1.3 abc reference frame model of VISMA

The modelling of VISMA can be sub-divided into the electrical and mechanical part, the former is modelled by the stator voltage of the ESM while the latter is modelled by the rotor dynamic equation. The two sub-models are coupled through a swing equation, which takes mechanical and electrical power into consideration, and eliminates simulating the complete electromagnetic relationship of stator and rotor [4, 49]. In the previous analysis, the converter with two-position controller for phase current control is replaced by an ideal current source. This segment demonstrates modelling of VISMA in abc coordinate system and is schematically represented by

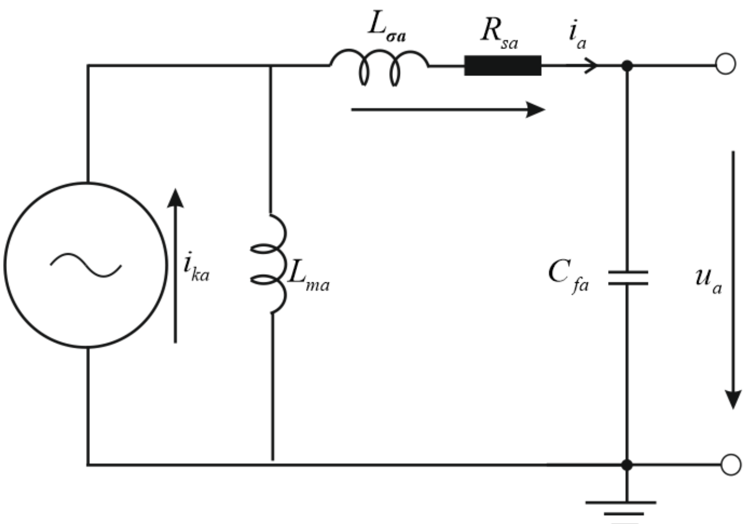

Figure 2.9. Per phase equivalent circuit of the synchronous generator with power source (phase a)

equivalent circuit of ESM in generator mode with an alternating current source $i_{ka} = i_a^*$ as shown in Figure 2.9. From Fig. 2.9, L_{ma} is the main inductance, $L_{\sigma a}$ is leakage inductance and R_{sa} is the winding resistance. With the help of Ohm's law, the equivalent circuit diagram of the synchronous generator with current source can be converted into the equivalent circuit diagram with voltage source (Figure 2.10). In the VISMA system, the equivalent circuit diagram of the synchronous generator is connected to the converter as the virtual part with converter i_a^* into a voltage source e_a with the virtual stator inductance corresponds to the real part of the synchronous machine part according to Fig. 2.8.

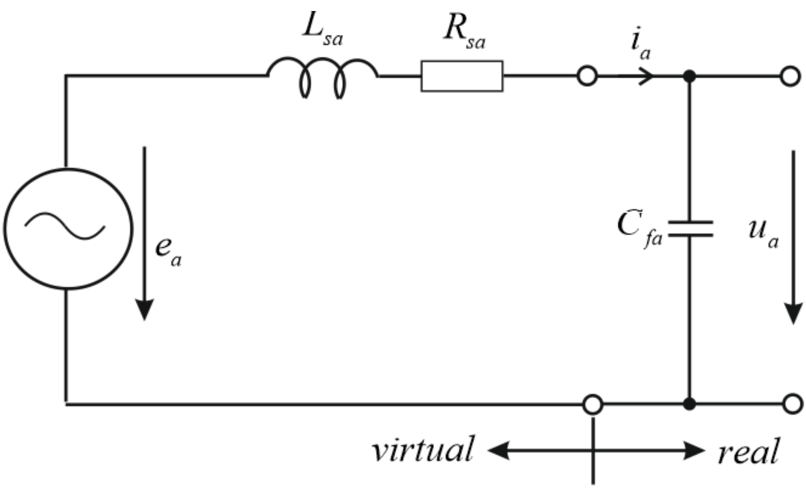

Figure 2.10. Per phase equivalent-circuit of ESM (phase a)

The inductance of the stator winding, L_{sa} and the per phase voltage, e_a is defined in equation (2.5) as follows:

$$\begin{cases} L_{sa} = L_{ma} + L_{\sigma a} \\ e_a = \frac{di_{ka}}{dt} \cdot L_{ma} \end{cases} \tag{2.5}$$

The machine electrical equation is defined as

$$\vec{\boldsymbol{E}}^*{}_{\boldsymbol{i}} = \boldsymbol{R}_{\boldsymbol{si}} \vec{\boldsymbol{I}}^*{}_{\boldsymbol{i}} + \boldsymbol{L}_{\boldsymbol{si}} \frac{d\vec{\boldsymbol{I}}^*{}_{\boldsymbol{i}}}{dt} + \vec{\boldsymbol{U}}^*{}_{\boldsymbol{ti}} \qquad i = 1,2, \dots n\,, \tag{2.6}$$

where$\vec{\boldsymbol{E}}^*{}_{\boldsymbol{i}}, \vec{\boldsymbol{I}}^*{}_{\boldsymbol{i}}, and\ \vec{\boldsymbol{U}}^*{}_{\boldsymbol{ti}}$, n respectively define VISMA virtual internal node voltage vector, virtual stator current space vector, stator terminal voltage space vector and number of VISMAs in the network. The variables in (2.6) are detailed as follows:

$$\vec{\boldsymbol{E}}^*{}_{\boldsymbol{i}} = \begin{bmatrix} \vec{e}_a^* \\ \vec{e}_b^* \\ \vec{e}_c^* \end{bmatrix}; \ \vec{\boldsymbol{I}}^*{}_{\boldsymbol{i}} = \begin{bmatrix} \vec{\imath}_{ai}^* \\ \vec{\imath}_{bi}^* \\ \vec{\imath}_{ci}^* \end{bmatrix} \ and\ \vec{\boldsymbol{U}}^*{}_{\boldsymbol{ti}} = \begin{bmatrix} \vec{u}_{ai}^* \\ \vec{u}_{bi}^* \\ \vec{u}_{ci}^* \end{bmatrix}. \tag{2.7}$$

Here, $\vec{e}_{ai}^*, \vec{e}_{bi}^*\ and\ \vec{e}_{ci}^*$ are per-phase pole wheel voltages

$\vec{\imath}_{ai}^*, \vec{\imath}_{bi}^*\ and\ \vec{\imath}_{ci}^*$ are per-phase stator reference currents, and

$u_{ai}, u_{bi}\ and\ u_{ci}$ are per-phase grid voltage or VISMA terminal voltages. The per-phase internal bus reference voltage is determined based on (2.8) as follows:

$$\vec{E}^*{}_i = \begin{cases} \vec{e}_{a\,i}^* = E_{p0,i}^* . \sin\theta_i \\ \vec{e}_{b\,i}^* = E_{p0,i}^* . \sin\left(\theta_i - \frac{2\pi}{3}\right) \\ \vec{e}_{c\,i}^* = E_{p0,i}^* . \sin\left(\theta_i + \frac{2\pi}{3}\right) \end{cases} \tag{2.8}$$

$E_{p0,i}^*$, is the amplitude of the pole wheel voltage and θ_i, is the virtual rotational angle of the rotor. The resistance $\boldsymbol{R}_{\boldsymbol{si}}$ and inductance $\boldsymbol{L}_{\boldsymbol{si}}$ matrices for the virtual stator are given by (2.9):

$$\boldsymbol{L}_{\boldsymbol{si}} = \begin{bmatrix} L_{si} & 0 & 0 \\ 0 & L_{si} & 0 \\ 0 & 0 & L_{si} \end{bmatrix}, \ and\ \boldsymbol{R}_{\boldsymbol{si}} = \begin{bmatrix} r_{si} & 0 & 0 \\ 0 & r_{si} & 0 \\ 0 & 0 & r_{si} \end{bmatrix} \tag{2.9}$$

Where r_{si} and L_{si} are the per-phase resistance and per phase inductance respectively. Voltage controller of the VISMA is represented using stator voltage equation and is expressed in Laplace domain form from (2.6) as follows:

$$\left[\vec{\boldsymbol{E}}^{*}{}_{i}(\boldsymbol{s}) - \vec{\boldsymbol{U}}_{ti}(\boldsymbol{s})\right]\vec{\boldsymbol{Y}}_{vi}(\boldsymbol{s}) = \vec{\boldsymbol{I}}^{*}{}_{i} \tag{2.10}$$

Where $\vec{\boldsymbol{Y}}_{vi}(\boldsymbol{s})$ and $\vec{\boldsymbol{I}}^{*}{}_{i}$ respectively defines the virtual admittance matrix and reference current of i^{th} VISMA. $\vec{\boldsymbol{Y}}_{vi}(\boldsymbol{s})$ is further defined as follows:

$$\vec{\boldsymbol{Y}}_{vi}(\boldsymbol{s}) = \begin{bmatrix} \frac{1}{r_{si}+sL_{si}} & 0 & 0 \\ 0 & \frac{1}{r_{si}+sL_{si}} & 0 \\ 0 & 0 & \frac{1}{r_{si}+sL_{si}} \end{bmatrix} \tag{2.11}$$

The output active power P_{out}, and output reactive power Q_{out}, of the VISMA-converters are calculated using (2.12) - (2.13) which yields

$$P_{out} = u_a i_a + u_b i_b + u_c i_c \quad \text{and} \tag{2.12}$$

$$Q_{out} = \frac{1}{\sqrt{3}}\left[i_a(u_b - u_c) + i_b(u_c - u_a) + i_c(u_a - u_b)\right] \tag{2.13}$$

where

u_a, u_b, u_c are per-phase output voltage of the inverter, and

i_a, i_b, i_c are per-phase output current of the inverter.

2.3.1.4 Two axis model of VISMA

In late 1920's R. H. Park formulated a coordinate transformation which in effect replaces time dependent variables of the stator circuit of ESM with fictitious variables of the rotor windings. Park revolutionizes machine theory by creating a transformation matrix that removes all time-varying inductances from the voltage equations of ESM which arises as a result of relative motion between rotor winding and stator winding [50]. Stator windings in abc frame (i.e., currents or voltages) can be equivalently expressed in d-q frame, such that the situation similar to the primitive machine is obtained, a representation of this is depicted in Figure 2.11 below. The d-q axis model offers a better and less complicated analytical approach to modeling machines in comparison to space vector format that designates machines in terms of complex variables. Phases a, b and c are respectively displaced by 120^{o} from one another while q-axis and d-axis are at quadrature to each other. Thus, resolving the phase variables ρ_a, ρ_b, ρ_c into the d and q axes gives the following two degrees of freedom matrix

$$\begin{bmatrix} \rho_d \\ \rho_q \end{bmatrix} = \begin{bmatrix} \cos\theta & \cos\left(\theta - \frac{2\pi}{3}\right) & \cos\left(\theta - \frac{4\pi}{3}\right) \\ \sin\theta & \sin\left(\theta - \frac{2\pi}{3}\right) & \sin\left(\theta - \frac{4\pi}{3}\right) \end{bmatrix} \begin{bmatrix} \rho_a \\ \rho_b \\ \rho_c \end{bmatrix}. \quad (2.14)$$

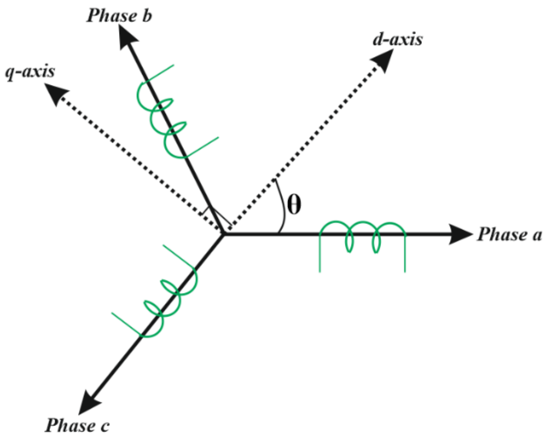

Figure 2.11. $3 - \phi$ machine and d-q equivalent

But this transformation yields two degrees of freedom. Therefore, to make it a square matrix (three degrees of freedom), we can use the concept of symmetrical component analysis such that

$$\rho_o = \rho_a + \rho_b + \rho_c \quad (2.15)$$

ρ_o is called zero component. Therefore, we can write (2.14) as

$$\begin{bmatrix}\rho_d\\ \rho_q\\ \rho_o\end{bmatrix} = \begin{bmatrix}\cos\theta & \cos\left(\theta-\frac{2\pi}{3}\right) & \cos\left(\theta-\frac{4\pi}{3}\right)\\ \sin\theta & \sin\left(\theta-\frac{2\pi}{3}\right) & \sin\left(\theta-\frac{4\pi}{3}\right)\\ 1 & 1 & 1\end{bmatrix}\begin{bmatrix}\rho_a\\ \rho_b\\ \rho_c\end{bmatrix}. \quad (2.16)$$

A constant $2/3$ is usually multiplied to account for the peak mmf of a rotating magnetic field $\Im_R = \frac{3}{2}\Im_m\cos(wt-\phi)$. So that in general we have:

$$\begin{bmatrix}\rho_d\\ \rho_q\\ \rho_o\end{bmatrix} = \frac{2}{3}\begin{bmatrix}\cos\theta & \cos\left(\theta-\frac{2\pi}{3}\right) & \cos\left(\theta-\frac{4\pi}{3}\right)\\ \sin\theta & \sin\left(\theta-\frac{2\pi}{3}\right) & \sin\left(\theta-\frac{4\pi}{3}\right)\\ \frac{1}{2} & \frac{1}{2} & \frac{1}{2}\end{bmatrix}\begin{bmatrix}\rho_a\\ \rho_b\\ \rho_c\end{bmatrix} \quad (2.17)$$

From equation (2.17), let transformation matrix, k be defined as

$$k = \frac{2}{3}\begin{bmatrix}\cos\theta & \cos\left(\theta-\frac{2\pi}{3}\right) & \cos\left(\theta-\frac{4\pi}{3}\right)\\ \sin\theta & \sin\left(\theta-\frac{2\pi}{3}\right) & \sin\left(\theta-\frac{4\pi}{3}\right)\\ \frac{1}{2} & \frac{1}{2} & \frac{1}{2}\end{bmatrix} \quad (2.18)$$

The inverse of (2.18) is given by

$$k^{-1} = \begin{bmatrix}\cos\theta & \sin\theta & 1\\ \cos\left(\theta-\frac{2\pi}{3}\right) & \sin\left(\theta-\frac{2\pi}{3}\right) & 1\\ \cos\left(\theta-\frac{4\pi}{3}\right) & \sin\left(\theta-\frac{4\pi}{3}\right) & 1\end{bmatrix}. \quad (2.19)$$

The pu virtual rotor speed $w_r(t)$ is given as

$$\theta = \int_0^t w_r(dt) + \theta_o(0) \quad (2.20)$$

where θ, defines the angular displacement measured with respect to the d-axis in the rotor reference frame. θ_0 represents the initial value of the angle of rotation at time $t = 0$. Now, applying Kirchhoff's voltage law (KVL) to the per-phase stator equivalent circuit of Fig. 2.10 in the natural variables yields the following

$$e_s = i_s r_s + p\lambda_s + u_s \tag{2.21}$$

where

$\lambda_s = L_s i_s$ and $p\lambda_s$ is the rate of change of flux linkages. (2.21) is written in three phase form as given as

$$e_{abcs} = i_{abcs} r_s + p\lambda_{abcs} + u_{abcs} \text{ and} \tag{2.22}$$

$$e_{dqos} = k e_{abcs} \, . \tag{2.23}$$

Multiplying (2.22) through by k yields

$$k e_{abcs} = k i_{abcs} r_s + k p\lambda_{abcs} + k u_{abcs} \tag{2.24}$$

$$e_{dqos} = k e_{abcs} = k r_s i_{abcs} + k p\lambda_{abcs} + u_{qdos} \, . \tag{2.25}$$

However,

$$i_{abcs} = k^{-1} i_{qdos} \qquad \text{and} \tag{2.26}$$

$$e_{abcs} = k^{-1} e_{qdos} \tag{2.27}$$

$$\therefore \; e_{dqos} = k e_{abcs} = k r_s k^{-1} i_{qdos} + kp\left[k^{-1}\lambda_{qdos}\right] + u_{qdos} \tag{2.28}$$

but also,

$$k k^{-1} = 1$$

such that (2.29)

$$e_{dqos} = k e_{abcs} = r_s i_{qdos} + kp\left[k^{-1}\lambda_{qdos}\right] + u_{qdos} \, . \tag{2.30}$$

Expanding (2.28) using product rule yields

$$e_{dqos} = k e_{abcs} = r_s i_{qdos} + kp[k^{-1}]\lambda_{qdos} + p\left[\lambda_{qdos}\right] + u_{qdos} \tag{2.31}$$

and thus

$$pk^{-1} = \frac{dk^{-1}}{dt} = \frac{dk^{-1}}{dt} x \frac{d\theta}{d\theta} = \frac{d\theta}{dt} x \frac{dk^{-1}}{d\theta} = \begin{bmatrix} -\sin\theta & \cos\theta & 0 \\ -\sin\left(\theta - \frac{2\pi}{3}\right) & \cos\left(\theta - \frac{2\pi}{3}\right) & 0 \\ -\sin\left(\theta - \frac{4\pi}{3}\right) & \cos\left(\theta - \frac{4\pi}{3}\right) & 0 \end{bmatrix} w_r . \tag{2.32}$$

For $\theta = 0$, we obtain after simplifying

$$kp[k^{-1}] = w_r \begin{bmatrix} 0 & 1 & 0 \\ -1 & 0 & 0 \\ 0 & 0 & 0 \end{bmatrix} \tag{2.33}$$

and therefore

$$kp[k^{-1}]\lambda_{qdos} = w_r \begin{bmatrix} 0 & 1 & 0 \\ -1 & 0 & 0 \\ 0 & 0 & 0 \end{bmatrix} \begin{bmatrix} \lambda_{qs} \\ \lambda_{ds} \\ \lambda_{os} \end{bmatrix} = w_r\lambda_{ds} - w_r\lambda_{qs} + 0\lambda_{os} \tag{2.34}$$

Equation (2.31) can now be re-written as follows:

$$e_{dqos} = ke_{abcs} = ki_{qdos} \pm w_r\lambda_{dqos} + p\lambda_{qdos} + u_{qdos} \tag{2.35}$$

Equation (2.34) shows that w can assume $\pm$ and in expanded form we have:

$$e_{ds} = i_{ds}r_s + p\lambda_{ds} - w_r\lambda_{qs} + u_{ds} \tag{2.36}$$

$$e_{qs} = i_{qs}r_s + p\lambda_{qs} + w_r\lambda_{ds} + u_{qs} \tag{2.37}$$

$$e_{os} = i_{os}r_s + p\lambda_{os} \tag{2.38}$$

Under balanced conditions, $i_{os} = 0$ as it produces no resultant flux linkage. All other zero sequence components are also zero, so that (2.38) becomes insignificant in the further analysis [51]. One important fact about equations (2.36) and (2.37) is that the voltage and current variables are no longer sinusoidal signals but rather direct current signals. They could serve as the reference signal to a system, this explains why they are often used in the design of control systems with most applications involving PI controllers [52]. The d-q coordinate voltage expressions in (2.36) and (2.37) for i^{th} VISMA are written in terms of virtual stator inductances as follows:

$$e_{di} - u_{di} = r_{si}i_{di} + L_{si}\frac{di_{di}}{dt} - \omega_r L_{si} \cdot i_{qi} \tag{2.39}$$

$$e_{qi} - u_{qi} = r_{si} \cdot i_{qi} + L_{si}\frac{di_{qi}}{dt} + \omega_r L_{si} \cdot i_{di} \tag{2.40}$$

Where, e_{dqi}, u_{dqi}, i_{dqi} are the pole wheel voltages, VISMA terminal voltages, and VISMA output current in d-q coordinate for i^{th} VISMA. r_{si}, L_{si}, are phase resistance, phase inductance and the ω_{ri} is the pu rotor speed respectively for i^{th} VISMA. Under balanced conditions, the nonlinear per-unit equation of the electromagnetic power P_{ei} developed in the virtual airgap of VISMA should be the same as the instantaneous active power output of the converter initially defined in (2.12). Transforming from machine variables to d-q coordinate system yields the following expression [53]:

$$P_{ei} = e_{di}i_{di} + e_{qi}i_{qi} \tag{2.41}$$

Due to the multidimensionality and complexities of the stability issues, it is of interest to make simplifying assumptions by adopting a suitable system representation and a detailed analytical methods [19]. In the ESM, the fundamental flux in the field-winding is in the path of the direct axis of the rotor and it developed an electromotive force (EMF) that lags this main-flux by 90^0. Thus, the generated virtual voltage *E* is principally on the path of rotor quadrature-axis, this however means that $e_d = 0$ [42, 54, 55]. In order to simplify the model of the VISMA further, the following assumptions are made (i) neglecting stator transients [56], (ii) neglecting transient saliency i.e. $x_{di} = x_{qi} = x_i$ [39] (iii) virtual stator is assumed purely inductive so that $r_{si} = 0$. (2.37) - (2.39) therefore reduces to:

$$u_{di} = x_i \cdot i_{qi} \tag{2.42}$$

$$e_{qi} - u_{qi} = x_i \cdot i_{di} \tag{2.43}$$

$$P_{ei} = e_{qi} i_{qi} \tag{2.44}$$

According to [56, 57], stator and network transients, governor model can be neglected without loss of generality when dealing with small-signal stability analysis of multiconverter based power systems. This research focuses on the steady state stability (SSS) after small disturbances rather than the transient analysis. Due to the high complexity and dimensionality of the foreseeable multi-VISMA system towards achieving 100% renewable power systems and because of the research motive of reducing the entire power system to direct interactions between virtual nodes of the VISMA, it is thus assumed the transients associated with the transmission line and virtual stator decay very fast so that VISMA microgrid is represented as positive sequence network. Since the rotor-angle is directly related to the active power control, the effect of voltage control in the rotor angle stability analysis will be ignored. To consolidate more on simplicity of (2.42) - (2.44) to neglecting the transients in the dynamics, it was reported in [58] that the steady state stability behaviour of any dynamical system is solely influenced by its stationary characteristics and not in any way affected by dynamic-parameters like passive damping, system-inertia, time-constant etc.

The simplified voltage equation of VISMA given in (2.42) - (2.43) is arranged in matrix form as follows:

$$\begin{bmatrix} u_{di} \\ u_{qi} \end{bmatrix} = \begin{bmatrix} 0 & x_i \\ -x_i & 0 \end{bmatrix} \begin{bmatrix} i_{di} \\ i_{qi} \end{bmatrix} + [0 \quad 1] \begin{bmatrix} 0 \\ e_{qi} \end{bmatrix} \tag{2.45}$$

Mechanical characteristics

Swing equation describes the rotor dynamics of VISMA and it is central to obtaining the stationary operating points of all the dynamic nodes in the microgrid. Any imbalances on the opposing torque acting on the virtual-rotor will lead to the acceleration or deceleration of the rotor depending on whether load is reduced or added to the network. Aside from using swing equation for power balancing in the network, VISMA also uses it to mimic inertia response of ESM. The complete equation of motion for the virtual mechanical part of the VISMA in per unit [39, 53, 59] is described by the following equations:

$$2H_i \frac{dw_{ri}}{dt} = M_{mech,i} - \frac{P_{ei}}{w_{ri}} - D_i(w_{ri} - w_s) \tag{2.46}$$

$$\begin{cases} \frac{d\delta_i}{dt} = w_b(w_{ri} - w_s) \\ \theta_i = w_s t + \delta_i \end{cases} \tag{2.47}$$

Where:

H = Equivalent moment of inertia of rotating mass in sec.

M_{mech} = Virtual shaft torque input to VISMA in pu

P_e = Virtual electrical power output

D = Virtual damping torque constant in pu

w_r = Angular frequency in mechanical rad/sec.

θ = Rotor mechanical angular position in rad

w_s = Angular synchronous speed in pu

w_b = base rotor electrical speed in electrical radians per seconds rad/sec.

δ = Rotor angular position measured with respect to synchronous axis in rad

2.4 Prominent VSG control topologies

2.4.1 OSAKA model

This model was invented by the research group of Ise laboratory in OSAKA University, Japan in 2011 [24, 30, 60]. The control scheme of this topology significantly depends on the swing equation of conventional ESM and utilizes a voltage-mode control, where both the real and reactive power at the grid are respectively regulated by modulating the phase-angle θ and amplitude of the voltage source converter E_p [61]. The dynamic equations of the topology in Fig. 2.12 are described by (2.48) - (2.50) [62].

$$P_{in} - P_{out} = Jw_r \frac{dw_r}{dt} + D(w_r - w_g) \tag{2.48}$$

$$P_{in} - P_0 = -\frac{m_p}{1+T_d s}(w_r - w_0) \tag{2.49}$$

$$Q_{ref} - Q_0 = -m_q(V_{out} - E_0) \tag{2.50}$$

P_0, P_{in}, P_{out} are set values of active power, Virtual shaft-power, output active-power respectively

Q_0, Q_{ref}, Q_{out} are set values of reactive-power, reference value for reactive power control and output reactive-power respectively

w_g, w_0, Output voltage angular-frequency, set value of angular-frequency

V_{out}, E_0 converter output voltage, nominal voltage

T_d, J, D Time constant of governor delay, virtual inertia, virtual damping factor

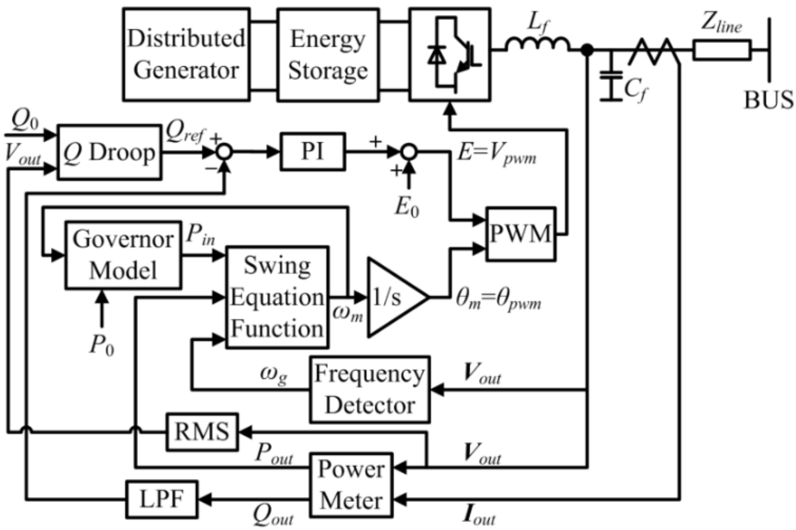

Figure 2.12. OSAKA control topology [31, 63]

The Governor Model block described by equation (2.49) is required to maintain a frequency stability, which is achieved by establishing a linear relationship between the grid frequency and the active power output from the converter. On the other hand, Q-Droop block is primarily required to provide voltage stability by creating a linear relationship between reactive power and the voltage described by (2.50). T_d, is included to help mimic the delayed characteristics of a real governor of ESM. The predefined powers P_0 and Q_0 are decided by the VSG rating and the power system operators (PSO) requirements [64].

2.4.2 Synchronverter

This VSG control scheme was proposed in 2009. It is an inverter that is designed for three phase grid connected system to mimic the behavior of conventional synchronous machines. The initial model name was static synchronous generator (SSG) [65] before being later changed to synchronverter [22]. The complex nonlinear dynamic equation of synchronverter is similar to that of ESM only that the power exchanged with the prime mover is replaced with power exchange with the dc bus. Also, it is modelled with the characteristic of cylindrical rotor type of having transient saliency (i.e. $x_{di} = x_{qi} = x_i$) neglected. The saturation effect in the iron core, eddy current losses and damper winding effects are also ignored in the model. The unpleasant hazards associated with ESM such as hunting (oscillations around the synchronous frequency) and instability issue as a result of loss of excitation are also possible during synchronverter operation. The basic block diagram representation of (synchronverter power unit) is depicted in Fig. 2.13 while the control structure is illustrated in Fig. 2.14. The basic equations used in Synchronverter scheme are given as follows:

$$J\frac{dw_r}{dt} = \left[T_m - T_e - D_p\left(w_{ref} - w_r\right)\right] \tag{2.51}$$

$$T_e = M_f i_f \langle i, \widetilde{\sin}\theta \rangle \tag{2.52}$$

$$E = w_r M_f i_f \langle i, \widetilde{\sin}\theta \rangle \tag{2.53}$$

$$e = E\widetilde{\sin}\theta \tag{2.54}$$

$$P = w_r T_e \tag{2.55}$$

$$Q = -E.\langle i, \widetilde{\cos}\theta \rangle \tag{2.56}$$

Where $J,\ T_m,\ T_e\ and\ D_p$ defines the virtual inertia, virtual-shaft torque, virtual electromagnetic torque, and virtual damping torque constant respectively. i_f, is the excitation current and M_f, is the optimum value of mutual inductance. Other variables $E, P_{set}, Q_{set}, P, Q$ are respectively defined as amplitude of the excitation voltage, active reference power, reactive reference power, the instantaneous active power, the instantaneous reactive power. $\dot{\theta}$, is the virtual rotor mechanical angular speed.

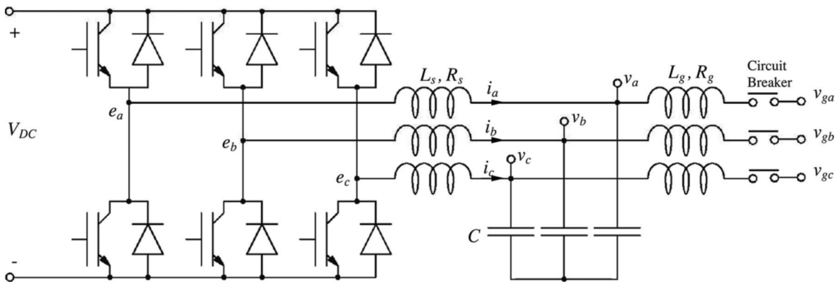

Figure 2.13. Power part of synchronverter [65]

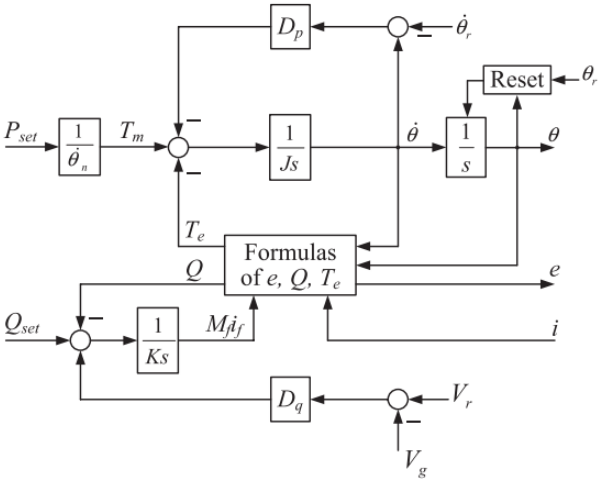

Figure 2.14. Synchronverter control scheme [65]

Expression for $\widetilde{\sin}\theta$ and $\widetilde{\cos}\theta$ are given in (2.57) – (2.58):

$$\widetilde{\sin}\theta = \begin{bmatrix} \sin\theta \\ \sin\left(\theta - \frac{2\pi}{3}\right) \\ \sin\left(\theta + \frac{2\pi}{3}\right) \end{bmatrix} \tag{2.57}$$

$$\widetilde{\cos}\theta = \begin{bmatrix} \cos\theta \\ \cos\left(\theta - \frac{2\pi}{3}\right) \\ \cos\left(\theta + \frac{2\pi}{3}\right) \end{bmatrix} \tag{2.58}$$

2.4.3 Cascaded Virtual Synchronous Machine (CVSM)

CVSM is a voltage controlled model which was proposed in 2013 [21]. This control scheme is based on power-frequency characteristics. It is made up of inertia mimicking unit, reactive droop unit, cascaded current and voltage controller units, and modulation unit. The inertia emulation and system damping are achieved with the help of swing equation. This control scheme doesn't require phase locked loop for grid synchronisation, though it does need it for oscillation damping. It is made up of two cascaded voltage and current controllers as illustrated in Fig. 2.15.

Figure 2.15. CVSM control scheme [21]

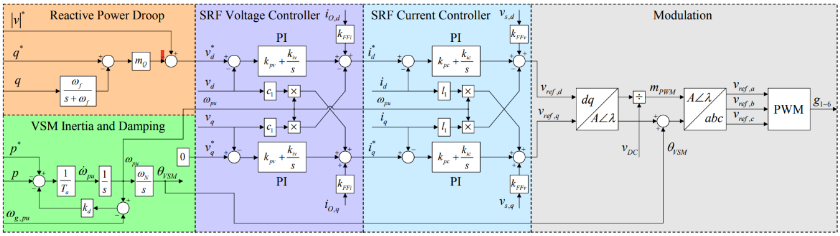

The voltage controllers use the voltage difference between reference voltage from the reactive droop controller $v_{o,dq}^{*}$ and the measured grid voltage $v_{o,dq}$ to output a reference current $i_{c,dq}^{*}$ which is also similarly compared with the measured grid current $i_{o,dq}$ by the current controller to output a converter reference voltage $v_{c,dq}^{*}$ which yield m_{dq} after modulation. The vital dynamics equations are given in (2.59) – (2.62). Parameter definitions not given above are obtainable in Ref. [21].

$$T_a \frac{dw_r}{dt} = P_{ref} - K_d(w_r - w_g) - P_e \tag{2.59}$$

$$\left(v_{o,dq}^{*} - v_{o,dq}\right)\left(k_{pv} + \frac{k_{iv}}{s}\right) \mp v_{o,qd} c_f w_r + k_{FFi} i_{o,dq} = i_{c,dq}^{*} \tag{2.60}$$

$$\left(i_{c,dq}^{*} - i_{c,dq}\right)\left(k_{pc} + \frac{k_{ic}}{s}\right) \mp i_{o,qd} l w_r + k_{FFi} v_{o,dq} = v_{ref,dq}^{*} \tag{2.61}$$

$$\frac{v_{ref,dq}^{*}}{v_{DC}} = m_{dq} \tag{2.62}$$

2.4.4 VSYNC

VSYNC control scheme developed as a current source model was proposed in 2009 [66]. VSYNC idea is to control the grid frequency through distributed energy storage systems rather than the DGs, as illustrated in Fig. 2.16 a. The major components of VSYNC are the power processor, the energy storage unit (e.g. supercapacitor, battery, flywheel) and the control unit. Power between the grid and the energy storage device is controlled to mimic both the rotational inertia response and the power-frequency droop response of ESM so as to counteract any frequency deviations in the grid. The structure of PLL adopted by VSYNC is obtainable in [29]. The inertia emulation is achieved through PLL having a characteristic identical to that of ESM. The dynamics describing this VSG control scheme is given by (2.63) – (2.65) [66, 67].

$$P_{VSG} = k_{SOC}(\mathrm{SOC} - \mathrm{SOC}_{ref}) - k_{inertia}\frac{dw}{dt} - k_{damp}(w - w_{ref}) \quad (2.63)$$

$$i_d^* = \left[\frac{2u_d}{3(u_d^2+u_q^2)}\right] P_{VSG} \quad (2.64)$$

$$i_q^* = \left[\frac{2u_q}{3(u_d^2+u_q^2)}\right] P_{VSG} \quad (2.65)$$

Equation (2.65) defines the real power generated to or by the VSYNC, and is schematically represented by Fig. 2.16 b. The $1^{st}, 2^{nd}, and\ 3^{rd}$ terms of (2.65) respectively indicate the

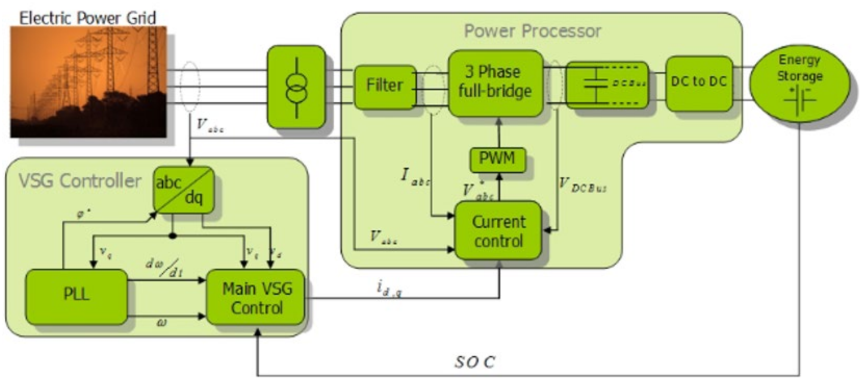

(a)

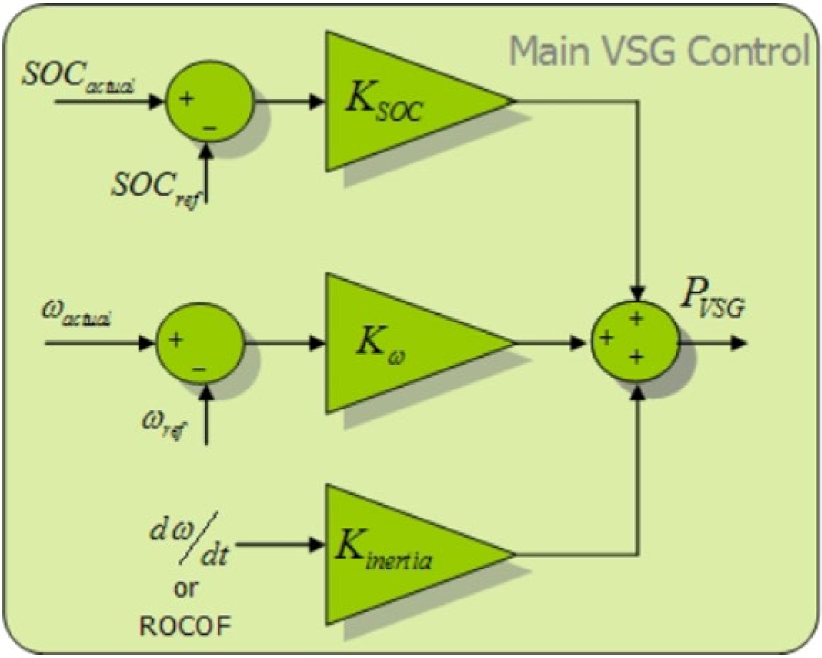

(b)

Figure 2.16. VSYNC (a) complete configuration model (b) Main VSG control block [67]

frequency droop characteristic, linearized inertia emulation and the energy storage (SOC) maintenance. i_d^* and i_q^* are reference currents.

2.4.5 Kawasaki Heavy Industry (KHI) Control Model

KHI is a current controlled scheme proposed in 2012 with the grid converter designed to operate as a voltage outputting model [68, 69] . The control of the grid converter is based on a VSG model of algebraic type. In this control scheme, a delightful operation under all kinds of load (in particular, unbalanced and nonlinear loads) is achieved by employing a current feedback loop that generates a current reference through a phasor diagram of ESM. The KHI scheme uses the conventional model of a governor and AVR to correct the deviations in grid frequency and grid voltage respectively [70-72]. The control structure of KHI model in Laplace domain is depicted in Fig. 2.17.

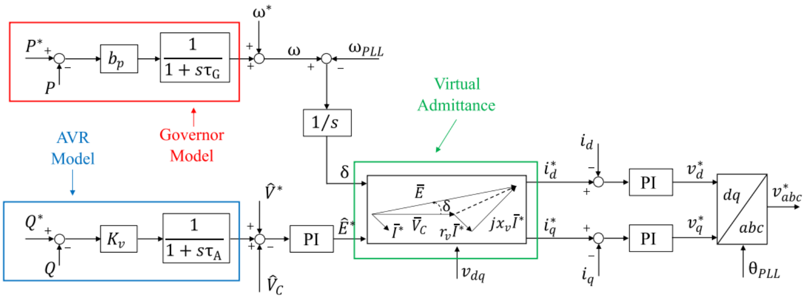

Figure 2.17. KHI control scheme [29]

The output current expression of the virtual machine represented by the phasor is given by

$$\begin{bmatrix} i_d^* \\ i_q^* \end{bmatrix} = Y_v \begin{bmatrix} E_d - v_d \\ E_q - v_q \end{bmatrix}, \tag{2.66}$$

where:

$$Y_v = \frac{1}{r_v^2 + x_v^2} \begin{bmatrix} r_v & x_v \\ -x_v & r_v \end{bmatrix}; \quad \begin{bmatrix} E_d \\ E_q \end{bmatrix} = E \begin{bmatrix} \cos\delta \\ \sin\delta \end{bmatrix} \text{ and } E = |\hat{E}^*| .$$

From the phasor diagram in Fig. 2.17, the reference generated currents (i_d^* and i_q^*) are compared with inverter output current (i_d and i_q) which is also equivalent to the virtual armature current of the VSG control scheme. An appropriate current controller is then necessary to generate the right control commands, though in this control scheme PI controllers are used to generate reference voltages for the PWM controls. The virtual reactance x_v is a fixed value independent of system frequency, i.e. $x_v \neq wL_v$. The phase angle between the virtual generated EMF $\hat{E}^*$and the grid line voltage, $\hat{V}_c$ is defined by δ and valuated through the governor and the PLL frequency w_{PLL}. The other model parameters $w, w^*, Y_v, \hat{V}^*$ are respectively defined as virtual angular rotor speed, reference angular speed, virtual admittance, voltage reference.

2.4.6 Synchronous Power Controller (SPC)

SPC was proposed in 2013 as a current source model with a voltage-control characteristic of the grid connected inverter [43]. It permits the operation of a grid inverter in a similar way as the ESM but with an improvement on the weak behaviour of ESM. The general structure of the control algorithm shown in Fig. 2.18 is similar to that of voltage-current simplified VISMA model invented by IEE, TU-Clausthal, the major differences in their features are the manner in which internal virtual voltage is generated and as well as their electromechanical principle. SPC uses a second order optimized model with an over-damped response that helps to reduce the oscillations in the system [41, 73], whereas VISMA model relies on the traditional swing equation. In SPC control scheme, the inertia, damping and droop characteristics can be independently configured without interfering with each other. The swing equation in SPC is modified and appropriately designed without subverting the damping characteristics of the converter [74]. Also, both control models generate current reference i_{ref} by utilizing the electrical behaviour of ESM. This is an emulation of the output impedance of the ESM and thus plays an important role during load sharing [75]. Both control schemes avoid the need for extra filtering which plays a vital role in improving the dynamic performance of the controller by enhancing its bandwidth. The involving equation dynamics are given in (2.67) – (2.69) [76]:

$$i_{ref}(s) = \frac{e(s) - V_g(s)}{R + sL} \tag{2.67}$$

$$E = (Q_{set} - Q)\left(k_{pq} + \frac{k_{iq}}{s}\right) + V_g(s) \tag{2.68}$$

$$VCO = \begin{bmatrix} \cos\theta \\ \cos\left(\theta - \frac{2\pi}{3}\right) \\ \cos\left(\theta + \frac{2\pi}{3}\right) \end{bmatrix} \tag{2.69}$$

Where E, i_{ref}, V_g, Q_{set}, Q, θ, k_{pq}, k_{iq}, R, L, are respectively defined as internal voltage amplitude, reference current, grid voltage, set reactive power, measured reactive power, rotor angle, proportional gain, integral gain, virtual resistance, virtual inductance. Three topologies of SPC emulating controller that have been investigated are; SPC-synchronous generator (SPC-SG), SPC-proportional controller (SPC–PI) and SPC- Configurable Natural Droop Controller (SPC–CND). They are majorly differentiated by the form of PLC transfer functions and are defined as follows [77]:

$$\begin{cases} G_{PLC,SG}(s) = \frac{1}{w_s(Js+D)} \\ G_{PLC,PI}(s) = K_X + \frac{K_H}{s} \\ G_{PLC,CND}(s) = \frac{K_P s + K_I}{s+K_G} \end{cases} \tag{2.70}$$

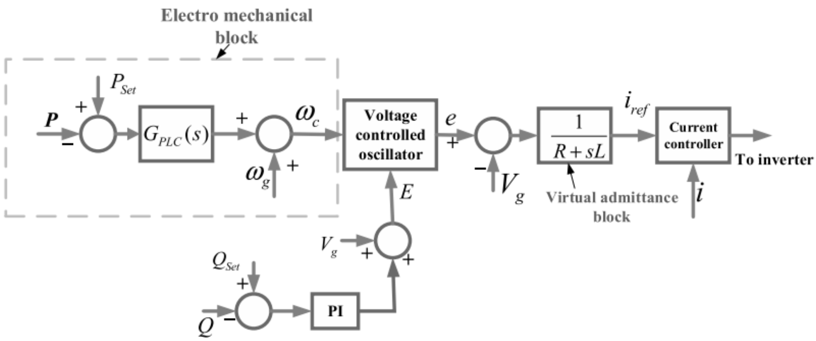

Figure 2.18. Synchronous power controller [75]

2.4.7 Inducverters

The idea of controlling VSC using the dynamics of induction machines was proposed in [78], inverters using this control technique are thus called Inducverters. According to the author, *Inducverters* introduces an easier and a more dependable control technique that is operable under unsymmetrical load and distorted grid circumstances. This control scheme is thus employable for multimachine operations in modern grids with an enhanced dynamic performance. The two major components of this scheme are the current synchronizing and the main controller units. Current synchronizing block is responsible for generating the reference frequency w_{ref} and phase angle θ using the local information (as shown in Fig. 2.19). The core controller unit generates the reference currents $i_{d,ref}$ and $i_{q,ref}$ which are processed through PI controller. The combination of the resulting current i^*_{abc} and the adaptive virtual impedance is thus used to realize the voltage reference e^*_{abc} which is lastly used to generate PWM control signal [75]. In addition to improving the inertia response, Inducverters also have the capability to closely track grid frequency w_g and also supply a constant amount of power to the grid which is one of the major issues of an inverter dominated power grid. The equation dynamics of Inducverters is given in (2.71) – (2.74) [78].

$$i_{d,ref} = (P_{set} - P_{ins})\left(k_p + \frac{k_i}{s}\right) \tag{2.71}$$

$$i_{q,ref} = (Q_{set} - Q_{ins})\left(k_p + \frac{k_i}{s}\right) \tag{2.72}$$

$$J\frac{dw_r}{dt} = T_e - T_L - Dw_r \tag{2.73}$$

$$w_s = \frac{d\theta}{dt} = w_r + w_{slip} + w_0 \tag{2.74}$$

Where $w_{slip}, T_L, w_s, J, k_p, k_i$ respectively define virtual slip speed, load torque, synchronous frame speed, synthetic inertia, proportional gain, integral gain. Other parameters take the usual meaning as defined in other models.

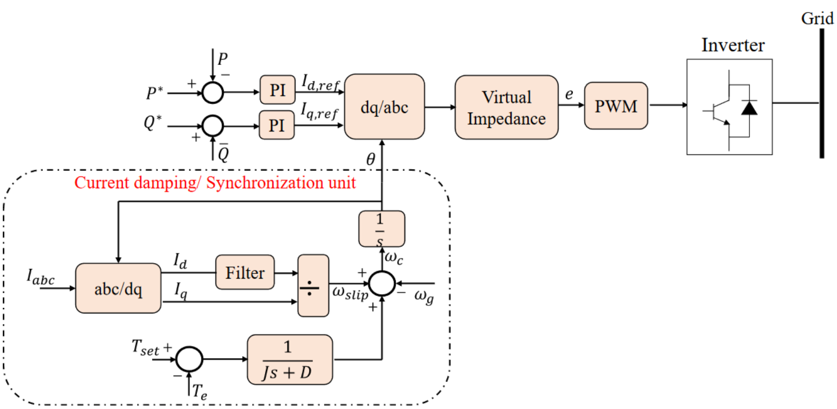

Figure 2.19. Inducverters [71]

2.4.8 Summary of the inertia control topologies

The key features of inertia control topologies have been discussed in the last section with their respective dynamic equations. In this section, the weaknesses of the topologies are highlighted as shown in Table 2.1 with the corresponding advances/improvements that have been exploited in the literature for each control scheme.

Table 2.1. Strength and weaknesses of traditional inertia control model and their advances

S/N	Inertia control model	Features/Strength	Drawbacks	Advances/improvements
1	OSAKA	1. Simple topology with a small size of control loops. 2. Grid forming capability [71], [41] 3. Frequency derivative introduces disturbances into the control, it is common in most of the control schemes but is eliminated here [71], [41].	1. Grid converter is susceptible to over current if fault occurs on the system and this is because of the unavailable dedicated current-control loop to regulate the line current [61]. This issue is synonymous to all voltage-controlled inverters [79, 80] 2. Oscillations in power and frequency , [80, 81] 3. Problem of numerical instability [41, 71] 4. Reactive power sharing inaccuracy is a major issue [62, 82] 5. Large changes in rotor speed during parallel operation of small ESM and distributed generator, most especially during load transition often degrade microgrid performance and also cause imbalance in ESM current [83]	1. The model in Ref. [24] was designed to incorporate an improved voltage dip ride through capability, and was evaluated for various voltage sag scenarios in [84] while a technique for reactive power sharing in a proportionate ratio to their sizes is investigated in [85] 2. In Ref. [62], an improved VSG control of OSAKA model is proposed where better transient power sharing is realized by altering the virtual stator-reactance using the concept of state-space model. 3. In Ref. [83], mechanism using the concept of Double-decoupled-synchronous-reference-frame and ESM negative sequence current suppression was presented to avoid unbalanced ESM current. 4.
S/N	Inertia control model	Features/Strength	Drawbacks	Advances/improvements

				5. The incorporated transient virtual stator impedance facilitates protection of inverter against overcurrent. 6. The issue of intrinsic low-frequency oscillations and oscillatory mode associated with OSAKA model is improved in [86] by adding a power quality compensation block as a state feedback to the traditional OSAKA control scheme. 7. In Ref. [87], the inertia control is designed such that the value of synthetic inertia is not constant but varies in a way as to reduce the relative virtual angular velocity $(w_m - w_g)$.
2	Synchronverter	1. PLL is used only for synchronization, so its effect of introducing a negative resistor effect that affects system stability is much avoided [80, 88]	1. The need of PLL for initial synchronization in feeble grid could make the system vulnerable to instabilities especially during faults [79, 81, 89].	1. Synchronverters have been improved and deployed in applications like single phase application [90], High voltage direct current system [91-93], STATCOM [94-96], self-synchronization capability [90, 97].
S/N	Inertia control model	Features/Strength	Drawbacks	Advances/improvements

		2. The fact that is voltage-source model means that it would have grid forming capability [41]. 3. While islanding, the rush current is slightly small because the output voltage and frequency are not significantly affected [98]. 4. Control realization is based on the second order characteristics of ESM [75] 5. 3-phase control model is based on non-salient pole rotor [71]. 6. Need for frequency derivative is eliminated [71]	2. For a self-synchronized model, PI controller performs the function of regulating the damping and ensuring a stable power control but on another hand, it raises the order of the closed-loop transfer function [75]. 3. The complexity of the involved differential equations employed in the control model might lead to numerical instability [75], [71] **4.** Because of its implementation as a voltage controlled model; it is without over-current protection and thus requires extra protection against grid transients [71]	2. Modifications in the form of virtual reactive components (L and C) & anti windup have been suggested to enhance the overall dynamic stability characteristics [99, 100]. Other improvements in synchronverter can be found in [100-105]. 3. A self-synchronized model was suggested in [78, 97] and this removes the necessity for PLL; this removes complications in the system model and enhances microgrid stability performance [71].
3	CVSM	1. Inertia emulation is achieved through swing equation.	1. Complex control algorithm 2. The optimization of all required machine parameters is a time-consuming task due to the non-linear coupling of the equations. 3. too many control variables will make the stability analysis cumbersome for multimachine cases 4. Has not been experimentally verified	1. Virtual impedance was introduced to uncouple reactive and active power [34, 106]. 2. Islanded operation is considered in [35] 3. The active droop controller dynamics is added to the control dynamics thus enhancing the operational flexibility of the microgrid [35, 106]

S/N	Inertia control model	Features/Strength	Drawbacks	Advances/improvements
			5. This control scheme is without outer active power control loop.	
4	VISMA (2-axis model)	Completely represent the model behavior of ESM	1. Unstable switching frequency because of rigid tolerance band [4, 20]. 2. The use of d-q transformation complicates real implementation 3. The optimization of all required machine parameters is a time-consuming task due to the non-linear coupling of the equations. 4. Underdamped response with high overshoot and oscillations in both frequency and power [29]. 5. Strong grid oscillation exists during operation in islanded mode which could lead to grid failure [4] 6. asymmetrical mains voltages [18].	The advances lead to the development of simplified abc VISMA model [20]
5	SVI-VISMA	1. The transient current is regulated close to zero using phase current controller, hence rush current is inherently guaranteed [20, 44]	1. Unstable switching frequency because of rigid tolerance band [4, 20]. 2. Lacks grid forming capability [44].	The use of large size of terminal capacitor and ensuring that cut-off frequency of the filter is less than minimum switching frequency of the phase controller will help to lower the grid-harmonics [20].

S/N	Inertia control model	Features/Strength	Drawbacks	Advances/improvements
		2. Capacitor is necessary at the VISMA inverter terminal if islanded mode is required but not necessary when in grid connected mode [20].	3. Large current ripples in steady state. 4. The modulation techniques produce a subharmonic component	
6	SIV-VISMA	1. Behaves in a similar fashion like real ESM even in the manner in which it is synchronized with the grid [20, 81] 2. PWM-controller ensures stable switching frequency of the VISMA converter [20]	1. It is vulnerable to instability because of the derivative term that may amplify perturbations [43] 2. Additional filter has a negative effect on the real time behavior of the control system including the bandwidth [43] 3. Because of its implementation as a voltage controlled model; it is without over-current protection and thus requires extra protection against grid transients [71, 79]. 4. The high harmonics present in the output current of the VISMA-inverter may intensify during grid disruptions, thereby impairing the controller's performance [43].	
7	SPC	1. Inertia emulation is achieved through swing equation [75], [81]	1. steady state error problem [107]. 2. Because of the lack of PLL for system frequency detection, grid	Flexible droop characteristic that eliminates the limitation of coupling between the damping and droop

S/N	Inertia control model	Features/Strength	Drawbacks	Advances/improvements
		2. Absence of discontinuities in the solution of the model equations eliminates the possible numerical instability problem [41]. 3. An optimized second-order equation was used to realize power loop controller, this thus subdues the inherited oscillations characterizing the swing equation [41]. 4. This control scheme avoids the need for extra filtering which therefore enhances the dynamic performance of the controller by enhancing its bandwidth. 5. Droop and damping parameters can be independently designed since they are not coupled and this enhances the dynamic performance	re-synchronization becomes challenging. Use of $w = 1$ may result in circulating current (during frequency grid deviation) which may be disastrous for the grid inverter [64]. 3. Control reconfiguration (switching) during islanding degrades smooth transitions particularly during faults [64]. 4. It is difficult to achieve control system parameter tuning because of the nested loop structure [41].	characteristics in the power regulating loop is presented in [108]. Besides, constant grid power is achievable irrespective of grid frequency variations. Detailed analysis of different power loop controllers is presented in [77, 109] while stability method of SPC is presented in [110]
8	VSYNC	1. Current source implementation, essential over-current protection (merit) [80].	1. Vulnerable to instability when used in weak grids due to the dynamics of PLL [41, 80], and is more serious if PI controller is employed to actualized inner	Modified dynamic equations that considers reactive power reference can be found in [72] and an idea to employ VSYNC as a voltage control

S/N	Inertia control model	Features/Strength	Drawbacks	Advances/improvements
		2. Quick reaction in tracking steady-state frequency [71]. 3. Easiest method of simulating inertia response [71].	current loop control [41]. Sophisticated PLL is thus necessary for hitch free operation [71]. 2. Because of the requirement for energy storage in the inertia control scheme [75], it becomes unsuitable for islanded operational mode [99]. 3. The control scheme is without AVR support facility [64]. 4. Inertia control is emulated during frequency perturbations but becomes difficult during input power variations [41]. 5. Execution time is lengthy [71]. 6. Noise disturbance may result in change in system characteristics [71, 80].	model is proposed in [29]. The idea of variable inertia controller to enhance the microgrid dynamic was presented in [111]. Fault ride through capability of VSYNC in Doubly fed induction generator (DFIG) based wind power system is investigated in [112] under the consideration of three phase symmetrical fault.
9	KHI	Extremely effective for unbalanced loads and abrupt changes in the grid operation [71].	1. It lacks inherent overcurrent capability [79]. 2. Reactive power sharing inaccuracy is a major issue [64].	Further development application wise have been reported. In Ref. [113], Double-decoupled-synchronous-reference-frame technique is adopted to control a single-phase inverter. Ripple current
S/N	Inertia control model	Features/Strength	Drawbacks	Advances/improvements

				compensation approach based on an adaptive virtual resistor is suggested in [114]. Small-signal modelling and parameter design is presented in [115]. A mathematical technique to reduce the frequency and voltage perturbations in the microgrid is presented in [116]. Current control model of KHI that replaces phase locked loop with rotor model is proposed in [79]. Low voltage ride through capability of KHI inertia-control scheme is presented in [117]
10	Inducverters	This scheme offers a real-time self-starting and auto-synchronization thus avoiding the necessity for a dedicated synchronizing block/PLL used in estimating the grid's parameters and aligning VSCs voltage-vector with the grid's voltage	1. High initial overcurrent inherited from the real induction machine is a major setback [89] 2. The use of adaptive compensator in the inner-control loop slows down grid voltage tracking of the set point value [89]. 3. Complicated analytical formulation due to adoption of hybrid abc-dq frame [89]. 4. Does not implement AVR.	1. The re-orientation of the hybrid-frame used in the controller to Synchronously-rotating Reference Frame (SRF) is achieved in [89] and thus simplifying model analysis. 2. Open loop control of current and voltage makes inertia control scheme vulnerable to undesirable transients during heavy grid disturbance [64].
S/N	Inertia control model	Features/Strength	Drawbacks	Advances/improvements
			5. Keeping the converter output power fixed regardless of the	

			magnitude of the voltage difference could result in negative resistance on the grid and thus degrade system stability [64]	

Table 2.2. Summarized comparison of inertia control topologies

Class of VSGs	VSG model	Frequency profile characteristics	Dedicated PLL	Seamless - Islanding transition capability	Self-synchronization capability	Fault ride through capability	Inherent overcurrent protection	Black start capability	Voltage control
SG model-based [80]	VISMA (dq-model)	Underdamped response with high overshoot & frequency oscillations [29].	Required [4]	Yes [4]	Not yet investigated	Not yet investigated	Yes [44]	Yes [4, 49],	Investigated [118].
Class of VSGs	VSG model	Frequency profile characteristics	Dedicated PLL	Seamless - Islanding transition capability	Self-synchronization capability	Fault ride through capability	Inherent overcurrent protection	Black start capability	Voltage control

SG model-based [80]	SVI-VISMA	underdamped with a limited overshoot, [29]	Required when outer control is incorporated.	Yes [20, 44, 49, 118]	Not yet investigated	Difficult to achieve according to [79]	Yes [44]	Yes [44]	Yes [118]
	SIV-VISMA	Damped frequency response [29]	Required when outer control is incorporated	Yes [20]	Not yet investigated	Not yet investigated	Voltage-source Implemented & as such no inherent over-current protection [80]	Not yet investigated	Yes [118]
	Synchronverter	Underdamped frequency response [29]	Required [76, 80].	Yes [75, 98, 119].	Yes [97]	Investigated in [120] as possible	Investigated in [120] as possible	Yes [121].	Yes [75]
	KHI	High oscillations in frequency [29].	Required [68, 80].	Yes [68]	Not investigated	Yes [117]	Present [68]	Yes	Present [116]
Class of VSGs	VSG model	Frequency profile characteristics	Dedicated PLL	Seamless - Islanding transition capability	Self-synchronization capability	Fault ride through capability	Inherent overcurrent protection	Black start capability	Voltage control

Swing equation Based [80]	SPC-SG	underdamped with a limited overshoot but more slower compared to SPC-PI & SPC-LL [29]	Not required [109, 110].	Yes [43, 75, 108].	Yes [76]	Yes [122, 123].	Present [41, 75]	Yes [64]	Present
	SPC-PI	underdamped with a limited overshoot [29]							
	SPC-LL								
	OSAKA	Damped frequency response [29]	Required [80]	Yes [83, 86]	Not investigated	Yes [24]	Voltage-source implementation; no over-current [79, 80]	Yes [64]	Yes [29]
Class of VSGs	VSG model	Frequency profile characteristics	Dedicated PLL	Seamless - Islanding transition capability	Self-synchronization capability	Fault ride through capability	Inherent overcurrent protection	Black start capability	Voltage control

Frequency-power response based	VSYNC	Excellent behavior	Needed [71, 80].	Not capable [41, 99].	Not investigated	Yes, as investigated in [112]	Present [44, 71]	Not investigated	Absent
	CVSM	underdamped with a limited overshoot, good settling time and damping [29]	Present [35]	Yes [35]	Present [29]	Present [124]	Present [124]	Possible	Present
Induction machine	Inducverters	Excellent response with no overshoot and high settling time	No [75, 89],	Not yet investigated	Yes [89]	generate constant power under disturbances or grid faults [75].	Current damping but no overcurrent protection	Yes [125] but No (in grid following mode) [89]	Yes [89]

3 Stability Analysis Tools in Modern Power System

3.1 Introduction

When stability analysis is to be carried out on a power grid, it is desirable to be pragmatic while developing an extensive power system model so that the relevant dynamics can be correctly captured and simulated under a desired simulation completion time. In the stability analysis of a multimachine power system with a significant level of distributed energy, different computational tools have been developed to study the interactions between different units of the microgrid system. The analytical approach used may be determined by the control architectures of the grid converters and also by the form of network disturbances. Some of these techniques are; model reduction technique, coherency and aggregation (CA) technique [126]. The CA technique is based on the inherent characteristics, such as network admittances, generator inertias, and loads to obtain a reduced model in the form of non-linear power systems [127]. The model reduction technique simplifies the power system representation while still maintaining system dynamic responses. This method has recently being employed in [128] and [129]. In this chapter, relevant mathematical tools for stability analysis are presented with a special focus on selective modal analysis, transition matrix and linearized small-signal model.

3.2 Small-signal linearized model of dynamic power system

Small-signal investigation of power system is predicated on obtaining a linearized dynamic model and this offers systematic means of not only providing stability assessment (e.g. via eigenvalue analysis) of the system but also introduces an effective way of obtaining controller parameters. Small-signal models are generally represented in state-space form where all the dynamics of every component are captured. Small-signal models are usually developed using a state-space representation of the network, where generic models for the different power system components are commonly available. Based on the state space model, standard control engineering tools are then applied to carry out stability assessment. With this increase in inverter-based power grid, it is critically more necessary to develop small-signal model as they are even more vulnerable to instabilities. Unfortunately, converter control schemes are often secured with intellectual properties (IP) personalized by the manufacturers, thus making the state space tasking [130]. The general mathematical expression that governs the internal dynamics of the associated components of the microgrid including the VISMAs, the control dynamics, loads etc. is defined by the n^{th} first order nonlinear differential algebraic equation (DAE) and r^{th} outputs as follows [131, 132]:

$$\dot{x}_i = f_i(x_1, x_2, \dots x_n;\ u_1, u_2, \dots u_r; t),\ \ y_i = g_i(x_1, x_2, x_3, \dots x_n;\ u_1, u_2, u_3, \dots u_r; t) \quad (3.1)$$

Where g_i denotes the set of algebraic functions, f_i represents set of nonlinear differential functions characterizing the system, x_i is a state variable, u_i defines the input state variable, and *t* is the time. The element $\dot{x}_i$ defines the time-derivatives of the state variables [27] and is represented in a simplified form as

$$\dot{\boldsymbol{x}}_i = \boldsymbol{f}(\boldsymbol{x}, \boldsymbol{u}) \quad (3.2)$$

where $\boldsymbol{x} = [x_1 \quad x_2 \dots \quad x_n]^T$ $\boldsymbol{u} = [u_1 \quad u_2 \dots \quad u_n]^T$.

Linearization of a dynamical system is a linear estimation of a non-linear system around given stationary points, the approximation in microgrid is effective only if the deviation in characteristics to the nominal operating mode after grid disturbances is negligibly small [53, 133]. Fig. 3.1 is an illustrative example of linearization. If we assume that point B is within the linearized region then the behaviour of the system at point A in the figure is approximated as that at point B. If x_0, u_0 defines the stationary operating point, then (3.2) is now defined as:

$$\dot{\boldsymbol{x}}_0 = \boldsymbol{f}(\boldsymbol{x}_0, \boldsymbol{u}_0) = 0 \quad (3.3)$$

Before proceeding with the linearization of the nonlinear power system dynamics in state-space representation, it is necessary that the stationary operating points are first evaluated. The steady-state is obtained by solving the dynamic equations for $\dot{x} = 0$ (i.e. (3.3)). The stationary operating points of the system variables are realized by providing the necessary reference signals and x_o, u_o. If slight perturbation is introduced in the system which may be through the change in input variables or change in state variables then, RHS in (3.2) is linearized by applying Taylor series expansion as follows [134]:

$$\dot{x}_i = f(x,u) \approx f(x_o,u_o) + \frac{\partial f}{\partial x}\bigg|_{\substack{x=x_o\\u=u_o}}(x-x_o) + \frac{\partial f}{\partial u}\bigg|_{\substack{x=x_o\\u=u_o}}(u-u_o) + \frac{\partial^2 f}{\partial x^2}\bigg|_{\substack{x=x_o\\u=u_o}}(x-x_o)^2 + \frac{\partial^2 f}{\partial u^2}\bigg|_{\substack{x=x_o\\u=u_o}}(u-u_o)^2 + \cdots \quad (3.4)$$

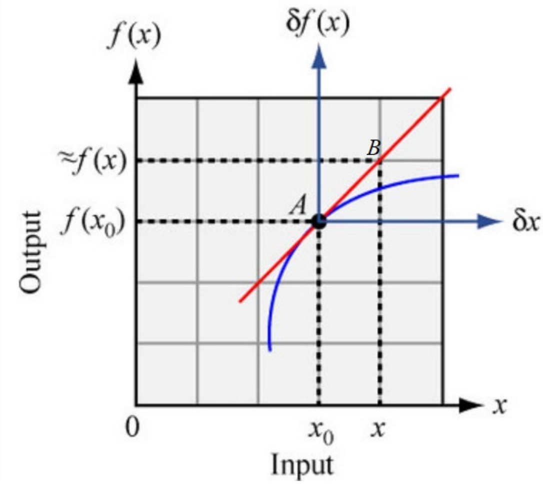

Figure 3.1. Illustrative example of linearization in dynamical systems [135]

f the higher order 2 and above is to be neglected and assuming that

$$A = \frac{\partial f}{\partial x}\bigg|_{\substack{x=x_o\\u=u_o}}, B = \frac{\partial f}{\partial u}\bigg|_{\substack{x=x_o\\u=u_o}} \quad (3.5)$$

n we have:

$$\Delta\dot{x} = A(x-x_o) + B(u-u_o) \quad (3.6)$$

Let the variable variations be defined as; $\delta x = \Delta x = x - x_o$ or $x = x_o + \Delta x$ and $\delta u = \Delta u = u - u_o$ or $u = u_o + \Delta u$. In the linear approximation, the behaviour of n-VISMA microgrid around a stationary point is detailed by the following set of differential equations:

$$\boldsymbol{\Delta\dot{x}} = \boldsymbol{A\Delta x} + \boldsymbol{B\Delta u} \quad (3.7)$$

The elements in matrices **A** and **B** depend on the initial steady state operating condition. Elements of **A** are partial derivatives of functions f_i with respect to the state variables x_i while elements of **B** matrix are partial derivatives of f_i with respect to u_i and are defined as follows [27]:

$$A = \begin{bmatrix} \frac{\partial f_1}{\partial x_1} & \cdots & \frac{\partial f_1}{\partial x_n} \\ \vdots & \ddots & \vdots \\ \frac{\partial f_n}{\partial x_1} & \cdots & \frac{\partial f_n}{\partial x_n} \end{bmatrix}_{dim=\,n\times n} \qquad B = \begin{bmatrix} \frac{\partial f_1}{\partial u_1} & \cdots & \frac{\partial f_1}{\partial u_r} \\ \vdots & \ddots & \vdots \\ \frac{\partial f_n}{\partial u_1} & \cdots & \frac{\partial f_n}{\partial u_r} \end{bmatrix}_{dim=\,r\times r} \tag{3.8}$$

A is called the system matrix and its eigenvalues at stationary condition (x_o, u_o) can be used to characterize the stability of the dynamical microgrid. Let $\lambda_i = \sigma_i \pm jw_i$ be a complex conjugate solution that satisfies (3.7), then the frequency of oscillation of the corresponding i^{th} mode is defined as [136]:

$$f_i = \frac{w_i}{2\pi}, Hz \tag{3.9}$$

The damping ratio (ξ_i) is given as [27, 131]:

$$\xi_i = -\frac{\sigma_i}{\sqrt{\sigma_i^2 + w_i^2}} \tag{3.10}$$

The power system is considered to be poorly damped when its $\xi_i < 5\%$.

3.3 Modal analysis in virtual rotor angle small-signal analysis

Rotor angle stability entails the study of electromechanical vibrations that occur in the virtual rotor due to grid disturbances [137]. The oscillations may be as a result of feeble electrical ties between the VISMAs, or between VISMAs and the connected loads due to a long transmission length (amounting to massive reactance), or on the grounds of uncoordinated highly responsive controllers [27]. To study the magnitude of the rotor swinging as a result of grid disturbances modal analysis is adopted. Oscillatory modal analysis is the most modern and widely used technique in power system stability investigation [138]. Modal analysis is a frequency domain approach that is particularly useful for characterizing the small signal stability of a linearized power system model around its steady state operating point. It makes it possible to quickly identify groups that exhibit similar behaviours and to clearly define each group's responsibility. Many details about these oscillations may be found in the stability studies of a power system around its equilibrium point prior to any disturbances, including the number of inter-area modes the system has, their frequency, and their damping. In addition, it aids in the improvement of modes that are adversely or insufficiently damped [139]. The technique entails decomposition of grid oscillations into separate components [138]. Modal analysis involves evaluating the eigen properties of the Jacobian matrix to investigate the static stability of the microgrid dynamic. Eigenvalue analysis simplifies the static stability of the microgrid by representing the disturbances' responses as a linear combination of uncoupled aperiodic and oscillatory responses [54]. The nature of the rotor swing is determined by modes of the system matrix. Laplace transform of (3.7) yields:

$$\Delta \boldsymbol{X}(\boldsymbol{s}) = (\boldsymbol{sI} - \boldsymbol{A})^{-\mathbf{1}}[\Delta \boldsymbol{X}(\mathbf{0}) + \boldsymbol{B}\Delta \boldsymbol{u}(\boldsymbol{s})] = \frac{\mathbf{Adj}(\boldsymbol{sI}-\boldsymbol{A})}{\mathbf{det}(\boldsymbol{sI}-\boldsymbol{A})}[\Delta \boldsymbol{X}(\mathbf{0}) + \boldsymbol{B}\Delta \boldsymbol{u}(\boldsymbol{s})] \tag{3.11}$$

The poles of $\boldsymbol{X}(\boldsymbol{s})$ are the roots of the equation i.e.

$$\det(\boldsymbol{sI} - \boldsymbol{A}) = 0 \tag{3.12}$$

The values of Laplace function $\boldsymbol{s}$ that satisfy (3.12) are the eigenvalues of the Jacobian matrix $\boldsymbol{A}$. Thus, the following criteria are used to characterize the microgrid's stability [40], [136]:

i. The microgrid is stable if ALL the eigenvalues of system matrix **A** are NEGATIVE
ii. The power system is UNSTABLE if at least one real part is POSITIVE
iii. If at least one σ of the eigenvalue is ZERO, then the system is CRITICALLY STABLE and no conclusion can be made
iv. The farther the negative real part from the ORIGIN, the faster the oscillatory responses decays to ZERO.

The above points i – iv, are illustrated by the complex plane in Fig. 3.2.

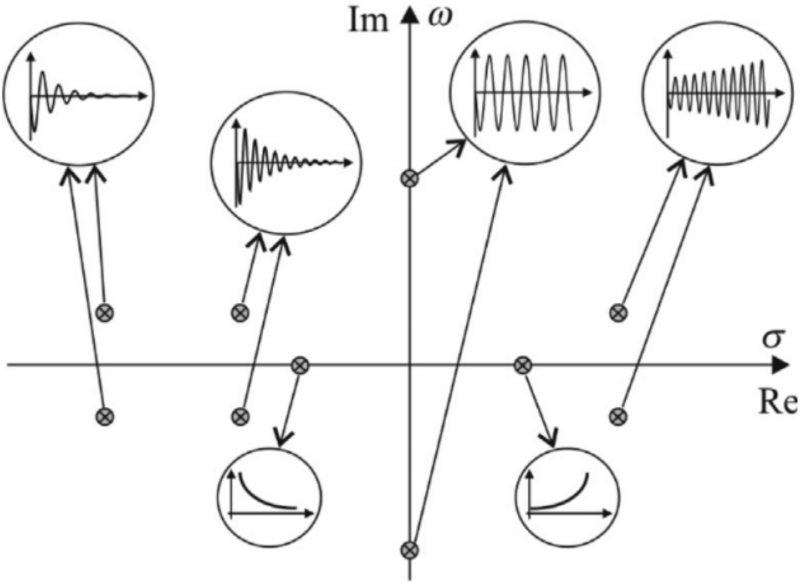

Figure 3.2. Mode type description on the complex plane [27]

Since $s = \lambda$, then we can write:

$$\det(\boldsymbol{A} - \lambda \boldsymbol{I_n}) = 0 \tag{3.13}$$

Where $\boldsymbol{I_n} \in \boldsymbol{R}^{n \times n}$ is called the identity matrix, and (3.13) is termed the characteristic equation of the Jacobian matrix. For any λ_i, there exists a non-zero right eigenvector Φ_i satisfying

$$\boldsymbol{A\phi_i} = \boldsymbol{\phi_i}\lambda_i \quad i = 1,2, \dots . n \tag{3.14}$$

Equation (3.14) shows that eigenvectors are not unique as they can be rescaled by multiplying or dividing their elements by a nonzero number. From (3.14), we can write:

$$\begin{cases} \boldsymbol{A\phi_1} = \boldsymbol{\phi_1}\lambda_1 \\ \boldsymbol{A\phi_2} = \boldsymbol{\phi_2}\lambda_2 \\ \quad\vdots \\ \boldsymbol{A\phi_n} = \boldsymbol{\phi_n}\lambda_n \end{cases} \tag{3.15}$$

Equation (3.15) can further be expanded as follows:

$$\boldsymbol{A}[\boldsymbol{\phi_1} \quad \boldsymbol{\phi_2} \quad \cdots \quad \boldsymbol{\phi_n}] = [\boldsymbol{\phi_1} \quad \boldsymbol{\phi_2} \quad \cdots \quad \boldsymbol{\phi_n}] \begin{bmatrix} \lambda_1 & 0 & \cdots & 0 \\ 0 & \lambda_2 & \vdots & 0 \\ \vdots & \vdots & \ddots & \vdots \\ 0 & 0 & \cdots & \lambda_n \end{bmatrix} = \boldsymbol{\Lambda} = \mathrm{diag}(\lambda_i),$$

Or, $\boldsymbol{A\Phi} = \boldsymbol{\Phi\Lambda}$ (3.16)

where; $\boldsymbol{\Phi} = [\boldsymbol{\phi_1} \quad \boldsymbol{\phi_2} \quad \cdots \quad \boldsymbol{\phi_n}]$, $\boldsymbol{\phi_i} = \begin{bmatrix} \boldsymbol{\phi_{1i}} \\ \boldsymbol{\phi_{2i}} \\ \vdots \\ \boldsymbol{\phi_{ni}} \end{bmatrix}$, where $\boldsymbol{\phi_i}$ is a column vector

$\boldsymbol{\Phi}$, is a square matrix and if its elements are linearly independent then matrix Φ is non-singular and its inverse, ($\boldsymbol{\Phi^{-1}}$) exist.

Pre-multiplying (3.16) by $\boldsymbol{\Phi^{-1}}$ and then right multiply the resulting expression by $\boldsymbol{\Phi^{-1}}$ yield;

$$\boldsymbol{\psi A \Phi} = \boldsymbol{\Lambda} \tag{3.17}$$

where $\boldsymbol{\psi} = \boldsymbol{\Phi^{-1}}$, is termed the left eigenvector which is a row vector and is defined as:

$$\boldsymbol{\psi} = [\,\boldsymbol{\psi_1} \quad \boldsymbol{\psi_2} \quad \cdots \quad \boldsymbol{\psi_n}]^{\boldsymbol{T}} = \left[\boldsymbol{\psi_1}^{\boldsymbol{T}} \quad \boldsymbol{\psi_2}^{\boldsymbol{T}} \quad \cdots \quad \boldsymbol{\psi_n}^{\boldsymbol{T}}\right]^{\boldsymbol{T}}, \boldsymbol{\psi_i} = [\boldsymbol{\psi_{i1}} \quad \boldsymbol{\psi_{i2}} \quad \cdots \quad \boldsymbol{\psi_{in}}]$$

If all the eigenvalues assume unequal values i.e. $\lambda_1 \neq \lambda_2 \ldots \neq \lambda_n$, then the corresponding eigenvectors are linearly independent. If ψ and Φ are normalized, then

$$\boldsymbol{\psi}.\boldsymbol{\Phi} = 1 \tag{3.18}$$

3.4 Time domain analysis via state transition matrix

Electrical power systems are generally complex and highly non-linear. The static stability of the non-linear system is entirely dependent on the nature, size of the inputs and the initial operating condition. By linearizing the nonlinear model around an equilibrium point, it is possible to use the linear dynamics to analyse stability of nonlinear systems within a given linear region. In contrast to nonlinear stability analysis, linear dynamic system is fully independent of the input and as such the state of a stable system having absolutely no input is surely expected to relapse to the origin [40]. Solution to a heterogenous state equation in (3.7) if the initial time is t_0 instead of 0 starting point is expressed as follows:

$$\Delta x(t) = e^{\boldsymbol{A}(t-t_0)}\Delta x(0) + \int_{t_0}^{t} e^{\boldsymbol{A}(t-\tau)}\boldsymbol{B}\Delta u(\tau)\, d\tau \qquad (3.19)$$

If a free motion dynamic (null input) is considered then (3.7) reduces to

$$\Delta\dot{\boldsymbol{x}} = \boldsymbol{A}\Delta\boldsymbol{x} \qquad (3.20)$$

Solution of (3.20) is given by $\Delta x(t) = e^{\boldsymbol{A}t}\Delta x(0)$. $e^{\boldsymbol{A}t}$ is called matrix exponential or state transition matrix and is of dimension $n \times n$ while $\Delta x(0)$ defines the initial condition. In a complex power system, evaluating $e^{\boldsymbol{A}t}$ may take a long time or may even cause the program to hang if not well structured. Also, in (3.20), each first order differential equation is a linear combination of all the state variables in the system. Due to this cross coupling of state variables, it is difficult to identify those parameters that greatly influence the dynamic performance of a particular state variable. It is thus necessary to decouple these state variables.

If $\Delta x = \boldsymbol{\Phi} z$ is a linear transformation equation, then

$$\Delta\dot{z} = \boldsymbol{\Lambda}\Delta z \qquad (3.21)$$

$$\Delta x(t) = \boldsymbol{\Phi} \boldsymbol{e}^{\Lambda t}\boldsymbol{\psi}\Delta\boldsymbol{x}(\boldsymbol{0}) \qquad (3.22)$$

$$\text{where } \Delta x(t) = \begin{bmatrix} x_1(t) \\ x_2(t) \\ \vdots \\ x_n(t) \end{bmatrix}, \Delta x(0) = \begin{bmatrix} \Delta x_{10}(t) \\ \Delta x_{20}(t) \\ \vdots \\ \Delta x_{n0}(t) \end{bmatrix}, e^{\Lambda} = \begin{bmatrix} e^{\lambda_1 t} & 0 & \cdots & 0 \\ 0 & e^{\lambda_2 t} & \vdots & 0 \\ \vdots & \vdots & \ddots & \vdots \\ 0 & 0 & \cdots & e^{\lambda_n t} \end{bmatrix} \qquad (3.23)$$

$x_i(t)$ and $x_{i0}(t)$ respectively defines the time response and the initial state of the i^{th} state variable. If the eigenvalues are distinct i.e. $\lambda_1 \neq \lambda_2 \neq \cdots \lambda_n$, then $e^{\boldsymbol{A}t}$ is represented as in (3.23). However, if there is multiplicity in a particular eigenvalue i.e. $\lambda_i = \lambda_1, \lambda_2, \lambda_2, \lambda_2, \lambda_3, \lambda_4 \ldots \lambda_n$, then e^{Λ} will have other terms like $te^{\lambda_2 t}$, $t^2 e^{\lambda_2 t}$ in addition to the normal $e^{\lambda_1 t}, e^{\lambda_2 t}$, $e^{\lambda_3 t}, e^{\lambda_4 t}, e^{\lambda_n t}$ [140].

To illustrate a numerical time domain analysis using eigenvalues and eigenvectors, the IEEE-9 bus VISMA microgrid with extended virtual buses shown in Fig. 3.3 has been considered for analysis. In this example case, all initial conditions are assumed equal to 1, definitely $\Delta x_{i0}(t) \neq 0$.

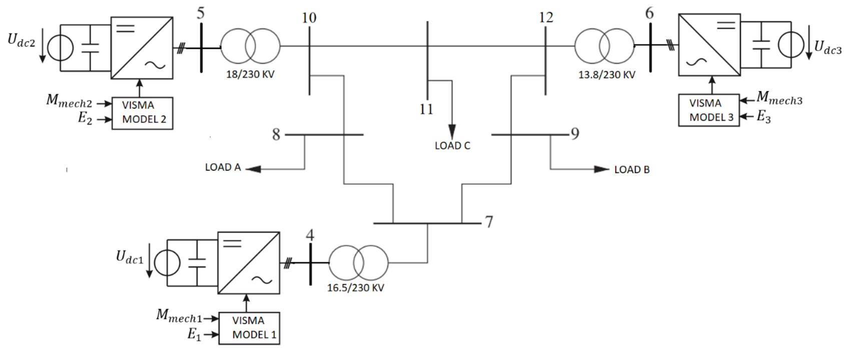

Figure 3.3. VISMA model with external power loop control

In Fig. 3.4 (a), zero equal damping is demonstrated for all VISMAs on the microgrid. This results in undamped (sustained) oscillations in both frequency and the virtual rotors. Though, it is much expected that the behaviour in both frequency and rotor must be similar due to their mathematical relationship, the result reveals that studying grid stability using rotor characteristics is much better due to the magnified oscillations they exhibit rather than using the frequency. In Fig. 3.4 (b), equal damping case of 4 was used for all the three VISMAs and this results in underdamped characteristics in both frequency and relative rotor angles. System behaviours in Fig. 3.4 (a and b) show that when damping is large, the perturbations in the system are damped faster. Increasing damping to damped out oscillations may also have a limitation, as its adjustment must always be considered in line with the particular inertia of the machine to avoid synchronizing time problem. This scenario is demonstrated in Fig. 3.4 (c and d), it is shown that, the time taken for the VISMAs to synchronize after perturbation increases when large damping values are used. This problem is majorly caused

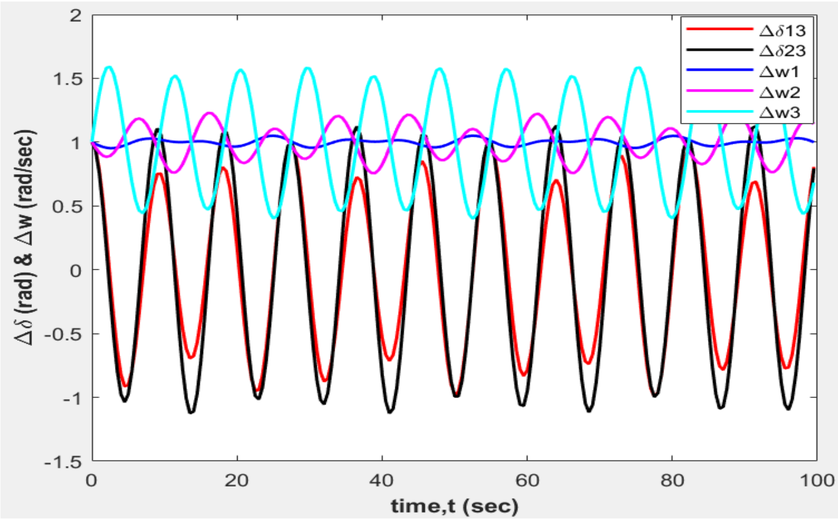
Δδ13
Δδ23
Δw1
Δw2
Δw3
Δδ (rad) & Δw (rad/sec)
time,t (sec)

(a)

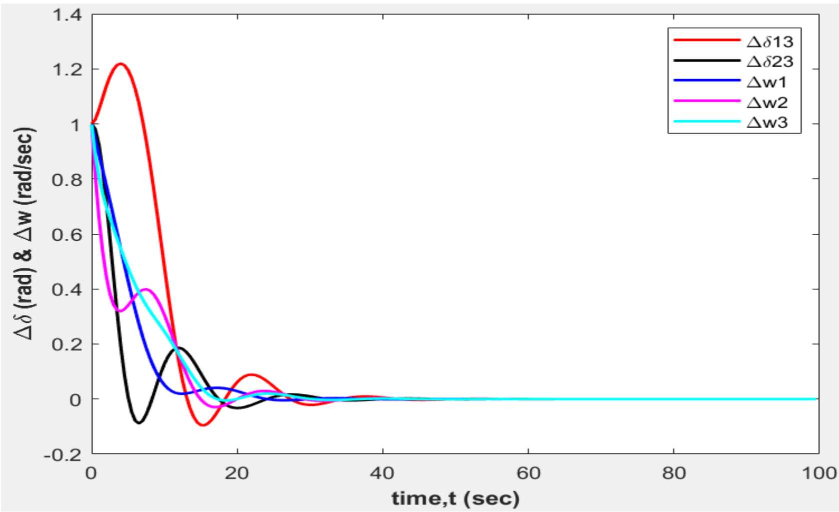
Δδ13
Δδ23
Δw1
Δw2
Δw3
Δδ (rad) & Δw (rad/sec)
time,t (sec)

(b)

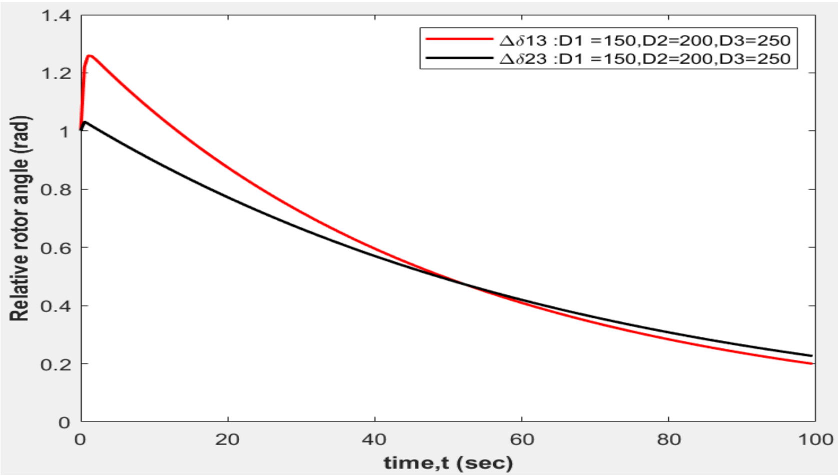
Δδ13 :D1 =150,D2=200,D3=250
Δδ23 :D1 =150,D2=200,D3=250
Relative rotor angle (rad)
time,t (sec)

(c)

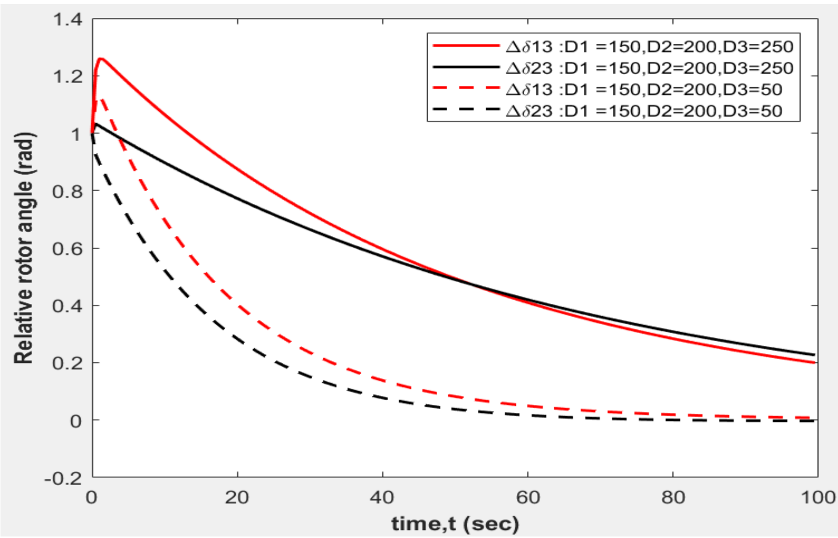
Δδ13 :D1 =150,D2=200,D3=250
Δδ23 :D1 =150,D2=200,D3=250
Δδ13 :D1 =150,D2=200,D3=50
Δδ23 :D1 =150,D2=200,D3=50
Relative rotor angle (rad)
time,t (sec)

(d)

Figure 3.4. *Time domain analysis with eigenvalues and eigenvectors for (a)* $D_i = 0$ *(b)* $D_i = 4$ *(c) homogenous and increased heterogenous damping cases (d) demonstrating reduced effect of* D_3 *from 250 to 50*

by an over increased ratio of damping to inertia i.e. $\frac{D_i}{T_{ai}}$ (where $i = 1,2,3..n$). VISMA 3 is having the largest damping to inertia ratio of 41.53 compared to VISMA1 with 3.172 and VISMA 2 with 15.625. Let's say D_3 is reduced to 50 from 250 so that its new ratio now becomes 8.31, then re-running the program yields the result in Fig. 3.4 (d) which clearly shows that synchronizing time will improve after grid disturbances.

3.5 Eigenvalue sensitivity for controller design

For a set of initial system conditions, it is often of interest to know how power system dynamics will react to change in some key system parameters or a particular disturbance scenario. During power system designs, some parameters are typically assumed with no proper idea on how the system is going to be impacted. Controller design in a complex modern power grid is one of these challenging tasks that need to be carefully undertaken if microgrid stability is to be ascertained under all disturbance conditions. Since power systems are generally nonlinear, controller designs could be achieved through a linearized model of nonlinear model by adopting some special techniques. Such techniques take care of relevant dynamics and details. However, in order to obtain controller parameters for optimal operation of the microgrid, first-order eigenvalue sensitivity have become a universally accepted tool. Couple of reasons justify its popularity: practicability, user-friendliness, simplistic nature etc [141]. To derive the sensitivity of the eigenvalues to the system parameters we may assume that the eigenvalues and eigenvectors vary continuously with respect to the elements of the system matrix **A**, so that perturbation equation is formulated for (3.14) [53, 142]. Taking the partial derivative of (3.14) with respect to system parameter β_{kj} (i.e. parameter β in k^{th} row and j^{th} column) using chain rule, we obtain the following [53]:

$$\frac{\partial \boldsymbol{A}}{\partial A_{kj}}\boldsymbol{\Phi_i} + \boldsymbol{A}\frac{\partial \boldsymbol{\Phi_i}}{\partial A_{kj}} = \frac{\partial \lambda_i}{\partial A_{kj}}\boldsymbol{\Phi_i} + \lambda_i\frac{\partial \boldsymbol{\Phi_i}}{\partial A_{kj}} \tag{3.24}$$

Collecting like terms and pre-multiplying each term of (3.14) with left eigenvector $\boldsymbol{\psi_i}$, yields:

$$\frac{\partial \boldsymbol{A}}{\partial A_{kj}}\boldsymbol{\Phi_i} + \boldsymbol{\psi_i}[A - \lambda_i \boldsymbol{I}]\frac{\partial \boldsymbol{\Phi_i}}{\partial A_{kj}} = \frac{\partial \lambda_i}{\partial A_{kj}}\boldsymbol{\Phi_i} \tag{3.25}$$

It is quite well established that $[\boldsymbol{A} - \lambda_i \boldsymbol{I}] = 0$ and using (3.20) in addition yield the following from (3.27);

$$\frac{\partial \lambda_i}{\partial A_{kj}} = \boldsymbol{\psi_i} \frac{\partial \boldsymbol{A}}{\partial A_{kj}} \boldsymbol{\Phi_i} \tag{3.26}$$

However, if all elements of $\frac{\partial \boldsymbol{A}}{\partial A_{kj}} = 0$ except the element in k^{th} row and j^{th} column, then (3.26) becomes;

$$\frac{\partial \lambda_i}{\partial A_{kj}} = \boldsymbol{\psi_{ki}}.\boldsymbol{\Phi_{ij}} \tag{3.27}$$

It is possible that the system matrix element $\boldsymbol{A}_{kj}$ in (3.28) is a function of system component parameter β i.e $\boldsymbol{A}_{kj} = f(\beta)$ or more likely that elements of matrix **A** are functions of same parameter β, then the eigenvalue sensitivity is obtained by taking the partial derivatives of the function in each row and column accordingly. However, based on the pointing direction of the parameter sensitivity and its value size, it can be determined whether the controller parameter so initially selected is suitable to achieve proper regulation or not [141]. System responses can thus be improved if need be.

4 Steady State Operating Points of Autonomous Microgrid

4.1 Introduction

Before starting the stability analysis of a multi-virtual synchronous machine (*n*-VISMA) power system, it is necessary to obtain the steady state operating points (SSOP) of all dynamic nodes in the network. The modified traditional iterative schemes using the concept of droop bus technique in an autonomous/islanded microgrid (IM) are not feasible for load flow analysis of VISMA microgrids incorporating no control dynamics. This chapter discusses a closed-form steady-state, fundamental-frequency model for an autonomous VISMA microgrid using the concept of a virtual swing bus.

4.2 State of the art load flow algorithms

The introduction of VISMA and droop control schemes in IBG brings along some technical and analytical challenges in the formulation of power flow solutions for the microgrid. Load flow study plays a significant role during system scheduling, network extension, and optimal operation of the microgrid [143]. It is useful in obtaining the stationary operating points at all buses in the multimachine power system [142]. However, the conventional means of iterative solutions like Gauss-Siedel and Newton-Raphson are not suitable for load-flow analysis of an autonomous microgrid because of the absence of slack bus. The line reactances is not constant but vary with the system frequency [144, 145]. A quiet number of analytical models have been developed to study the power flow characteristics of an autonomous microgrid. Load flow analysis in autonomous microgrid was formulated in [146, 147] using the traditional iterative method. The authors failed to consider the operational behaviour of IM with decentralized droop control but rather considered the DG bus with maximum capacity as the swing bus and the other buses as either PV or PQ buses. This assumption is not practicable as the DG units are generally of micro sources and do not have the capability to act as an infinite bus to keep-hold the system frequency and its local voltage constant. An improved backward/forward sweep (BFS) approach was proposed in [148]. This method has a high computational efficiency and good solution accuracy but it is only suitable for radial distribution and weakly meshed systems with singular power source and could be subjected to convergence issues when used in multisource microgrid [149]. Ref. [149] also considers a slack node and other nodes as PQ nodes which is an invalid assumption in an autonomous microgrid. As mentioned in [150], their application is limited to grid connected systems and cannot be directly applied to DG with droop characteristics.

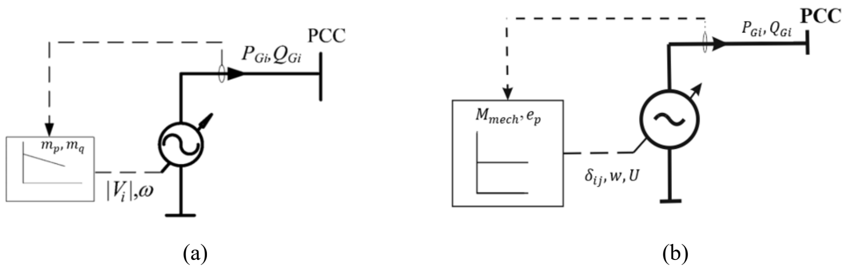

Figure 4.1. Steady state operating points models for islanded microgrid (a) Existing droop bus technique [143, 145, 149-151] (b) Proposed virtual swing bus model

Droop bus technique was introduced (see fig. 4.1 (a)) in addition to the conventional PV and PQ buses [143, 145, 149-151] for a load flow solution of an IM considering the droop characteristics of the DGs. In [149], a generalized 3-φ power flow algorithm for IM using globally convergent Newton trust method was suggested. This algorithm solves sets of non-linear equations and demands the evaluation of the *'Hessian matrix'* in addition to the state matrix and this makes the computation very complex. This method in [149] is exquisitely sensitive to the initial configuration of the problem variables [152]. An improved modified Newton-Raphson (IMNR) method for load flow was suggested in [151], it extended the conventional Newton–Raphson method to the autonomous case with complex loads. A number of models have also been developed from the angle of evolutionary-based methods which are unconstrained with the initial-values of the problem variables. Elrayyah *et al.*, suggested a power flow technique for a droop based islanded microgrid using the concept of particle swarm optimization (PSO) to select the voltage droop parameters that optimize reactive power sharing among the DGs for all loading conditions [153]. Though the model of Elrayyah is effective and allows for stability testing of the microgrid, it does fail to calculate active power sharing among the DGs. Guaranteed convergence PSO with Gaussian mutation was proposed in [152]. However, the effectiveness of metaheuristic techniques depends on the selection of parameters. A Homotopy-based method to provide solution to load flow of droop controlled IM is presented in [154].

The droop bus models discussed in the last paragraph are only valid for DGs that solely incorporate droop control schemes and cannot provide complete steady state operating points of SVI-VISMA model especially when in its natural state. SVI-VISMA in its natural state does not implement a governor and hence does not actuate a primary frequency control but nevertheless, an external droop controller can be added. SVI-VISMA has an inherent droop characteristic and, thus possess the capability to maintain network synchronization without externally added droop control.

In this research, a novel virtual bus technique based on the principle of swing equation to obtain the SSOP of all dynamic nodes in autonomous VISMA microgrid is considered (see fig. 4.1 b). This proposed concept employs the use of constant amplitude of virtual excitation and virtual torque localized to each VISMA unlike the droop bus approach that uses active and reactive power coefficients as major constant control parameters.

The proposed load flow technique for VISMA microgrid further considers the following conditions:

1. The steady operating points of buses are independent of the characteristics of the interface power electronic converter, distributed energy resources and network filter.
2. There is no slack bus, so any bus on islanded (SVI-VISMA) microgrid system could serve as a reference bus. The voltage at all buses are variables except the virtual buses in which the pole wheel voltages are prespecified. The system frequency is global and also a variable.
3. All SVI-VISMA buses are governed by swing equation. Either the terminal bus or the internal bus could act as the 'virtual swing bus'. Note that the designated virtual swing bus here does not have the capability to maintain system frequency. If the internal bus is taken as the virtual swing bus, then the active and reactive power at the terminal bus is determined by considering the active and reactive losses in the virtual stator.
4. VISMA internal bus cannot be classified as slack, PV, or PQ buses since the parameters are not pre-specified, though the pole wheel voltage is known but the active power P, Q and pole-wheel angle on the bus is not known but to be determined via iterative scheme.

The obtained load flow solution is thus useful in the steady stability analysis of VISMA. The usual question about whether IBG can effectively replace the traditional generation scheme is also answered in this dissertation. The effectiveness of the proposed algorithm is validated by comparing the results obtained with that obtained from time domain analysis using SIMULINK.

4.3 Microgrid System Modelling

4.3.1 VISMA system

A schematic of VISMA system without excitation control and governor dynamics is shown in Fig. 4.2. The system consists of a DC voltage intermediate circuit to which either an energy storage device or a combination with one or more DC voltage generators is connected, a self-commutated, fast-switching, three-phase inverter, a phase current regulator, a process computer on which a model to simulate the synchronous machine runs, an LC output filter and the current and voltage transducer for measuring the network-side operating parameters. The virtual bus is designated with red line in Fig. 4.2.

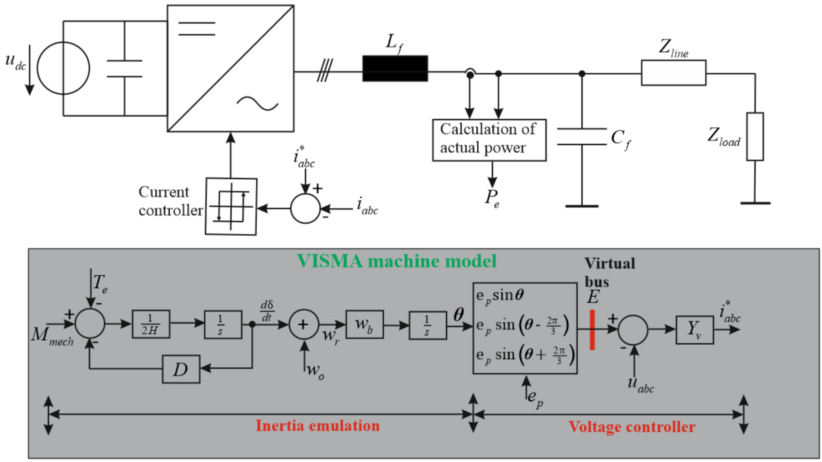

Figure 4.2. Block diagram representation of VISMA

4.3.2 Static Load Modelling

In large scale power system stability studies loads are typically aggregated at bulk supply substations. In rotor-angle stability studies a static representation of loads is commonly employed. A static load model describes the behaviour of loads at any point in time as algebraic functions of system frequency and load bus voltage at that instant. The active power P and reactive power Q delivered to the load are represented independently by the following frequency dependent load model [40, 155]:

$$P_{Li} = P_{Lo,i}\left(\frac{U_i}{U_o}\right)^{\alpha}\left(1 + K_{pf}\Delta w\right) \tag{4.1}$$

$$Q_{Li} = Q_{Lo,i}\left(\frac{U_i}{U_o}\right)^{\beta}\left(1 + K_{qf}\Delta w\right) \tag{4.2}$$

Where Δw is the angular frequency deviation $(w - w_o)$, $P_{Lo,i}$ and $Q_{Lo,i}$ are the active and reactive power at initial steady state operating points, U_o is the nominal voltage, K_{pf} and K_{qf} are frequency sensitivity parameters and respectively ranges between 0 to 3.0 and -2.0 to 0 respectively [149]. The exponent values for different categories of loads are given in Table 4.1.

Table 4.1. Load types and exponent values [143]

Load type (L_T)	α	β
Constant Power (KP)	0.00	0.00
Constant current (KC)	1.00	1.00
Constant Impedance (KI)	2.00	2.00
Residential load (RL)	0.92	4.04
Commercial load (CL)	1.51	3.40
Industrial load (IL)	0.18	6.00
Typical load (TL)	0.92	1.00

4.3.3 Network Modelling

In an autonomous microgrid, $\mathrm{Y_{bus}}$ is the network admittance matrix and is not constant because the system frequency is also not fixed. Therefore, for a system with *N* buses (virtual buses inclusive), $\mathrm{Y_{bus}}$ is defined as follows:

$$Y_{bus} = \begin{pmatrix} Y_{11}(w) & \cdots & Y_{1N}(w) \\ \vdots & \ddots & \vdots \\ Y_{N1}(w) & \cdots & Y_{NN}(w) \end{pmatrix} \tag{4.3}$$

4.3.4 Power injected at the virtual buses

It is desired in this section to establish the inherent relationship between active power, P_G at the virtual bus and load angle, δ and the reactive power, Q_G to internal generated voltage, E. This relationship can be utilized to achieve load sharing between VISMA inverters only with the help of local measurements at their point of common coupling.

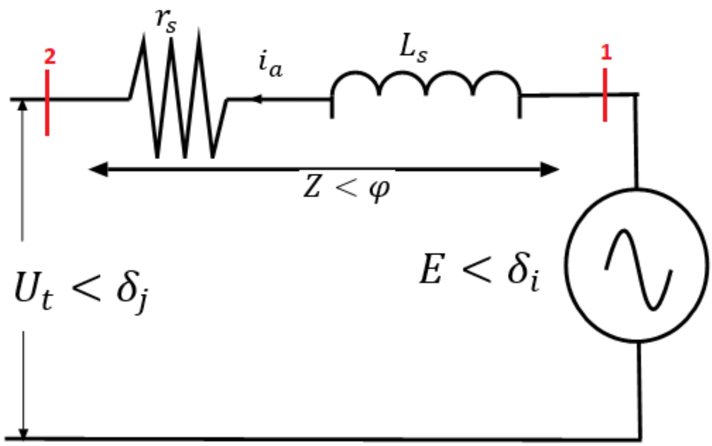

Figure 4.3. Per phase equivalent circuit of VISMA stator

The complex power delivered to the internal bus i of VISMA shown in fig. 4.3 is given as [156, 157]:

$$S_{G,i} = P_{G,i} + jQ_{G,i} = E_i i_i^* \qquad i = 1,2 \ldots\ldots n \tag{4.4}$$

Where n, is the number of internal nodes. $P_{G,i}$ and $Q_{G,i}$ are obtained as follows [60]:

$$P_{G,i} = \frac{E_i^2}{Z_{ij}} \cos \varphi_i - \frac{U_{t,i}.E_i}{Z_{ij}} \cos(\varphi_i + \delta_{ij}) \tag{4.5}$$

$$Q_{G,i} = \frac{E_i^2}{Z_{ij}} sin\, \varphi_i - \frac{U_{t,i}\,E_i}{Z_{ij}} \sin(\varphi_i + \delta_{ij}) \tag{4.6}$$

Where $\delta_{ij} = \delta_i - \delta_j$, is the power angle difference between the virtual bus and its corresponding terminal bus, i_i^* is the conjugate of the stator current from VISMA i, while Z_{ij} and φ_i are magnitude and the phase of the virtual stator impedance respectively. From phasor impedance diagram, we can establish that $\cos \varphi_i = R_{ij} / Z_{ij}$ and $\sin \varphi_i = X_{ij} / Z_{ij}$ [158], equations (4.5 & 4.6) are transformed to (4.7 & 4.8) as follows:

$$P_{G,i} = \frac{E_i}{R_{ij}^2 + X_{ij}^2} \left[R_{ij}(E_i - U_{t,i} \cos\delta_{ij}) - U_{t,i} \sin\delta_{ij}\right] \tag{4.7}$$

$$Q_{G,i} = \frac{E_i}{R_{ij}^2 + X_{ij}^2} \left[-R_{ij} U_{t,i} \sin\delta_{ij} + X_{ij}(E_i - U_{t,i} \cos\delta_{ij})\right] \tag{4.8}$$

Equations (4.7 & 4.8) are also reduced to (4.9 & 4.10) as follows;

$$U_{t,i} \sin\delta_{ij} = \frac{X_{ij}.P_{G,i} - R_{ij}.Q_{G,i}}{E_i} \tag{4.9}$$

$$E_i - U_{t,i} \cos\delta_{ij} = \frac{R_{ij} P_{G,i} + X_{ij}.Q_{G,i}}{E_i} \tag{4.10}$$

Independent control of P_G and Q_G is possible if we assume the virtual stator is purely inductive, so that $R_{ij} \approx 0$. If δ_{ij} is small, then we can assume that $\sin\delta_{ij} = \delta_{ij}$ and $\cos\delta_{ij} = 1$ so that, (4.9) and (4.10) becomes:

$$\begin{cases} P_{G,i} = \dfrac{U_{t,i}\ E_i}{x_{d,ij}}\ \delta_{ij} \\ Q_{G,i} = \dfrac{E_i^2}{x_{d,ij}} - \dfrac{U_{t,i}\,E_i}{x_{d,ij}} \end{cases} \tag{4.11}$$

Where $x_{d,ij}$, is the virtual reactance. It is clear from (4.11) that active power injected into VISMA bus is dependent on the power angle while reactive power is dependent on the voltage amplitude difference. Since the stator is purely inductive (as an assumption), it implies that there is no active power drop between the internal bus and the terminal of the VISMA but there exists reactive loss. $P_{G,ti}$ and $Q_{G,ti}$ injected at the terminal bus can be proved in similar way and in that case the complex power injected at the VISMA terminal bus 2 of fig. 4.3 becomes:

$$S_{G,ti} = P_{G,ti} + jQ_{G,ti} = U_{t,i}\, i_i^* \tag{4.12}$$

$$\begin{cases} P_{G,ti} = \dfrac{U_{t,i}\, E_i}{x_{d,ij}}\, \delta_{ij} \\ Q_{G,ti} = \dfrac{U_{t,i}\, E_i}{x_{d,ij}} - \dfrac{E_i^2}{x_{d,ij}} \end{cases} \tag{4.13}$$

From the solution of (4.11) and (4.13), the reactive loss in the virtual stator can be derived as [142, 158]:

$$Q_{loss,stator} = Q_{G,i} + Q_{G,ti} = \left(E_i^2 - 2U_{t,i}\, E_i \cos\delta_{ij} + U_{t,i}^2\right)/x_{d,ij} \tag{4.14}$$

Alternatively,

$Q_{loss,stator}$ can be evaluated by considering the voltage phasor relationship between the internal virtual bus and the corresponding terminal bus of a particular VISMA i, as shown in Fig. 4.4. The voltage drop in the virtual stator is thus obtained by applying cosine rule given in (4.15).

$$V_{drop,stator} = E_i^2 + U_{t,i}^2 - 2U_{t,i}\, E_i cos\delta_{ij} \tag{4.15}$$

So that,

$$Q_{loss,stator} = \frac{V_{drop,stator}^2}{x_{d,ij}} = \frac{E_i^2 - 2U_{t,i}\, E_i cos\delta_{ij} + U_{t,i}^2}{x_{d,ij}} \tag{4.16}$$

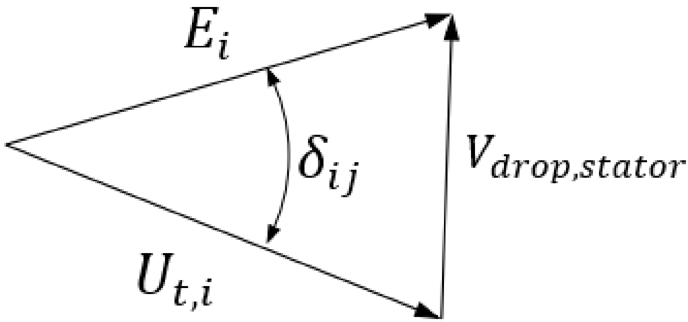

Figure 4.4. Virtual voltage drop estimation using cosine law

4.4 Problem formulation

Generally, DGs are modelled as PV or PQ buses in a grid connected system but it is impossible in IM to operate all DGs in PQ or PV mode because of the absence of slack bus. In an IM, DGs are modelled in three modes, i.e. PV, PQ, and droop [143, 149, 151, 159]. There is one exception, though, in that not every DG bus can be represented as a droop bus. VISMA can function without the addition of external droop since it possesses an innate natural droop feature. The formulation of the proposed algorithm involves two steps, first solving the load flow like the conventional Gauss- Siedel. The system frequency is initialized as 1.0 pu, and is recalculated in each step of the iteration. The voltage at all buses is also initialized to 1.0 pu. It is worth nothing that an arbitrary reference bus is selected with zero reference angle. The voltage U_i at bus i can be determined by using the following iterative voltage equation [160, 161].

$$\vec{U}_i^{k+1} = \frac{1}{\vec{Y}_{ii}}\left[\frac{P_i - jQ_i}{\left(\vec{U}_i^{k}\right)^*} - \sum_{j=1}^{i-1} \vec{Y}_{ij}\,\vec{U}_j^{k+1} - \sum_{j=i+1}^{N} \vec{Y}_{ij}\,\vec{U}_j^{k}\right] \tag{4.17}$$

For PV buses, net injected reactive power is evaluated based on the iterative voltages $\vec{U}_i^{k+1}$ and using the following expression:

$$Q_i^{k+1} = -Im\left\{\left(\vec{U}_i^{k}\right)^*\left(\sum_{j=1}^{i-1} \vec{Y}_{ij}\,\vec{U}_j^{k+1} + \sum_{j=i}^{N} \vec{Y}_{ij}\,\vec{U}_j^{k}\right)\right\} \tag{4.18}$$

Where $\vec{U}_i^{k+1}$ is the new value of iterated voltage at bus i, $\vec{U}_i^k$ *and* $\vec{U}_j^k$ are the magnitudes of voltages at buses i, and j respectively, $\vec{Y}_{ij}$ is the admittance between buses i, and j, P_i and Q_i are the scheduled active and reactive power at bus i and $\vec{Y}_{ii}$ is the self-admittance at bus i. For PV buses, Q is determined from (4.18) while the angle is determined from complex voltage in (4.17). For VISMA internal bus, bus voltage is pre-specified as an amplitude of the pole wheel voltage e_p, in this case the pole wheel angle is determined by keeping the iterative angle in (4.17) and discarding the iterative voltage. The VISMA internal buses are variable frequency dependent, so P and Q injections are obtained iteratively using the following expressions:

$$P_{Gi}^{k+1} = P_{max}^k \delta_{ij}^k \tag{4.19}$$

$$Q_{Gi}^{k+1} = \frac{E_i^2 - E_i U_j^k}{x_{d,i}} \tag{4.20}$$

Figure 4.5 depicts functional flow chart for the proposed algorithm. If there are m VISMAs in the network of system frequency, w then the total number of variable vectors X to be determined is given by:

$$X = [(P^N)^T \quad (Q^N)^T \quad (U^{N-m})^T \quad (\delta^{N-1})^T \quad w] \tag{4.21}$$

Network frequency is global and an important parameter that is required in each step of the iteration until program convergence is achieved. At steady state, there is no acceleration of the virtual rotor, so from (2.7) and the active expression in (4.11), the rotor angles are obtained as follows:

$$\delta_{ij}^{k+1} = \left(\frac{M_{mech,pu,i} w^k - D_i(w^k - w_{s,pu})}{P_{max,i}^k}\right) \tag{4.22}$$

The total active power generated at steady state is thus;

$$P_{total} = \sum_{i=1}^m P_{G,pu,i} = \left[M_{mech,pu,i}\, w_{pu} - K_{d,pu,i}\left(w_{r,pu} - w^*\right)\right] \tag{4.23}$$

For *N* bus systems, the total active (P_{loss}) and reactive (Q_{loss}) losses are calculated as follows [150, 162]:

$$\begin{cases} P_{loss} = \frac{1}{2}\sum_i^N \sum_j^N R\{\, Y_{ij}\big(U_i^* U_j + U_j^* U_i\big)\} \\ Q_{loss} = -\frac{1}{2}\sum_i^N \sum_j^N I\{\, Y_{ij}\big(U_i^* U_j + U_j^* U_i\big)\} \end{cases} \tag{4.24}$$

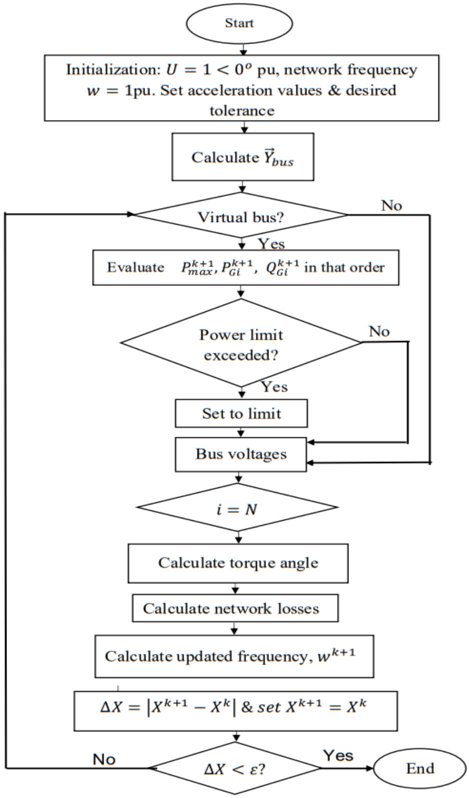

Figure 4.5. Functional flow chart for Virtual swing bus algorithm

The total active power (P_{total}) and reactive power (Q_{total}) injected by the VISMAs at the virtual buses are defined as follows [39, 150]

$$\begin{cases} P_{total} = P_{load} + P_{loss} \\ Q_{total} = Q_{load} + Q_{loss} \end{cases} \tag{4.25}$$

where P_{load} = Total active power load demand and Q_{load} = Total reactive power load demand

The classical model sometimes refers to the one in which damping is ignored (i.e., D_i = 0), but here the damping effect is considered explicitly, as it can have non-negligible effect on the stability of steady-state power grid operation and can potentially be used as tunable parameter for optimizing the stability and most valuably updating the system frequency [163]. In electrical power system, frequency is a global variable, and hence all VISMAs in the network are expected to inject active power at same angular frequency. By eliminating, P_{total} in (4.25) and (4.23), the following iterative expression can be derived.

$$w^{k+1} = w^* + \frac{\sum_{i=1}^{m} w^k M_{mech,pu,i} - \left(P_{load}^{k+1} + P_{loss}^{k+1}\right)}{\sum_{i=1}^{m} D_i} \tag{4.26}$$

4.4.1 Model extension with externally added droop controller

Equation (4.11) reveals that angle δ can be controlled by regulating P_G, and VISMA virtual bus voltage E is controlled by regulating Q_G. Control of the w dynamically controls the power angle and, thus, the active power flow. By adjusting P_G *and* Q_G independently, frequency and amplitude of the grid voltage are determined. Equation (4.13) forms the basis for the following conventional droop equation [27, 164]:

$$w - w_{s,pu} = -K_{pi}\left(P_{mi}^* - P_{mo,i}\right) \tag{4.27}$$

$$E_{ci} - E = -K_{qi}\left(Q_{Gi} - Q_{o,i}\right) \tag{4.28}$$

where P_{mo} and P_m^* $(or\ P_G)$ are the set and adjusted operating points of the virtual mechanical power input to the VISMA. E_c, $Q_{o,i}$, m_p *and* m_q are the controlled virtual bus voltage, reactive power set point, active and reactive droop coefficients, respectively.

Considering the steady operation of VISMA, (4.27) and (2.46) are combined to obtain the following iterative expression for rotor angle of the VISMAs:

$$\delta_{ij,droop}^{k+1} = \left[\frac{M_{mech,pu,i}w^k - \left(\frac{1}{K_{pi}} + D_i\right)(w^k - w_{s,pu})}{P_{max,i}^k}\right] \tag{4.29}$$

Frequency update and virtual excitation voltage with external droop addition in the form of iterative scheme are obtained as follows:

$$w_{droop}^{k+1} = w^* + \frac{\sum_{i=1}^{m} w^k M_{mech,pu,i} - \left(P_{load}^{k+1} + P_{loss}^{k+1}\right)}{\sum_{i=1}^{m}\left(\frac{1}{m_{pi}} + D_i\right)} \tag{4.30}$$

$$E_{ci}^{k+1} = E_i - m_{qi}\left(Q_{Gi}^k - Q_{o,i}\right) \tag{4.31}$$

If $m_{pi} = \infty$ in (4.29) and (4.30), then (4.22) and (4.26) are respectively obtained. Also, if $m_{qi} = 0$ in (4.31), then $E_{ci} = E$. These substitutions mean that the VISMA microgrid model without power and excitation control dynamics is easily obtainable from that with external droop extension. The load flow solution is completed when the difference between the new estimate and the previous estimates falls within an acceptable limit.

4.5 Validation of The Proposed Algorithm

To validate the applicability of the proposed algorithm and prove its accuracy, two case systems have been considered. These systems were also modelled in SIMULINK environment for detailed time domain analysis. In order to effectively analyse VISMA operations on these networks, additional virtual buses are introduced. These buses are equivalent to the internal nodes of the conventional ESM on the network. With respect to inverters, right amount of active power at the PCC necessary for frequency stability depends on the composition of loads on the network, and as such constant power load (CPL) and constant impedance load (CZL) have been considered for the analysis.

Case study 1. The first system is IEEE-9 bus standard network designed to operate as an island microgrid. For the purpose of the analysis, the buses are labelled as shown in Fig. 3.3., i.e. each bus number is shifted up by 3 when compared with the standard IEEE-9 bus system. The virtual buses of VISMA 1, VISMA 2 and VISMA 3 are numbered as 1, 2 and 3 respectively. The parameters for the VISMAs in Fig. 3.3 are given in Table 4.2 while the line and load bus parameters are obtainable from [42]. The validation here is in two categories. In the first category, the algorithm is used with constant excitation and constant torque. Table 4.3 shows the performance of the proposed algorithm with that of the time domain simulation, and the generic standard grid tied method obtained in Ref. [42] for a CPL at all load buses. Table 4.4 is the load flow results when all the load buses are of CZL. The average valued error of the voltage magnitude and phase angle of the proposed algorithm with respect to the time domain method are respectively 0.00083% and 0.005% for CPL and 0.0% and 0.00083% for CZL. These results demonstrate an excellent performance of the proposed load flow algorithm for islanded mode operation of microgrids based on virtual swing bus. The steady state frequency obtained by the proposed algorithm is shown in the respective table of results. Table 4.5 shows the values of active and reactive power generated by the VISMAs.

Table 4.2. VISMA parameters for IEEE-9 bus system

Description	Symbol	VISMA 1	VISMA 2	VISMA 3
Shunt capacitance,$\times 10^{-5}$, pu	C_f	3.1740	3.1740	3.1740
Virtual inductance,$\times 10^{-4}$, pu	L_s	1.6128	3.1778	4.8091
Virtual inertia (sec)	H	23.64	6.40	3.01
Virtual damping (p.u)	D	700	700	700
Amplitude of pole wheel voltage (p.u)	$\hat{e}_p$	1.0566	1.0502	1.0170
Virtual torque input, (p.u)	M_{mech}	0.716	1.630	0.850
Rated frequency	f_b		60 Hz	

Table 4.3. Voltage and angle profile of IEEE-9 bus VISMA microgrid with CPL and no external droop control

Bus No.	Bus Description	Original IEEE (Grid tied)		Virtual swing bus algorithm		Simulink	
		Voltage V (p.u)	Angle, δ (rad)	Voltage V (p.u)	Angle, δ (rad)	Voltage V (p.u)	Angle, δ (rad)
1	Virtual buses	-	-	1.0566	0.0396	1.0566	0.0397
2		-	-	1.0502	0.3443	1.0502	0.3444
3		-	-	1.0170	0.2298	1.0170	0.2299
4	Terminal buses	1.0400	0.0000	1.0400	0.0000	1.0400	0.0000
5		1.0250	0.1620	1.0251	0.1620	1.0251	0.1620
6		1.0250	0.0814	1.0250	0.0814	1.0250	0.0814
7	Load buses	1.0260	-0.0387	1.0258	-0.0387	1.0258	-0.0387
8		0.9956	-0.0696	0.9957	-0.0696	0.9956	-0.0696
9		1.0127	-0.0644	1.0127	-0.0644	1.0127	-0.0643
10		1.0258	0.0649	1.0258	0.0649	1.0258	0.0650
11		1.0159	0.0127	1.0159	0.0127	1.0159	0.0127
12		1.0324	0.0343	1.0324	0.0343	1.0324	0.0344
Frequency				0.999999584			

Table 4.4. Voltage and angle profile of IEEE-9 bus VISMA microgrid With CZL and no external droop control

Bus No.	Bus Description	Virtual swing bus algorithm		SIMULINK	
		Voltage, V (p.u)	Angle, δ (rad)	Voltage, V (p.u)	Angle, δ (rad)
1	Virtual buses	1.0566	0.0403	1.0566	0.0403
2		1.0502	0.3459	1.0502	0.3459
3		1.0170	0.2315	1.0170	0.2315
4	Terminal buses	1.0395	0.0000	1.0395	0.0000
5		1.0239	0.1620	1.0239	0.1620
6		1.0235	0.0808	1.0235	0.0808

7	Load buses	1.0248	-0.0394	1.0248	-0.0393
8		0.9949	-0.0698	0.9949	-0.0698
9		1.0107	-0.0665	1.0107	-0.0665
10		1.0242	0.0640	1.0242	0.0640
11		1.0136	0.0104	1.0136	0.0104
12		1.0306	0.0330	1.0306	0.0330
Frequency		0.999983475			

Table 4.5. Power generated by the VISMA in IEEE-9 bus VISMA microgrid for constant excitation and constant torque

Load Type	Power injected at virtual buses	Sources		
		VISMA 1	VISMA 2	VISMA 3
CZL	Active power, P	0.7276	1.6415	0.8616
	Reactive power, Q	0.3124	0.3821	0.0283
CPL	Active power, P	0.7161	1.6301	0.8501
	Reactive power, Q	0.3030	0.3693	0.0181

In the second category, the algorithm is used with an added external droop control. Equal values of static droop coefficients have been used for all VISMAs i.e $m_p = 0.03$ and $m_q = 0.02$. Table 4.6 and Table 4.7 respectively illustrate the performance of the algorithm for CPL and CZL in comparison with the time domain values. The average valued error of the voltage magnitude and phase angle of the proposed algorithm with respect to the time domain method are respectively 0.0033% and 0.00083% for CPL and 0.0% and 0.0025% for CZL. These results reveal a good performance of the proposed algorithm for an islanded microgrid. The active and reactive power generated by VISMAs are presented in Table 4.8. The total

Table 4.6. Voltage and angle for IEEE-9 bus VISMA microgrid with CPL and external droop

Bus No.	Bus Description	Virtual swing bus algorithm		SIMULINK	
		Voltage, V (p.u)	Angle, δ (rad)	Voltage, V (p.u)	Angle, δ (rad)
1	Virtual buses	1.0504	0.0401	1.0504	0.0401
2		1.0427	0.3497	1.0428	0.3497
3		1.0162	0.2315	1.0162	0.2315
4	Terminal buses	1.0333	0.0000	1.0333	0.0000
5		1.0173	0.1645	1.0174	0.1644
6		1.0204	0.0822	1.0204	0.0822
7	Load buses	1.0186	-0.0392	1.0186	-0.0392
8		0.9878	-0.0706	0.9879	-0.0706
9		1.0056	-0.0652	1.0056	-0.0652
10		1.0181	0.0660	1.0182	0.0660
11		1.0088	0.0129	1.0088	0.0129
12		1.0265	0.0346	1.0265	0.0346
Frequency		0.999999802			

Table 4.7. Voltage and angle for IEEE-9 bus VISMA microgrid with CZL and external droop

Bus No.	Bus Description	Virtual swing bus algorithm		SIMULINK	
		Voltage, V (p.u)	Angle, δ (rad)	Voltage, V (p.u)	Angle, δ (rad)
1	Virtual buses	1.0505	0.0401	1.0505	0.0402
2		1.0428	0.3486	1.0428	0.3483
3		1.0162	0.2299	1.0162	0.2299
4	Terminal buses	1.0337	0.0000	1.0337	0.0000
5		1.0175	0.1634	1.0175	0.1632
6		1.0203	0.0806	1.0203	0.0805
7	Load buses	1.0193	-0.0392	1.0194	-0.0392
8		0.9894	-0.0694	0.9894	-0.0695
9		1.0057	-0.0663	1.0057	-0.0664
10		1.0184	0.0649	1.0185	0.0648
11		1.0085	0.0109	1.0086	0.0108
12		1.0264	0.0330	1.0264	0.0329
Frequency		0.999999438			

Table 4.8. Power generated by the VISMAs in IEEE-9 bus VISMA microgrid with droop control extension.

Load Type	Power injected	Sources		
		VISMA 1	VISMA 2	VISMA 3
CPL	P, pu	0.7164	1.6304	0.8504
	Q, pu	0.3101	0.3727	0.0402
CZL	P, pu	0.7165	1.6305	0.8505
	Q, pu	0.3050	0.3716	0.0408

power generated by the VISMAs and the total load demand and losses of the system for both categories of case study 1 are shown in Table 4.9. According to Table 4.9, when the frequency deviation is same among units, that VISMA with a high capacity can produce more power to microgrid [152]. Tables 4.8 and 4.9 highlight the importance of relationships between frequency deviation and active power sharing among VISMAs.

Table 4.9. Total terminal power generated, demands and losses for IEEE-9 bus VISMA microgrid

Control mode	Load type	P_{dg}	Q_{dg}	P_{load}	Q_{load}	P_{loss}	Q_{loss}	Total losses
No external droop	CPL	3.1963	0.6904	3.1500	1.1500	0.0464	0.4596	0.4619
	CZL	3.2307	1.5989	3.1839	1.1609	0.0467	0.4380	0.4405
External droop added	CPL	3.1971	1.5768	3.1500	1.1500	0.0471	0.4268	0.4294
	CZL	3.1975	1.5804	3.1511	1.1489	0.0464	0.4315	0.4340

Figure 4.6 demonstrates show that, frequency stability of the system improves when local droop control is added external to each VISMA. Figure 4.7 illustrates the voltage profile for both categories of system case study. CPL_droop and CZL_droop respectively define constant power load and constant impedance load when external droop control is added to natural VISMA.

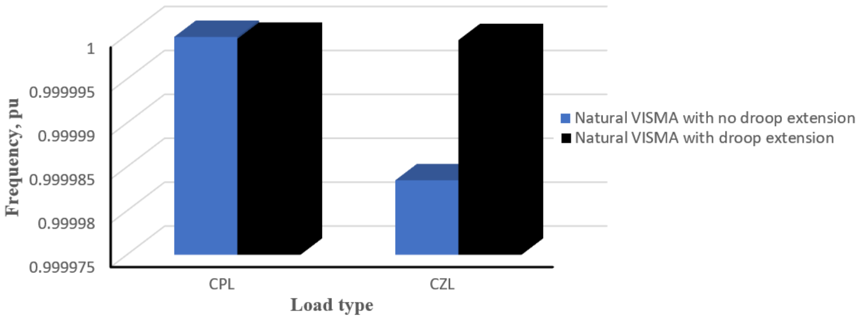

Figure 4.6. System frequency for IEEE-9 bus VISMA microgrid for different load type

Figure 4.7 is the schematic voltage profile representation at the VISMA for different load type and control. The plot show that voltages at the system buses are negatively impacted (based on the chosen static droops) when external droop control is added. The level of impact may however be reduced by using lower size of droop coefficients [165].

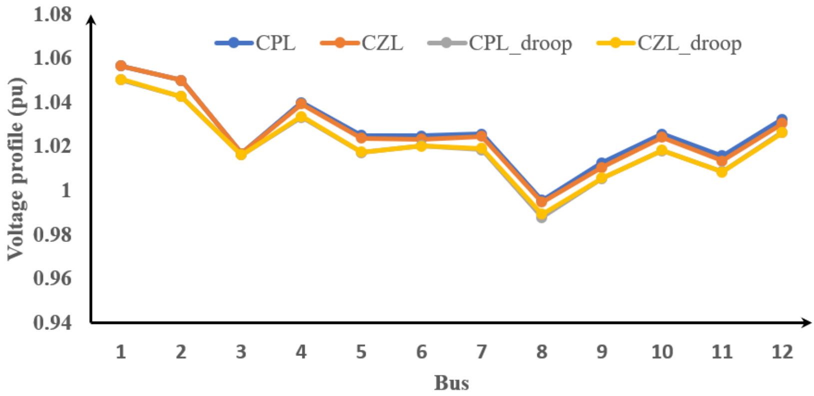

Figure 4.7. Voltage profile for different load type and control

Fig. 4.8 – Fig. 4.11 are nonlinear dynamic simulations of IEEE-9 bus VISMA microgrid for constant power load case. The idea here is to schematically validate some of the steady state numerical values obtained in the tables. Fig. 4.8 demonstrates the synchronization of the three VISMAs on the grid at a unified system frequency of approximately 1. Numerical results shown in Table 4.5 for active and reactive power at the virtual buses 1-3 under constant power load with no external PLC added are illustrated in Fig. 4.9 and Fig. 4.10. Though, the bone of contention is the steady state. operating point, but the transient behaviour of the VISMAs are also shown. Rotor angle simulation of IEEE-9 bus VISMA microgrid with CPL having no external droop control for buses 1-3 shown in Table 4.3 are demonstrated in Fig. 4.11

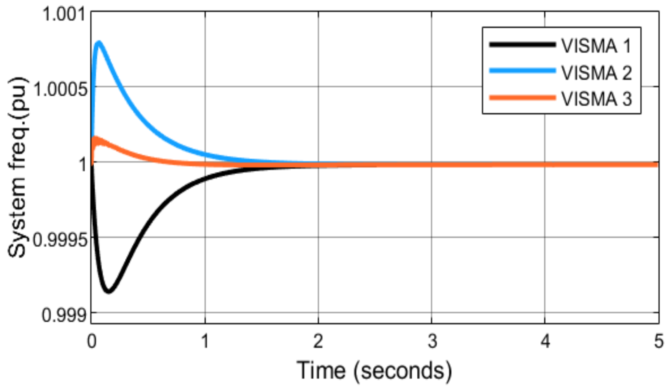

Figure 4.8. System frequency

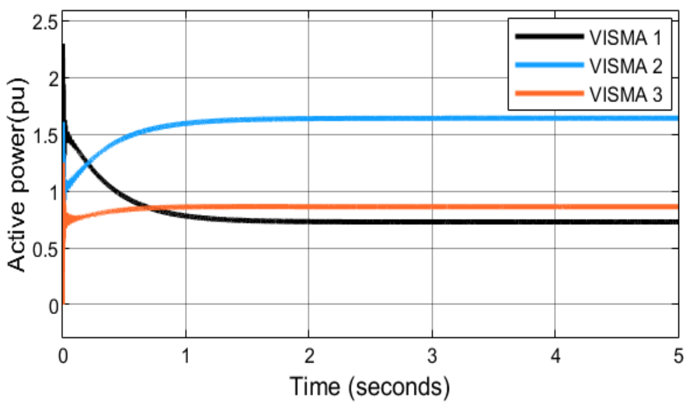

Figure 4.9. Active power at the virtual buses

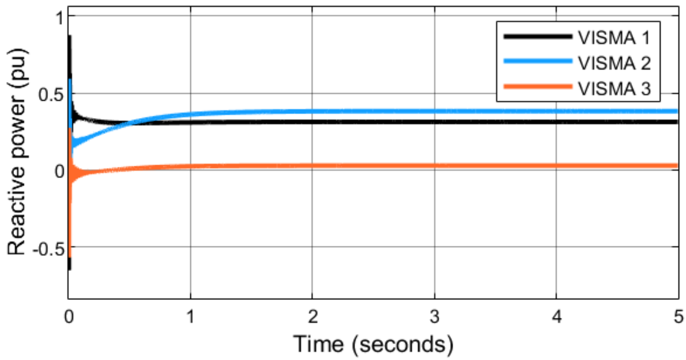

Figure 4.10, Reactive power injection at the virtual buses

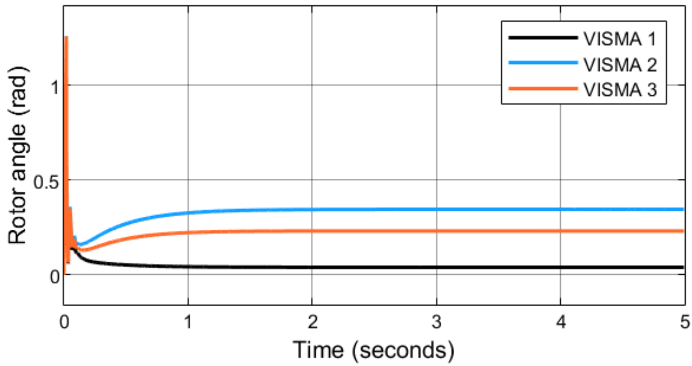

Figure 4.11. Rotor angle stationary operating points

Case study 2. The second system is a low voltage (LV) distribution system (Fig. 4.12). The base power and base line voltage are respectively 1000W and $220 - V_{LL}$. The parameters for the VISMAs and the lines are as given in Table 4.9. Proportionate equal static droop coefficients used are given in Table 4.9. To simplify the analysis, only CZL type was considered at the load bus. Table 4.11 gives the voltage and angle profile in each bus.

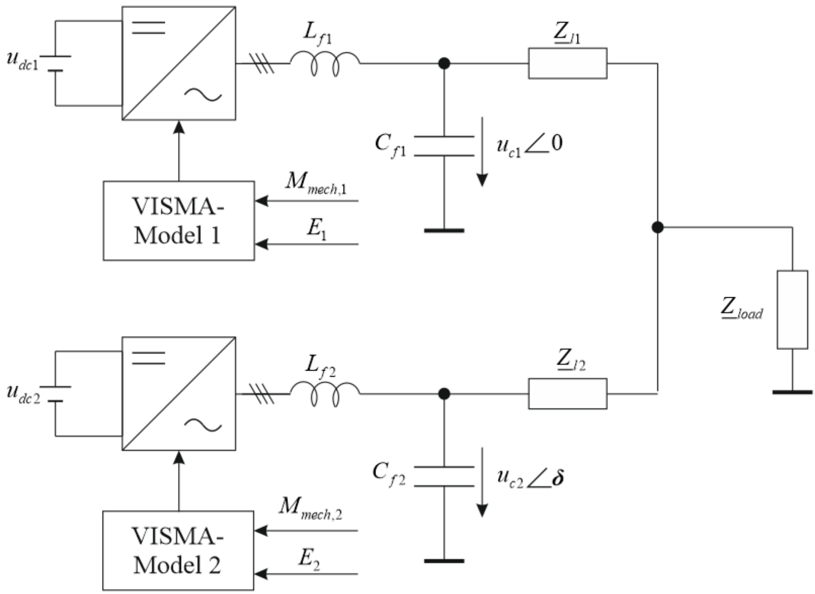

Figure 4.12. Two VISMA low voltage model [48]

Values of the generated power as well as the power demands and losses of system are presented in Table 4.12 for the algorithm with and without external droop control. The steady state frequency obtained by the proposed algorithm without control is 0.9999 p.u and with control is 0.999953 p.u which also consolidate on the capability of external droop to enhancing system frequency stability. The average valued error of the voltage magnitude and phase angle of the proposed algorithm with respect to the time domain method are given in Table 4.13 and also schematically represented in Fig. 4.13. According to Table 4.13, the average valued error in IEEE-9 bus system is quite less compared to those obtained in LV system. This is simply because IEEE-9 bus system is highly inductive as compared to LV system with low X/R ratio. When X/R is high, both the active power and reactive power are efficiently decoupled.

Table 4.10. Parameters for the two-system low voltage model [48]

Symbol	Value	Symbol	Value	Description
L_{f1}	5 mH	L_{f2}	5 mH	real
C_{f1}	5 μF	C_{f2}	5 μF	real
L_{s1}	3.5 mH	L_{s2}	2.5mH	virtual
J_1	$0.1\ \mathrm{kg}\cdot\mathrm{m}^2$	J_2	$0.6\ \mathrm{kg}\cdot\mathrm{m}^2$	virtual
D_1	$5\ \mathrm{kg}\cdot\mathrm{m}^2/\mathrm{s}$	D_2	$5\ \mathrm{kg}\cdot\mathrm{m}^2/\mathrm{s}$	virtual
$\underline{Z}_{l1}$	(0.3 + 0.5j) Ω	$\underline{Z}_{l2}$	(0.2 + 0.3j) Ω	real
f_0	60 Hz	$\underline{Z}_{Load}$	(10 + 5.5j) Ω	real
$\hat{e}_{p1,L-L}$	220 V	$\hat{e}_{p2,L-L}$	220 V	virtual
M_{mech1}	6.6 Nm	M_{mech2}	2.34 Nm	virtual
m_{p1}	9.4×10-5rad/s/W	m_{p2}	9.4×10-5rad/s/W	real
m_{q1}	0.0013V/VAR	m_{q2}	0.0013V /VAR	real

** All parameters are converted to p.u for analysis

Table 4.11. Voltage profile 2-VISMA LV system

Bus No	Bus Description	No external droop				External droop			
		Virtual swing bus Algorithm		Simulink		Virtual swing bus Algorithm		Simulink	
		V, pu	δ, rad	V, pu	δ, rad	V, pu	δ, rad	V, pu	δ, rad
1	Internal buses	1.0000	0.0706	1.0000	0.0704	0.9946	0.0708	0.9947	0.0706
2		1.0000	-0.0049	1.0000	-0.0054	0.9909	-0.0047	0.9909	0.0052
3	Load buses	0.9833	0.0000	0.9831	0.0000	0.9765	0.0000	0.9764	0.0000
4		0.9740	-0.0238	0.9738	-0.0239	0.9661	-0.0233	0.9660	-0.0234
5		0.9612	-0.0239	0.9610	-0.0239	0.9539	-0.0237	0.9537	-0.0236

Table 4.12. Power generated, load demand and system losses

Control type	Sources	P	Q	P_{dg}	Q_{dg}	P_{load}	Q_{load}	P_{loss}	Q_{loss}
VISMA only	VISMA 1	2.5476	0.7025	3.4893	2.0477	3.4332	1.8883	0.0561	0.1595
	VISMA 2	0.9417	1.3452						
VISMA + external droop	VISMA 1	2.5211	0.7505	3.4363	2.0167	3.3810	1.8596	0.0553	0.1572
	VISMA 2	0.9152	1.2661						

Table 4.13. Average valued error of the proposed algorithm with respect to time domain values

System case	Control configuration	Load types	V, pu	δ, rad
IEEE-9 bus	Without PLC	CPL	0.00083%	0.00500%
		CZL	0.00000%	0.00083%
	With PLC	CPL	0.00330%	0.00083%
		CZL	0.00250%	0.01000%
LV system	Without PLC	CZL	0.01200%	0.01600%
	With PLC	CZL	0.01000%	0.01800%

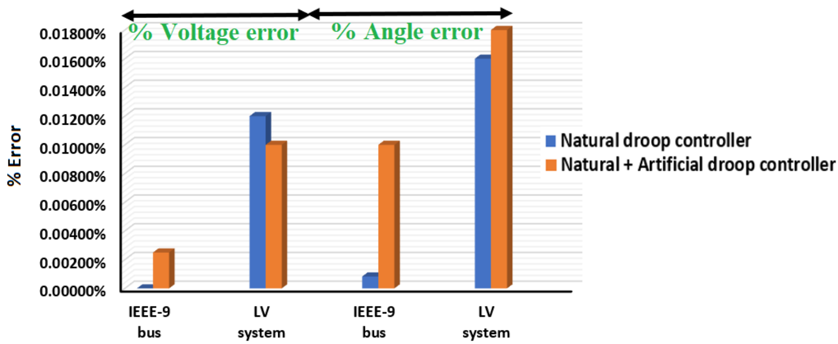

Figure 4.13. Comparative percentage error between LV & HV systems

5. Small-Signal Rotor Angle Stability of *n*-VISMA Microgrid

5.1 Introduction

Due to the progressive integration of DGs in the power system, the deployment of novel technologies and controls has led to several questions being asked regarding the system responses to perturbations. The variability and uncertainty in DGs operations have brought a number of technical challenges to power system operations and impose enormous effects on power system stability and dynamic responses of the microgrid [13, 26]. Electrical power systems are generally known to be ever prone to rotor angle oscillations which may occur as a result of generation dispatch changes, load variations, weak electrical connections between the inverter-based power sources, between power source inverter and load due to long distances (large reactance), and due to uncoordinated control units. Because of the complex nature of the power systems the disturbances in a region may affect other power sources within the same local region or other external areas. Since the inverter-based sources are not as rugged as the ESM, the system oscillations must be killed in due time before causing unrepairable damage to the power systems. In a multi-VISMA (n-VISMA) microgrid, relative rotor angle stability of the power system is dependent on the active power balance after a small perturbation. Using relevant analytical models are essential issues for microgrid stability analysis. This section provides a comprehensive small-signal stability analysis to study the inherent electromechanical oscillations in the virtual rotors of an interconnected VISMA system. The subsystems of the microgrid consisting of VISMA, network, load and the outer power control are all modelled in Synchronously-rotating Reference Frame (SRF).

5.2 State of the art of small-signal models in microgrids

A microgrid can be operated either in grid connected mode or in isolated mode. When in grid (stiff) connected mode, most of the system-level dynamics are dictated by the main grid due to the relatively small size of micro sources. In isolated mode, the system dynamics are dictated by micro sources themselves, their power regulation control and, to an unusual degree, by the network itself. One of the important concerns in the reliable operation of a microgrid is small-signal stability [146, 166, 167].

Power system stability plays a vital role in ensuring safe, reliable and optimal operation of a high order multivariable modern power system whose dynamic response is induced by several devices with distinctive properties. Depending on the network configuration, circumstances surrounding the system operation and the nature of disturbances, varieties of instabilities may evolve. Power system stability is basically categorized into rotor angle stability, frequency stability and voltage stability [19]. In a n-VISMA microgrid, the ability to reestablish balance between the opposing forces is determined by the rotor angle stability of each VISMA. Rotor angle stability is the ability of the VISMA to remain in synchronism with the network after being subjected to disturbance caused by torque imbalances in the system. If the rotor oscillations resulting from the imbalances are not resolved in due time, they can lead to severe damages to the power plant [27]. As one of the critical stability problems for secured microgrid systems, angle stability can be categorized into a small-disturbance and large disturbance angle stability [23, 24]. In the stability analysis of multimachine power system with high level of distributed energy, different computational tools have been developed to study the interactions between different units in the microgrid system.

Extensive studies have been conducted on the stability of VSGs in a single inverter-based power grid that is controlled by either the GFL or GFM converters. Frequency stability analysis of a grid connected inverter is proposed in [168]. The authors divided the synchronization procedures into grid-synchronization and self-synchronization to assess the low-frequency nonlinear characteristic and instability scenario. This model has the limitation of heavily depending on slack bus and thus may be difficult to implement for a multimachine microgrid. In Refs. [169, 170], the dynamic characteristic of a single power converter connected to a stiff grid was studied by developing a small-signal model of a conventional droop control, root trajectory technique was then used to investigate stability condition of the system. However, the control strategy used lacks capability to provide necessary ancillary services during system disturbances because of incapability to solve inertia issues and thus limit the rate of change of frequency (ROCOF). In Ref. [66], VSG is used to enhance the rotor angle stability of a small grid system and results reveal that the presence of VSG improves the damping, but the magnitude of the rotor angle excursion due to perturbation is unchanged. In [171], a demand response method has been proposed to improve small-signal stability of a power system through adjustment of operating points using modal analysis for grid operations. The procedural techniques are well highlighted but detailed analytical methods are not examined. A tuning method of the cascaded virtual synchronous machine (CVSM) using the eigenvalue sensitivity matrix of the linearized model is presented in [34]. A linearized state space model of CVSM for a single machine operating in islanded mode is presented in [35] to evaluate small disturbance stability by eigenvalue analysis. The analytical model for D'Arco et. al. on CVSM model is cumbersome for a single machine and may not be easily realizable for multimachine analysis. Jia Lu et al. carried out small signal stability analysis on OSAKA model of VSG control by comparing its dynamic characteristics with that of droop control [31]. A small-signal stability analysis of a PV generation connected to a weak grid is investigated in [172] using eigenvalue technique under different power grid strength and control parameters. Stability analysis of a synchronverter-dominated microgrid based on bifurcation theory is presented in [173]. Small signal stability analysis and different control strategy for active support control of interface converter is presented in [174]. A small signal stability analysis based on n Light Gradient Boosting Machine (LightGBM) optimization model to predict the minimum damping ratio required by the grid dynamic stability is presented in [175].

In the practical sense, the number of DGs on the grid are enormous and it is thus imperative to consider stability analysis of multi DGs systems. Qiang et. al. suggested a NL approach to attenuating disturbance in the excitation control of multi machine power system based on recursive technique without the need to carry out linearization [176]. Karady and Mansour proposed two algorithms for stability improvement of the power system. The first algorithm employs tracking of the relative rotor angles to determine which generator in the network is to be tripped when disturbance occurs while the second algorithm compares the active power output of each generator before and after disturbance to determine the most appropriate generator tripping for transient stability [177]. [178] carried out small signal stability analysis on a part of Western Electricity Coordinating Council system (WECC) to investigate the impact of reduced inertia on electromechanical modes of oscillation of different level of multi-DGs on the system dynamic stability. It was reported that when the penetration level is more than 30%, the damping ratio of the critical mode is largely impacted below the threshold limit. System level small signal analysis is carried out and as such the individualized impact of each of the DG parameters on the system dynamics have not been considered. In Ref. [179], modelling and stability analysis method of VSG controlled Modular Multilevel Converters (MMC) using the concept of linearized small signal average valued model was proposed. According to Xu *et al.* [180], this model implementation is only effective if the capacitors are sufficiently large to uphold relatively constant voltage across each MMC submodule. In addition, MMC averaged models are not able to reliably simulate the transients under dc fault conditions. In Refs. [32, 33], the stability performance between islanded microgrid with single VISMA of large capacity and that with multiple VISMAs with smaller sizes was investigated. It was reported that the multi-VISMA microgrid suppresses frequency oscillation better than the single VISMA counterpart. However, the small signal model employed for the microgrid stability analysis is oversimplified and hides a lot of details, it may not be easily extended for oscillatory modal analysis which is the most modern method currently used to analyse power system stability [138]. A small-signal model of a multi-energy system integrated with wind and photovoltaic (PV) is presented in [136]. The damping characteristics of the interconnected power system are analysed using eigenvalue technique under different operating conditions. The authors indicated that systems with RE system show the best recovery ability and small-signal response and are thus able to adjust system frequency faster. The stability analysis by these authors are also at system level and has not taken system dynamics and control parameters into consideration. In the autonomous operation of microgrid, the control architecture adopted is essential for smooth operation of the system. Centralized control schemes such as master slave [181] are based on the availability of a communication infrastructure which is said to be expensive and unreliable as there are extensively large numbers of micro sources to be controlled in the network. A decentralized control scheme solves this problem by adopting local droop control for each micro-source. Droop control is widely used in inverter-based autonomous microgrids to regulate the power flow according to the local information with no need of communication.

Since 2017, different topologies of VSG control have been proposed [29] and many are still continuously evolving. Due to this different control strategies, small signal stability analysis techniques also differ. In addition, most of the stability analysis on the VSG control models has mostly been considered on a single machine or a mixed power plant, as in [30, 31]. However, in regards to the VISMA model from IEE Germany, very little work has been done on its stability analysis; the most recent work by [32, 33] is carried out at system level. In this dissertation, a small-signal rotor angle stability analysis of a multi-virtual synchronous machine operating in autonomous mode is presented. The approach here is to obtain a novel linearized state space model for *n*-VISMA microgrid and then evaluate eigenvalue sensitivity with respect to virtual inertia and virtual damping. The sensitivities of the eigenvalues are used to identify the parameters with the strongest influence on the critical modes. The sensitivities of the eigenvalues indicate the magnitude and direction of the eigenvalue shift when such parameter is changed. The concept of participation factor (PF) is also employed to identify which of the VISMA is stabilizing the network the most and which is contributing to the microgrid oscillations based on the specified network parameters. Transients and steady state dynamics of the microgrid are also studied. The operational limits of the investigated microgrid are also studied. In the stability analysis of the investigated microgrid, the power sources are assumed to be 100% VISMAs in anticipation of future power systems with no traditional generation systems. However, the stability analysis is carried out on a VISMA microgrid with two configurations i.e. VISMAs with total reliance on the inherent droop characteristics of ESM (discussed in this chapter) and VISMA with an externally added decentralized power loop controller (discussed in chapter 6)

5.3 *n*-VISMA system representation

VISMAs interact with one another through the transmission network and the connected loads as shown in Fig. 5.1. In Fig. 5.1, let $i = 1,2, \ldots n$ corresponds to the internal buses of the VISMAs, $i = n+1, n+2, \ldots \ldots 2n$ corresponds to the terminal buses of the VISMAs and $i = 2n + 1, \ldots \ldots \ldots . m$ be the load buses. All loads are modelled as constant impedances [54].

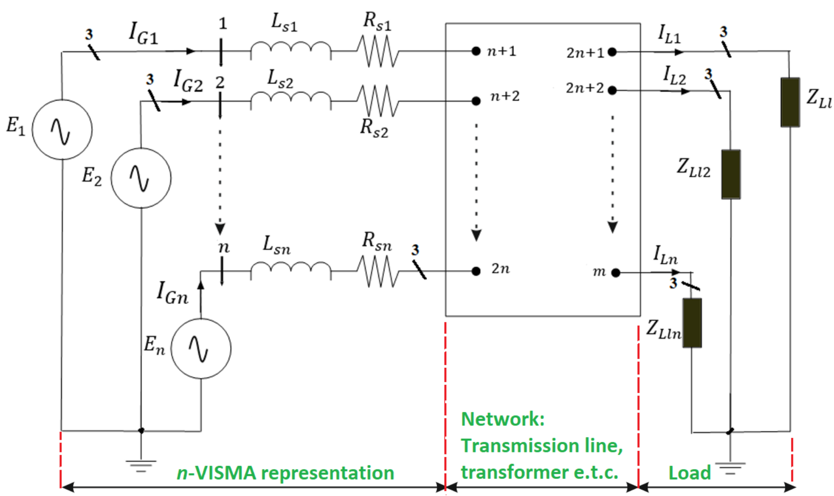

Figure 5.1. *n*-VISMA with constant impedance loads

5.4 State space modelling of *n*-VISMA microgrid

5.4.1 Modelling of the network

The VISMAs described by (2.46) - (2.47) interact with one another through the electrical network (transmission network and the distribution of loads), which determines the electrical output power of each machine. In a small-signal model, the dynamics of the line inductances and capacitances, referred to as the electrical transients, are presumed to have a rapid decay and are ignored [57, 166]. Thus, the electric output power P_{ei} provided by the VISMAs can be determined from an algebraic voltage-current relationship involving the network admittance matrix $\boldsymbol{Y_{bus}}$ as [57]:

$$\vec{\boldsymbol{I}} = \boldsymbol{Y_{bus}}\vec{\boldsymbol{U}} \tag{5.2}$$

$\vec{U}$ is the vector of bus voltage, $\vec{\boldsymbol{I}}$ is the current injections at the buses, and the positive direction of $\vec{\boldsymbol{I}}$ means the current is flowing from a bus into the network and $\boldsymbol{Y_{bus}}$ is the bus admittance matrix. Equation (5.2) is broken down for generation and load buses as follows

$$\begin{bmatrix} \vec{I}_G \\ \vec{I}_L \end{bmatrix} = \begin{bmatrix} Y_{gg} & Y_{gl} \\ Y_{lg} & Y_{ld} \end{bmatrix} \begin{bmatrix} \vec{U}_G \\ \vec{U}_L \end{bmatrix} = \begin{bmatrix} Y_{gg} & Y_{gl} \\ {Y_{gl}}^T & Y_{ld} \end{bmatrix} \begin{bmatrix} \vec{U}_G \\ \vec{U}_L \end{bmatrix} \tag{5.3}$$

$\vec{I}_G$ *and* $\vec{U}_G$ are vectors of current and voltage injection at the VISMA terminal bus. $\vec{I}_L$ *and* $\vec{U}_L$ are vectors of current and voltage injection at the load buses and are defined as follows:

$$\vec{U}_G = \begin{bmatrix} U_{g1} \\ U_{g2} \\ \vdots \\ U_{g,n} \end{bmatrix} = n\ vector\ of\ VISMA\ terminal\ bus\ voltage\ (n \times 1) \tag{5.4}$$

$$\vec{U}_L = \begin{bmatrix} U_{L,1} \\ U_{L,2} \\ \vdots \\ U_{L,N_L} \end{bmatrix} = n\ vector\ of\ load\ bus\ voltage\ \ (n_L \times 1) \tag{5.5}$$

$$\vec{I}_G = \begin{bmatrix} I_{g1} \\ I_{g2} \\ \vdots \\ I_{gn} \end{bmatrix} = n\ vector\ of\ VISMA\ output\ current\ (n \times 1) \tag{5.6}$$

$$\vec{I}_L = \begin{bmatrix} I_{L,1} \\ I_{L,2} \\ \vdots \\ I_{L,N_L} \end{bmatrix} = n_L \; vector \; of \; load \; bus \; current \; (n_L \times 1) \tag{5.7}$$

$N = n + n_L =$ Total number of terminal nodes [163]

The admittance matrix in (5.3) then has the following dimensions:

$$Y_{gg} = n \times n$$

$$Y_{gl} = n \times n_L$$

$$Y_{lg} = n_L \times n$$

$$Y_{ld} = n_L \times n_L$$

5.4.2 Modelling of the load

The stability analysis is simplified if the entire power system is reduced to only coupling between the VISMAs in the network and this is possible if all loads are modelled as constant impedances. With this type of load, all the buses other than the VISMA internal buses can be eliminated by network reduction [182]. Consider the constant load connected to bus k in fig 5.2. In order to determine the load admittance Y_{Lk} at a particular bus k, the power consumption $P_{Lk} + JQ_{Lk}$ (positive values meaning consuming) and the magnitude of voltage at that bus are necessary. Because of the orientation of I_{Lk} and U_{Lk}, negative is usually placed in front of the load admittance

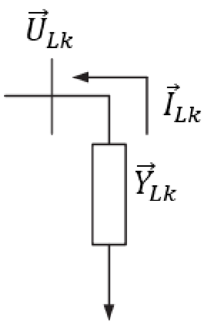

matrix Y_{Lk} [142]. Each load is converted into a constant admittance to ground at its bus using the equation (5.7)

Figure 5.2. Constant impedance load

$$S_{Lk} = U_{Lk} I_{Lk}^{*} = P_{Lk} + JQ_{Lk} \tag{5.7}$$

Where P_{Lk}, Q_{Lk}, U_{Lk} *and* Y_{Lk} are the active power, reactive power, voltage, and load admittance at bus *k* respectively. Because of the orientation of I_{Lk} *and* U_{Lk}, negative is usually placed in front of load admittance matrix Y_{Lk} [142].

The current injection I_{Lk} at bus k is thus given by;

$I_{Lk}^{*} = -\frac{P_{Lk}+JQ_{Lk}}{U_{Lk}}$ or

$$I_{Lk} = -\left(\frac{P_{Lk}+JQ_{Lk}}{U_{Lk}}\right)^{*} = -\frac{P_{Lk}-JQ_{Lk}}{U_{Lk}^{*}} \times \frac{U_{Lk}}{U_{Lk}} = -\left(\frac{P_{Lk}}{|U_{Lk}|^{2}} - J\frac{Q_{Lk}}{|U_{Lk}|^{2}}\right) U_{Lk} \tag{5.8}$$

Similarly,

$$I_{Lk} = -Y_{Lk} U_{Lk} = -(G_{Lk} + JB_{Lk}) U_{Lk} \tag{5.9}$$

In matrix notations, the load components in the network can be expressed as

$$\vec{\boldsymbol{I}}_{L} = -\begin{bmatrix} Y_{L1} & 0 & 0 & 0 \\ 0 & Y_{L2} & 0 & 0 \\ 0 & 0 & Y_{L3} & 0 \\ 0 & 0 & 0 & \ddots \end{bmatrix} \boldsymbol{U}_{L} \tag{5.10}$$

From (5.8) and (5.9), it can be deduced that $G_{Lk} = \frac{P_{Lk}}{|U_{Lk}|^{2}}$ and $B_{Lk} = -\frac{Q_{Lk}}{|U_{Lk}|^{2}}$

In order to combine load and network model, we substitute (5.9) in (5.3) so that;

$$\begin{bmatrix} \vec{I}_{Gk} \\ -Y_{Lk} U_{Lk} \end{bmatrix} = \begin{bmatrix} Y_{gg} & Y_{gl} \\ Y_{lg} & Y_{Ld} \end{bmatrix} \begin{bmatrix} \vec{U}_{Gk} \\ \vec{U}_{Lk} \end{bmatrix} \quad \text{or} \tag{5.11}$$

$$\begin{bmatrix} \vec{I}_{Gk} \\ 0 \end{bmatrix} = \begin{bmatrix} Y_{gg} & Y_{gl} \\ Y_{lg} & Y_{ld} + Y_{Lk} \end{bmatrix} \begin{bmatrix} \vec{U}_{Gk} \\ \vec{U}_{Lk} \end{bmatrix} \tag{5.12}$$

If there exists a local constant impedance load on the generator terminal bus, then (5.12) is modified as follows:

$$\begin{bmatrix} \vec{I}_{Gk} \\ 0 \end{bmatrix} = \begin{bmatrix} \tilde{Y}_{gg} & Y_{gl} \\ Y_{lg} & \tilde{Y}_{ll} \end{bmatrix} \begin{bmatrix} \vec{U}_{Gk} \\ \vec{U}_{Lk} \end{bmatrix} = \boldsymbol{Y'_{bus}} \begin{bmatrix} \vec{U}_{Gk} \\ \vec{U}_{Lk} \end{bmatrix} \tag{5.13}$$

Where $\tilde{Y}_{gg} = Y_{gg} + Y_{Lk}$ and $\tilde{Y}_{ll} = Y_{ld} + Y_{Lk}$

Equation (5.13) reveals that CZL at a particular bus *k* only exist as an addition in the main diagonal of $\boldsymbol{Y_{bus}}$ when the current injection at the load buses is set to zero. If we define n and n_L as the number of VISMA terminal nodes and load nodes respectively, then the dimension of $\boldsymbol{Y_{bus}}$ is $(n + n_L) \times (n + n_L)$ while that of partitioned admittance matrix $\boldsymbol{Y'_{bus}}$ is $(2n + n_L) \times (2n + n_L)$ [183]. By applying Kron's reduction technique [184], a model reduced to the VISMA terminal bus is obtained as follows:

$$\vec{I}_{Gk} = \left[\tilde{Y}_{gg} - Y_{gl}\left(\tilde{Y}_{ll}\right)^{-1} Y_{lg}\right] \vec{U}_{Gk} = Y_{reduce}\, \vec{U}_{Gk} \tag{5.14}$$

$\boldsymbol{Y}_{\text{reduce}} := n \times n$ matrix and is the reduced admittance matrix. The network reduction technique developed by Kron is an analytical model that is valid when the loads are exclusively designated as constant impedances. If the loads are of other load types, then the characteristics of the load buses must be preserved. Network reduction is applicable solely to the buses in the network with zero current injection [182, 185].

On the choice of load type for stability analysis, any load type is possible according to Ref. [57]. However, the choice of load type is determined by the nature of application and requirement. It was reported in [57] that a constant impedance load model is much more commonly used in disturbance simulation and stability analysis of power systems. Adopting varied load models will affect the analysis results. A composite load consisting of a constant impedance load, a constant power load, and a constant current load often described by the ZIP polynomial load model or a dynamic load like an induction motor is also possible. They are, however, much more realistic, according to some literature, but the focus on reducing the complex VISMA microgrid to direct interactions between VISMA virtual nodes will be difficult [163].

5.4.3 d-q to x-y coordinate model of VISMA microgrid

In a transmission network involving interconnectivity of different VISMAs system, change of variables is often necessary. VISMAs are represented in d-q coordinate system while the network is in DQ (x-y) coordinate system, as such for compatibility and easy analysis, harmonisation of the coordinate systems is sacrosanct. The subsystem of the microgrid consisting of the VISMAs, network, power controller and load were thus unified at x-y reference frame. This common reference frame is often called synchronously rotating reference frame (SRF) which is also called DQ coordinate [53, 54, 56]. Schematic of reference frame transformation is shown in figure 5.3.

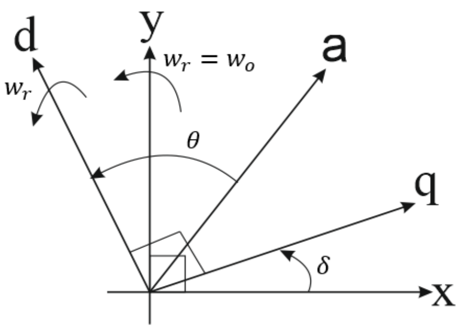

Figure 5.3. Reference frame transformation

For each VISMA, the transformation in the new x-y variable is achieved using the following equation [56, 142]:

$$\begin{bmatrix} f_d \\ f_q \end{bmatrix} = \begin{bmatrix} \sin(\delta) & -\cos(\delta) \\ \cos(\delta) & \sin(\delta) \end{bmatrix} \begin{bmatrix} f_x \\ f_y \end{bmatrix} \tag{5.15}$$

So that for each VISMA, the transformation in the new variable is achieved using the following equation [56, 142]:

$$\begin{bmatrix} i_{di} \\ i_{qi} \end{bmatrix} = \begin{bmatrix} sin\,\delta_i & -cos\,\delta_i \\ cos\,\delta_i & sin\,\delta_i \end{bmatrix} \begin{bmatrix} i_{xi} \\ i_{yi} \end{bmatrix} \tag{5.16}$$

Equation (5.15) is used in equation (2.45) so that the equations for current and voltage in the x-y coordinate system are then derived as follows:

$$\begin{bmatrix} u_{xi} \\ u_{yi} \end{bmatrix} = \begin{bmatrix} 0 & x_i \\ -x_i & 0 \end{bmatrix} \begin{bmatrix} i_{xi} \\ i_{yi} \end{bmatrix} + \begin{bmatrix} \cos\delta_i \\ -\sin\delta_i \end{bmatrix} e_{qi} \tag{5.17}$$

$$\begin{bmatrix} i_{xi} \\ i_{yi} \end{bmatrix} = \begin{bmatrix} 0 & -\frac{1}{X_i} \\ \frac{1}{X_i} & 0 \end{bmatrix} \left(\begin{bmatrix} u_{xi} \\ u_{yi} \end{bmatrix} - \begin{bmatrix} e_{qi}\cos\delta_i \\ e_{qi}\sin\delta_i \end{bmatrix} \right) \tag{5.18}$$

Similarly, the reduced network admittance matrix in (5.14) has an equivalent x-y coordinate form given by (5.19).

$$\boldsymbol{I_{Gxy}} = \boldsymbol{Y_{NG}U_{Gxy}} \tag{5.19}$$

Where I_{Gxy} and U_{Gxy} are respectively the x-y coordinate current and voltage of each VISMA. $\boldsymbol{Y_{NG}}$ is the x-y coordinate network admittance matrix, (5.19) can further be expressed as:

$$I_{Gxy} = (G_{Gx} + jB_{Gx})(U_{Gx} + jU_{Gy}) \tag{5.20}$$

Or in matrix form as:

$$\begin{bmatrix} I_{Gx} \\ I_{Gy} \end{bmatrix} = \begin{bmatrix} G_{Gx} & -B_{Gx} \\ B_{Gx} & G_{Gx} \end{bmatrix} \begin{bmatrix} U_{Gx} \\ U_{Gy} \end{bmatrix} \tag{5.21}$$

If there are *n*-VISMA in the network, then (5.21) is written in an expanded form as follows:

$$\begin{bmatrix} i_{x1} \\ i_{y1} \\ i_{x2} \\ i_{y2} \\ \vdots \\ i_{xn} \\ i_{yn} \end{bmatrix}_{2n\times 1} = \begin{bmatrix} G_{11} & -B_{11} & G_{12} & -B_{12} & \cdots & G_{1n} & -B_{1n} \\ B_{11} & G_{11} & B_{12} & G_{12} & \cdots & B_{1n} & G_{1n} \\ G_{21} & -B_{21} & G_{22} & -B_{22} & \cdots & G_{2n} & -B_{2n} \\ B_{21} & G_{21} & B_{22} & G_{22} & \cdots & B_{2n} & G_{2n} \\ \vdots & \vdots & \vdots & \vdots & \cdots & \vdots & \vdots \\ G_{n1} & -B_{n1} & G_{n2} & -B_{n2} & \ddots & G_{nn} & -B_{nn} \\ B_{n1} & G_{n1} & B_{n2} & G_{n2} & \cdots & B_{nn} & G_{nn} \end{bmatrix}_{2n\times 2n} = \begin{bmatrix} u_{x1} \\ u_{y1} \\ u_{x2} \\ u_{y2} \\ \vdots \\ u_{xn} \\ u_{yn} \end{bmatrix}_{2n\times 1} \tag{5.22}$$

In the d-q coordinate system, the electrical power output can be calculated using equation (2.41). But, in the *x-y* coordinate system, the power developed in the virtual airgap is calculated by substituting i_{qi} from (5.16) into (2.44), and this yield:

$$P_{ei} = e_{qi}(i_{xi} \cos\delta_i + i_{yi} \sin\delta_i) \tag{5.23}$$

Fig. 5.4. illustrates the schematic diagram of the stages involved in the variable transformation for achieving stability analysis of the VISMA microgrid.

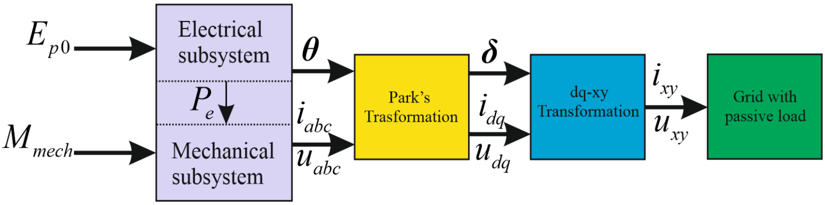

Figure 5.4. Stages of the entire system model

5.5 Small-signal linearized model of *n*-VISMA microgrid in x-y coordinate system

Intermittent and uncertain renewable power sources have a significant impact on the small-signal characteristics of the transmission network. However, there is a growing concern that supply fluctuations may cause transmission networks to operate closer to their stability boundaries [186]. Small-signal stability analysis thus becomes highly essential, and this is achieved by deriving the linear model of the nonlinear system [178]. Small signal analysis using linear technique provides useful information about the inherent dynamic characteristic of power systems and helps in its design [131]. The system performance may then be analysed by such methods like root-locus plots, frequency domain analysis (Nyquist criteria), and Routh's criterion. But for multivariable linear systems, state space model is often used. Stability characteristics may be determined by evaluating the eigenvalues of the system matrix [42]. Then, the linearized state-space model of VISMA microgrid to assess small-signal stability by eigenvalue analysis is derived based on the following sub-sections.

5.5.1 Linearized model of VISMA

If the virtual excitation is assumed constant (i.e. neglecting the impact of excitation system and voltage control), then e_{qi} is treated as a constant variable in (5.23). The active power injected at the VISMA virtual bus described by (5.23) is highly non-linear because of the transcendental functions. For a small disturbance, the transcendental functions are linearized by the relations [42]:

Assuming $y = \sin(\delta_i)$, then $y + \Delta y = \sin(\delta_i + \Delta\delta_i)$, and by neglecting the higher order terms we have $\Delta y = \Delta\delta_i \cos(\delta_i)$. Similarly, if $y = \sin(\delta_i)$, then $\Delta y = -\Delta\delta_i \sin(\delta_i)$

The linearized model of (5.15) yield;

$$\begin{bmatrix}\Delta f_d \\ \Delta f_q\end{bmatrix} = \begin{bmatrix}\sin(\delta) & -\cos(\delta) \\ \cos(\delta) & \sin(\delta)\end{bmatrix}\begin{bmatrix}\Delta f_x \\ \Delta f_y\end{bmatrix} + \begin{bmatrix}\cos(\delta) & \sin(\delta) \\ -\sin(\delta) & \cos(\delta)\end{bmatrix}\begin{bmatrix}f_x \\ f_y\end{bmatrix}\Delta\delta \tag{5.24}$$

Linearization of (5.23) is critical to obtaining the system matrix and is derived in matrix form as follows:

$$\Delta P_{ei} = \left(\begin{bmatrix}e_{qi}\cos(\delta_i) & e_{qi}\sin(\delta_i)\end{bmatrix}\begin{bmatrix}\Delta i_{xi} \\ \Delta i_{yi}\end{bmatrix} + e_{qi}\cdot\begin{bmatrix}-\sin(\delta_i) & \cos(\delta_i)\end{bmatrix}\begin{bmatrix}i_{xi} \\ i_{yi}\end{bmatrix}\right)\Delta\delta_i \tag{5.25}$$

Where, $i_{xyi} = [i_{xi} \quad i_{yi}]^T$ is the real and imaginary component of the current injected at the i^{th} terminal of the i^{th} VISMA, and $u_{xyi} = [u_{xi} \quad u_{yi}]^T$ is the real and imaginary components of the voltage at the terminal bus of the i^{th} VISMA. The voltage and current components are in the synchronously-rotating network frame of reference, and are each in per-unit on their respective network base quantities. The linearized voltage and current injection at the i^{th} terminal of i^{th} VISMA bus in the x-y coordinates system is obtained in compact form as follows:

$$\begin{bmatrix}\Delta i_{xi} \\ \Delta i_{yi}\end{bmatrix} = \begin{bmatrix}0 & -\frac{1}{x_i} \\ \frac{1}{x_i} & 0\end{bmatrix}\begin{bmatrix}\Delta U_{xi} \\ \Delta U_{yi}\end{bmatrix} + \frac{e_{qi}}{x_i}\cdot\begin{bmatrix}\cos(\delta_i) \\ \sin(\delta_i)\end{bmatrix}\Delta\delta_i + \frac{1}{x}\begin{bmatrix}\sin(\delta_i) \\ -\cos(\delta_i)\end{bmatrix}\Delta e_{qi} \tag{5.26}$$

$$\begin{bmatrix}\Delta U_{xi} \\ \Delta U_{yi}\end{bmatrix} = \begin{bmatrix}0 & x_i \\ -x_i & 0\end{bmatrix}\begin{bmatrix}\Delta i_{xi} \\ \Delta i_{yi}\end{bmatrix} + e_{qi}\begin{bmatrix}-\sin(\delta_i) \\ \cos(\delta_i)\end{bmatrix}\Delta\delta_i \tag{5.27}$$

$$\Delta u_{xyi} = X_{gi}\Delta i_{xyi} + M_i\Delta\delta_i \tag{5.28}$$

Where:

$$\begin{bmatrix}\Delta i_{xi} \\ \Delta i_{yi}\end{bmatrix} = \Delta i_{xyi}; \begin{bmatrix}\Delta u_{xi} \\ \Delta u_{yi}\end{bmatrix} = \Delta u_{xyi}; \begin{bmatrix}0 & -x_i \\ x_i & 0\end{bmatrix} = X_{gi}; \begin{bmatrix}-\sin(\delta_i) \\ \cos(\delta_i)\end{bmatrix}e_{qi} = M_i$$

For *n*-VISMA in the network, (28) is reformulated as;

$$\boldsymbol{\Delta U_{xy}} = \boldsymbol{X_g\Delta I_{xy}} + \boldsymbol{M_D\Delta\delta} \tag{5.29}$$

Where:

$\Delta\boldsymbol{U_{xy}} = [\Delta u_{xy,1} \quad \Delta u_{xy,2} \quad \cdots \quad \Delta u_{xy,n}]^T$, $2n \times 1$ matrix

$\Delta\boldsymbol{I_{xy}} = [\Delta i_{xy,1} \quad \Delta i_{xy,2} \quad \cdots \quad \Delta i_{xy,n}]^T$, $2n \times 1$ matrix

$\Delta\boldsymbol{\delta} = [\Delta\delta_1 \quad \Delta\delta_2 \quad \cdots \quad \Delta\delta_n]^T$, $n \times 1$ matrix

The matrices $\boldsymbol{X_g}$ und $\boldsymbol{M_D}$ are composed of sub-matrices $X_{g,i}$ and M_i in diagonal elements:

$\boldsymbol{X_g} = diag(X_{g,1} \quad X_{g,2} \quad \cdots \quad X_{g,n})$; $\boldsymbol{M_D} = diag(M_1 \quad M_2 \quad \cdots \quad M_n)$

5.5.2 State space modelling of the network and load

linearizing (5.19) yield:

$$\Delta\boldsymbol{I_{Gxy}} = \boldsymbol{Y_{NG}}\Delta\boldsymbol{U_{Gxy}} \tag{5.30}$$

Where $\boldsymbol{Y_{NG}} = 2n \times 2n$ matrix. Substituting (5.29) in (5.30) to eliminate the vector of VISMA terminal voltages yields:

$$\Delta\underline{\boldsymbol{I}}_{\boldsymbol{xy}} = (\boldsymbol{I} - \boldsymbol{Y_{NG}}\boldsymbol{X_G})^{-1}\boldsymbol{Y_{NG}}\boldsymbol{M}\Delta\boldsymbol{\delta} = \boldsymbol{Y_{EN}}\boldsymbol{M}\Delta\boldsymbol{\delta} \tag{5.31}$$

$\boldsymbol{Y_{EN}} = (\boldsymbol{I} - \boldsymbol{Y_{NG}}\boldsymbol{X_G})^{-1}\boldsymbol{Y_{NG}}$ is called *effective network admittance matrix*, and it is of same dimension as $\boldsymbol{Y_{NG}}$, $\boldsymbol{I}$ is an identity matrix of $2n \times 2n$ dimension. For *n*-VISMA, (5.23) is reformulated as follows:

$$\Delta\boldsymbol{P_{en}} = \left[\boldsymbol{L}.\Delta\underline{\boldsymbol{I}}_{\boldsymbol{xy}} + diag\left(\boldsymbol{M^T}\underline{\boldsymbol{I}}_{\boldsymbol{xy}}\right)\right]\Delta\boldsymbol{\delta} \tag{5.32}$$

Where:

$\underline{\boldsymbol{I}}_{\boldsymbol{xy}} = [i_{xy,1} \quad i_{xy,2} \quad \cdots \quad i_{xy,n}]^T =$ Vector of VISMA output currents in DQ coordinate

$L_i = e_{qi}.[\cos(\delta_i) \quad \sin(\delta_i)]$

The matrix $\boldsymbol{L}$ is composed of sub-matrices L_i in diagonal elements:

$\boldsymbol{L} = diag(L_1 \quad L_2 \quad \cdots \quad L_n)$

The vector of VISMA output currents in $x - y$ synchronous coordinate when the entire network is reduced to direct interactions between the internal virtual nodes is given by;

$$\underline{\boldsymbol{I}}_{\boldsymbol{xy}} = \boldsymbol{Y}_{\boldsymbol{EN}}\underline{\boldsymbol{E}}_{\boldsymbol{q,xy}} \tag{5.33}$$

Where

$$\underline{\boldsymbol{E}}_{\boldsymbol{q,xy}} = \begin{bmatrix} e_{q,xy,1} & e_{q,xy,2} & \cdots & e_{q,xy,n} \end{bmatrix} \quad and \quad \boldsymbol{e}_{\boldsymbol{q,xy,i}} = e_{qi}\cdot\begin{bmatrix} cos(\delta_i) \\ sin(\delta_i) \end{bmatrix}$$

Substituting (5.31) and (5.33) in (5.32) for n-VISMA yields:

$$\Delta P_{en} = \left[L.Y_{EN}.M + diag\left(M^T Y_{EN}\underline{E}_{q,xy}\right)\right]\Delta\delta_n = H_n\Delta\delta_n \tag{5.34}$$

Where $H_n = \left[L.Y_{EN}.M + diag\left(M^T Y_{EN}\underline{E}_{q,xy}\right)\right]$ and $\Delta\delta_n = \Delta\delta$

H_n is the System Jacobi or Laplacian matrix and is of dimension $n \times n$ matrix, $\Delta P_{en}\ and\ \Delta\delta_n$ are of dimension $n \times 1$. $L.Y_{EN}.M$ and $\mathrm{diag}\left(M^T Y_{EN}\underline{E}_{q,xy}\right)$ are of $n \times n$ matrix. In the preserved state space model of the VISMA microgrid shown in Fig. 5.5, the physical structure of the transmission network connecting the load nodes to the power sources is fully represented by $\boldsymbol{Y}_{\mathbf{bus}}$, this comes with complexity associated with larger set of equations as a result of increased number of nodes and it thus makes stability analysis cumbersome.

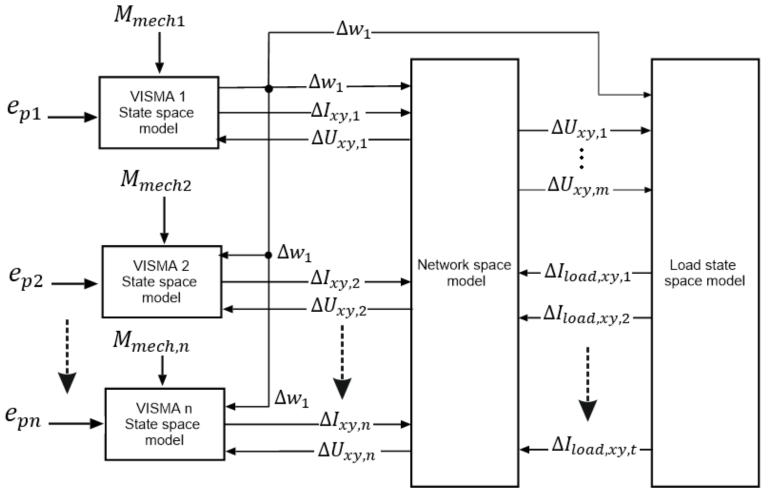

Figure 5.5. Complete small-signal model of *n*-VISMA microgrid

However, to achieve network reduced model, loads are represented as constant impedances, and this enables coupling (transmission lines and loads) between generators to be reduced to a single term that depends only on state variables of the VISMAs. Thus, the interaction between the internal nodes of the *n*-VISMA after the elimination of the load and lines is illustrated in Fig. 5.6.

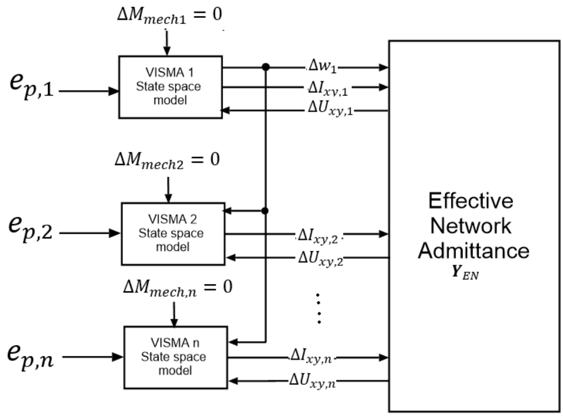

Figure 5.6. Internal nodes interactions in the *n*-VISMA microgrid

The linearized expression of active power injection by *n*-VISMA in (5.34) can also be of the form:

$$\begin{bmatrix} \Delta P_{e1} \\ \Delta P_{e2} \\ \vdots \\ \Delta P_{en} \end{bmatrix} = \begin{bmatrix} H_{11} & H_{12} & \cdots & H_{1,n} \\ \vdots & \vdots & \ddots & \vdots \\ H_{n,1} & H_{n,2} & \cdots & H_{n,n} \end{bmatrix} \begin{bmatrix} \Delta \delta_1 \\ \Delta \delta_2 \\ \vdots \\ \Delta \delta_n \end{bmatrix} \tag{5.35}$$

Equation (5.35) shows that the change in electrical power in any VISMA as a result of small disturbance is a function of change in the rotor angle of all VISMA across the network. The two major components of *H* matrix are defined as follows:

- H_{ii}: The diagonal elements of *H* matrix describe the total individual synchronizing torque contribution of each VISMA to the network.
- H_{ij}: Off diagonal elements of *H* matrix describe the interactive synchronizing torque between VISMAs in the network.

In power system stability, it is unconventional to consider each rotor angle as a state variable since the loss of synchronism does not translate to all rotor angles increasing simultaneously, instead of having all the angles moving, it is essential to select a reference VISMA, and then examine other individual VISMA rotor angles relative to the reference VISMA [54]. This helps to access whether the rotor angles remain relatively bounded or not. If the virtual rotor angle of n^{th} VISMA is assumed as the common reference, then (5.34) is written in the relative angle form as follows:

$$\Delta P_{e,n-1} = H_{n-1}\Delta\delta_{n-1} \tag{5.36}$$

Where H_{n-1} is an $n \times (n-1)$ matrix dimension and $\Delta\delta_{n-1}$ is the vector of relative rotor angles between the common reference VISMA n, and any i^{th} node of other VISMA in the interconnected system. The stability of a linear dynamic system is completely not dependent on the input and initial operating condition [131]. For free motion dynamics, the swing equation defined (2.46) – (2.47) is linearized as two first order differential equations in per unit as follows [27]:

$$\begin{cases} \frac{d\Delta\omega_{ri}}{dt} = -\frac{\Delta P_{ei}}{T_{a_i}} - \frac{D_i}{T_{a_i}}\Delta\omega_{ri} \\ \frac{d\Delta\delta_i}{dt} = \omega_b\Delta\omega_{ri} \end{cases} \tag{5.37}$$

Where $\Delta\omega_{ri}$ is the pu speed deviation, $T_{a_i} = 2H_i$ (mechanical time constant) and Δ is the linear operator. The interaction between the internal nodes of the *n*-VISMA is illustrated in Fig. 5.6. Considering (5.36) and (5.37), the linearized state space-model representing microgrid dynamics is formulated as:

$$\Delta\dot{x} = Ax \tag{5.38}$$

Where x is the system state variables and is defined as;

$$x = \left[\begin{array}{cccc|cccc|c} \Delta\delta_{1n} & \Delta\delta_{2n} & \cdots & \Delta\delta_{(n-1),n} & \Delta w_1 & \Delta w_2 & \cdots & \Delta w_{n-1} & \Delta w_n \end{array}\right]^T \tag{5.39}$$

$$A = \left[\begin{array}{cccc|cccc|c}
0 & 0 & \cdots & 0 & w_b & 0 & \cdots & 0 & -w_b \\
0 & 0 & \cdots & 0 & 0 & w_b & \cdots & 0 & -w_b \\
\vdots & \vdots & \ddots & \vdots & \vdots & \vdots & \ddots & \vdots & \vdots \\
0 & 0 & \cdots & 0 & 0 & 0 & \cdots & w_b & -w_b \\
\hline
-\dfrac{H_{11}}{T_{a1}} & -\dfrac{H_{12}}{T_{a1}} & \cdots & -\dfrac{H_{1,n-1}}{T_{a1}} & -\dfrac{D_1}{T_{a1}} & 0 & \cdots & 0 & 0 \\
-\dfrac{H_{21}}{T_{a2}} & -\dfrac{H_{22}}{T_{a2}} & \cdots & -\dfrac{H_{2,n-1}}{T_{a2}} & 0 & -\dfrac{D_2}{T_{a2}} & \cdots & 0 & 0 \\
\vdots & \vdots & \ddots & \vdots & \vdots & \vdots & \ddots & \vdots & \vdots \\
-\dfrac{H_{(n-1),1}}{T_{a,(n-1)}} & -\dfrac{H_{(n-1),2}}{T_{a,(n-1)}} & \cdots & -\dfrac{H_{(n-1),(n-1)}}{T_{a,(n-1)}} & 0 & 0 & \cdots & -\dfrac{D_{n-1}}{T_{a,(n-1)}} & 0 \\
\hline
-\dfrac{H_{n1}}{T_{a,n}} & -\dfrac{H_{n2}}{T_{a,n}} & \cdots & -\dfrac{H_{n,(n-1)}}{T_{a,n}} & 0 & 0 & \cdots & 0 & -\dfrac{D_n}{T_{a,n}}
\end{array}\right] \tag{5.40}$$

Evaluation of the eigen properties of system matrix ***A*** provides vital information concerning the stability characteristics of the dynamic system. **A** is a Jacobian matrix whose elements are given by the partial derivatives estimated at the equilibrium point about which the small disturbance is being analysed.

5.6 Stability Analysis of *n*-VISMA Model in Autonomous Mode

5.6.1 Validation of the proposed model

The validation of the proposed small-signal analytical model designed to operate in autonomous mode is implemented on the standard IEEE-9 bus system. In order to effectively analyze VISMA operation on this network, additional virtual buses are introduced. These buses are equivalent to the internal nodes of the conventional ESM on the network. The physical buses are labelled as shown in Fig. 3.3., i.e. each bus number is shifted up by 3 when compared with the standard IEEE-9 bus system. The virtual buses of VISMA 1, VISMA 2 and VISMA 3 are numbered as 1, 2 and 3 respectively. The parameters for the VISMAs in Fig. 3.3 are given in Table 5.1 while the line and load bus parameters are obtainable in [42]. On the validity of the proposed numerical analytics, the dynamic responses of the small-signal model are compared with those of the NL system dynamics built in SIMULINK environment according to Fig. 4.4. The fact that the hysteresis current controller operates at a specific tolerance band, the switching frequency of the converter is not stable but varies within a frequency band, thereby introducing harmonics with different frequency terms in the output currents [20]. Thus, to avoid this problem and at the same time simplify the analysis, current controlled source inverter (CCSI) is used to model three-phase inverters.

Table 5.1. Parameters for IEEE-9 bus VISMA microgrid

Description	Symbol	VISMA 1	VISMA 2	VISMA 3
Shunt capacitance, $\times 10^{-5}$, pu	C_f	3.1740	3.1740	3.1740
Virtual inductance, $\times 10^{-4}$, pu	L_s	1.6128	3.1778	4.8091
Virtual inertia (sec)	H	23.64	6.40	3.01
Virtual damping (p.u)	D	150	200	250
Static droop coefficients, pu	m_p	0.13	0.01	0.04
Active power PI controller integral gain	K_i	$1e^{-5}$	$1e^{-5}$	$1e^{-5}$
Active power PI controller proportional gain	K_p	0.01	0.01	0.01
Pole wheel voltage (p.u)	E_o	1.0566	1.0502	1.0170
Virtual torque input, (p.u)	P_{m0}	0.716	1.630	0.85 .5
Rated frequency	f_b	60 Hz		

Fig. 5.7 depicts the grid frequency dynamics of the two models under comparison. At $t = 3$ sec, there was a step increase in the virtual mechanical input to VISMA 2 from 1.63 pu to 1.8 pu while the mechanical inputs to other VISMAs remain unchanged. Before the disturbance, the small-signal model and NL model are well merged. A set of other results comparing the NL simulations and the linearized small signal are depicted in Fig. 5.8 to Fig. 5.10. The power output dynamic responses of the two models are shown in Fig. 5.8. Considering spaces, only the D and Q components of VISMA2 output currents for both categories of models have been shown in Fig. 5.9. Similarly, Fig. 5.10 represents the dynamic responses of rotor angles of the three VISMAs. It is clear from all the illustrations that the linearized small-signal (LS) model presented in previous section is sufficient for rotor angle stability study and analysis.

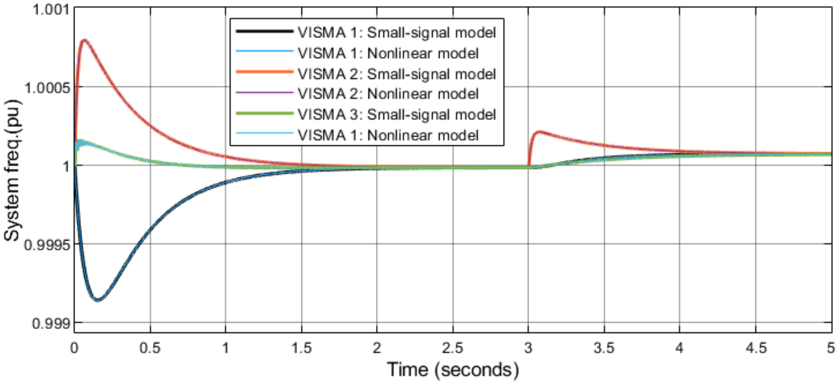

Figure 5.7. Comparing step response in frequency (pu) for both NL and LS models due to step change in input torque

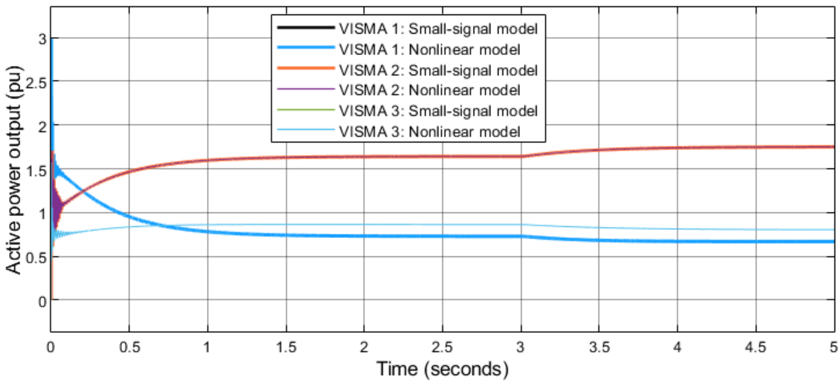

Figure 5.8. Comparing step response in output power (pu) for both NL and LS models due to step change in input torque

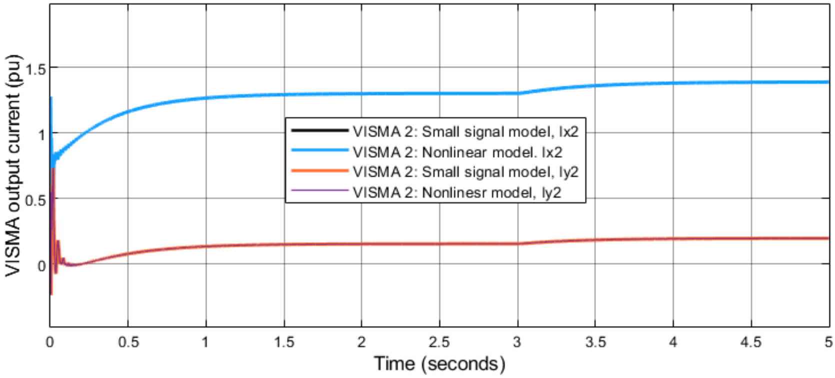

Figure 5.9. Comparing step response in output current (pu) for both NL and LS models due to step change in input torque

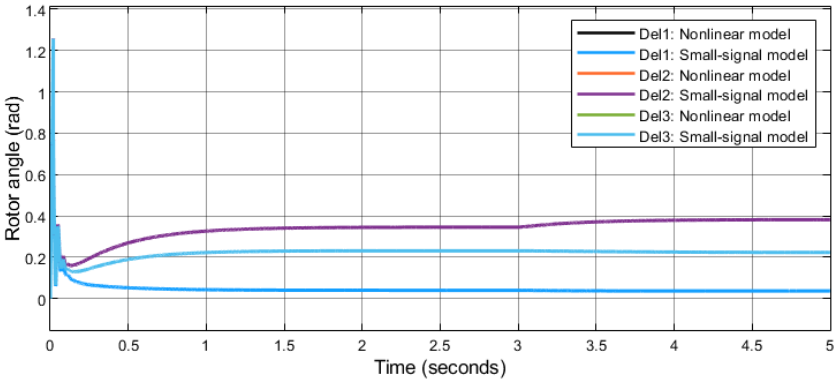

Figure 5.10. Comparing step response in rotor angle (pu) for both NL and LS models due to step change in input torque

5.6.2 System Eigenvalues Analysis

It has been demonstrated earlier that the developed LS model is sufficient to reliably characterize the behaviour of the dynamic VISMA microgrid when operated in autonomous mode. Eigenvalue analysis, which is a frequency domain approach, is a very powerful tool for characterizing small signal stability of a power system and is employed here to investigate the dynamic stability condition of the VISMA microgrid around the stationary operating points, according to Lyapunov stability criterion. To investigate the effect of damping on the pole movement in the PZ map, three different cases of damping representations have been considered for the relative angle stability, as shown in Fig. 5.11. Table of eigenvalues for a case of different values of damping is given in Table 5.2. At D = 0 for all the three VISMAs on the network, all of the system poles lie on the imaginary axis of the PZ-map. With this, the microgrid experiences undamped oscillations. At D = 30 for all VISMAs, all the modes are complex with negative real parts and the power system experiences an underdamped oscillation. The transient response of the *underdamped systems* consists of two parts, namely an exponentially decaying amplitude actuated by the real part of the system pole and a sinusoidal waveform provided by the imaginary part of the system pole. At, $D_1 = 150, D_2 = 200$ and $D_3 = 250$, there exist two pairs of complex conjugate oscillatory modes with negative real part and one negative real value as shown in Table 5.2, which is the damping case for the investigated system.

Table 5. 2. System Eigenvalues

Damping		Mode	Eigenvalues	Frequency (Hz)	Damping ratio
Case 1	$D_1 = 0$	Mode 1	-0.0000 $\pm$13.3592i	2.1262	0.0000
	$D_1 = 0$	Mode 2	-0.0000$\pm$8.6882i	1.3828	0.0000
	$D_1 = 0$	Mode 3	0.0000	-	-
Case 2	$D_1 = 30$	Mode 1	-2.2284 $\pm$13.1154i	2.1168	0.1680
	$D_1 = 30$	Mode 2	-1.0354 $\pm$ 8.5814i	1.3751	0.1200
	$D_1 = 30$	Mode 3	-1.4340	0.0000	1.0000

Case 3	$D_1 = 150$	Mode 1	-37.5676	0.0000	1.0000
	$D_2 = 200$	Mode 2	$-8.4487 \pm 4.7816i$	0.7610	0.8703
	$D_3 = 250$	Mode 3	$-2.9305 \pm 5.2265i$	0.8318	0.4891

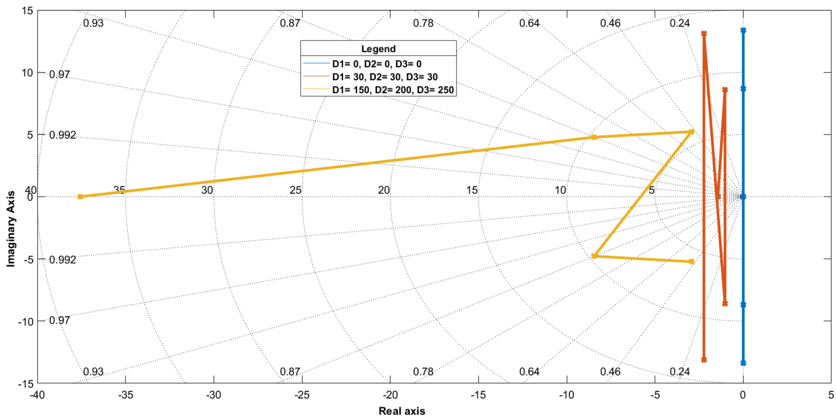

Figure 5.11. Impact of damping on system pole locations

5.6.3 Parameter sensitivities and Participation factor in small signal stability analysis of *n*-VISMA Microgrid

The basis of eigenvalue analysis lies on the premise that with the penetration of distributed power sources, the effective inertia of the system will be reduced. As such, it is imperative to understand how small-signal stability behaviour will change with the change in system inertia and system damping. Analysis of the dynamic stability by temporary changing of the system control parameters and evaluation of corresponding system eigenvalues is tedious for a multimachine power system. Instead, selective modal analysis is carried out where the poles with fast decaying transients are insignificant [35, 127]. In that case, the sensitivity of the dominant poles with respect to the system parameters are prioritized and examined so as to uncover the extent to which each parameter impacts on the system modes and more so to identify measures that might ensure satisfactory performance and stability of the microgrid. The parameter sensitivity of the system poles is defined as the derivative of the eigenvalues with respect to the system parameters [106]. Considering n-VISMA microgrid with k tunable parameters, the relative sensitivity $\alpha_{n,k}$ of the parameter β_{kj} with respect to the eigenvalue n is defined in (5.41), where $\boldsymbol{\psi_n}$ and $\boldsymbol{\Phi_n}$ are the left and right eigenvectors associated to the eigenvalue λ_n [35, 53].

$$\alpha_{n,k} = \frac{d\lambda_n}{d\beta_k} = \boldsymbol{\psi_n} \frac{d\boldsymbol{A}}{d\beta_{kj}} \boldsymbol{\Phi_n} \tag{5.41}$$

Sensitivity is a good indication of parameter to a mode. The real side of the sensitivities has a direct relationship with the derivatives of the eigenvalue location along the real axis with respect to each parameter β_k. A positive sensitivity value associated with a particular mode means an increase in that parameter will shift the complementary eigenvalue further to the right thereby increasing the system instability. In the same manner, the imaginary side of the sensitivity is related to the derivative of the pole location along the imaginary axis [35]. Knowing that the stability of a dynamical system is often indicated by the real part of the system poles, only the real side of the sensitivity matrix has been studied. A specific damping case $D_1 = 150, D_2 = 200$ and $D_3 = 250$ for the three VISMAs on the network has been considered for parameter sensitivity and PF analysis. Figure 5.12 illustrates parameter sensitivity of the slowest pole (having the largest time constant) which also double as the most poorly damped poles in the system. From this figure, nearly all the tunable parameters of the VISMAs considered have significant influence on the system stability with the least impact coming from D_3. The dynamic response of the microgrid can however be improved by reducing T_{a1} or D_2 or D_3, or increasing D_1 or T_{a2} or T_{a3}.

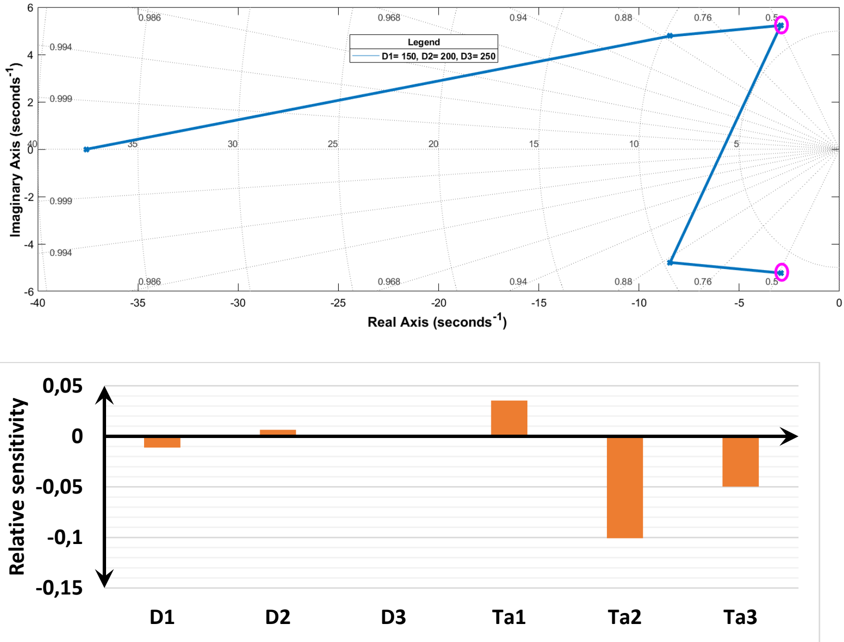

Figure 5.12. Parameter sensitivity of the Dominant system pole

The contribution of this pole to the transient response may be significant but is not a severe pole as to put the microgrid in a precarious state. Similarly, the oscillatory mode studied in Fig. 5.13 is heavily impacted by T_{a2}, T_{a3} and lightly affected by D_2. Decreasing parameter T_{a2}, or increasing D_2 or T_{a3} would move the pole further away to the left of the imaginary axis and thereby improving the dynamic response of the microgrid.

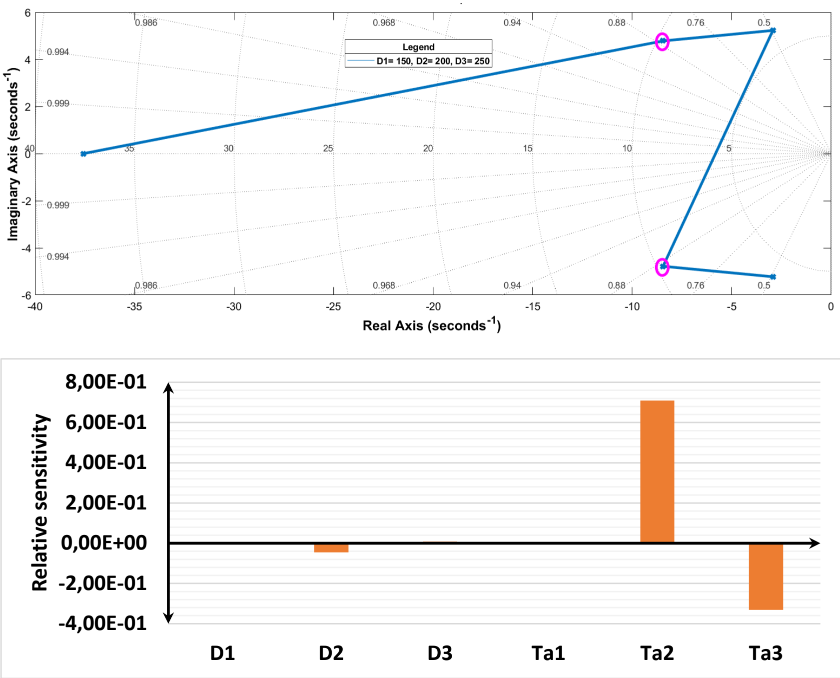

Figure 5.13. Parameter sensitivity of the fastest oscillatory mode

However, this pole is not so severe as to induce instability in the system. Since these parameters cannot change during the natural healthy operation, they are also unlikely cause system instability. To enhance the operational performance of the microgrid especially for the poles that are close to the imaginary axis, parameter sensitivities play a crucial role in the tuning of the system, which is achieved either by manual adjustment or autoregulation scheme [21, 34].

PF is a measure of the sensitivity of a particular mode to the diagonal elements of the system matrix and is equal to $\alpha_{n,k}$ when $k = j$ in (5.41) [53, 142]. PF plays a vital role in power system stability analysis, according to [54], it can be used to identify the specific device that is mainly responsible for the system instability and thus helps to establish the necessity for power system stabilizer in the system. PF can be positive, zero, or negative. In regards to the rotor angle stability, a positive PF related to a specific VISMA implies that the VISMA in question is having a contributory effect on the swinging of the rotor, while a negative PF implies that the VISMA is dampening the rotor swinging. If PF for VISMAs are negative, then introducing a PSS would increase the oscillations in the system [187].

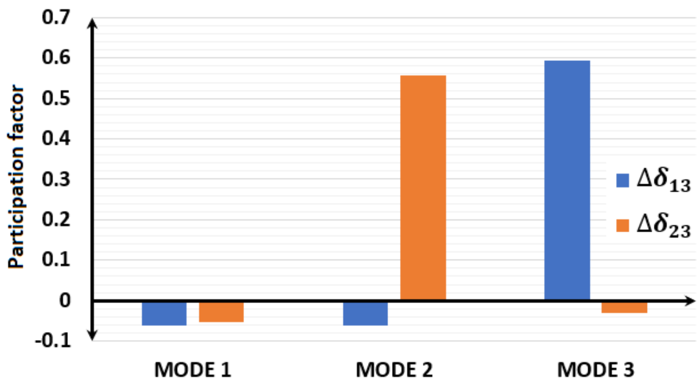

Figure 5.14. Modal effect on relative rotor swinging participations

Fig. 5.14 shows the modal participations on the relative rotor swinging. Here, VISMA 3 is assumed to be the common reference so that magnitude of the rotor swinging in VISMA 1 and VISMA 2 is measured with respect to VISMA 3 i.e. $\Delta\delta_{13}$ *and* $\Delta\delta_{23}$. According to the Figure 5.14, mode 1 does not contribute to the rotor swinging, it rather dampens the oscillations in the system. Mode 2 has a significance impact on the swinging of VISMA rotor 2 while the same mode has a positive impact in damping the oscillations of VISMA rotor 1. Similarly, Mode 3 significantly influences the swinging of VISMA rotor 1 while correspondingly dampening the oscillations of VISMA rotor 2. Now, it is desired to remove the need for machine relativity so as to be able to study the behaviour of each rotors to parameter changes. It is seen from Fig. 5.14 that VISMA 1 is majorly impacted by the dominant mode 3, its participation in the system oscillation can be improved by increasing D_1 as suggested earlier but care should be taken such that it does not have a negative ripple effect on increasing the oscillatory participations of other VISMAs to the specified mode. Fig. 5.15 illustrates the effect of increasing D_1 on the oscillatory participations of the virtual rotors in the network. Obviously, while the participation level of VISMA1 and VISMA 3 are reducing, that of VISMA 2 is increasing. The virtual rotor performance in the microgrid stability can however be improved if increase in D_1 is accompanied by corresponding decrease in D_2. As shown in Fig. 5.15, the yellow line show that the effective participation of rotors in the system oscillations drops.

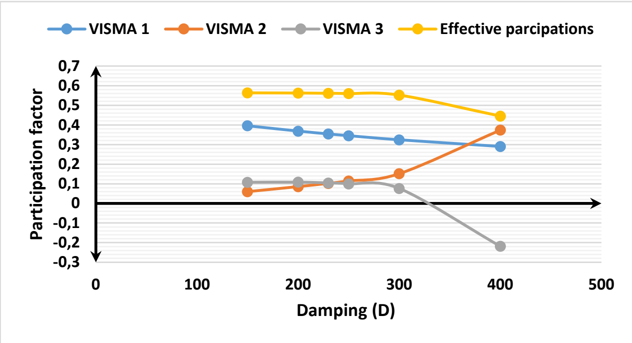

Figure 5.15. Effect of damping on the oscillatory participations of virtual rotors

6. Rotor Angle Stability and Parametric Sensitivity of *n*-VISMA With Outer Power Loop Controller

6.1 Introduction

The natural VISMA model presented in chapter 5 does not incorporate outer power controllers, the active and reactive power regulations were respectively achieved by setting the model parameters virtual torque and virtual excitation. The fundamental assumptions in classical stability analysis that the effect of mechanical torque for small-signal study is negligible often lead to an incorrect result. This chapter presents a comprehensive small-signal rotor angle stability analysis of a multi-virtual synchronous machine to demonstrate the impact of external power loop controllers on the electromechanical dynamics of VISMA microgrid. The presented work addresses an interesting phenomenon that may occur when a PLC is installed to support frequency stability. This control structure makes it possible to set the respective ancillary services in a targeted manner as shown in Fig. 6.1. In the multi-VISMA microgrid presented, each VISMA unit is designed to have an independent localized control so that fundamental active and reactive powers can be shared based on individualized static droop coefficients. The approach here is to obtain a generalized state space model for *n*-VISMA microgrid and then analyse the inherent electromechanical oscillations in the virtual rotors around an equilibrium point.

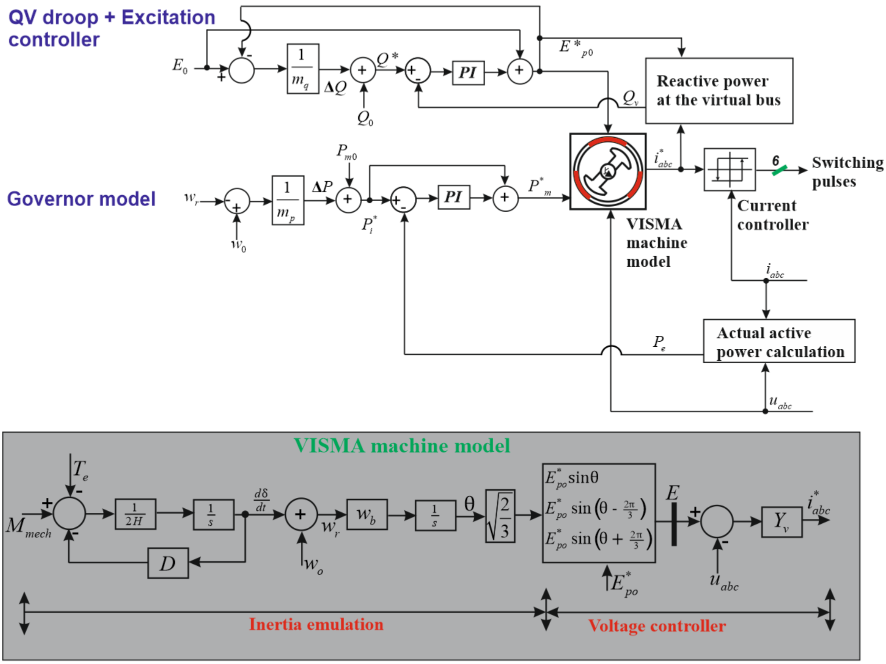

Figure 6.1. VISMA model with control.

In this representation, external power loop controller is added to allow for full flexibility of operation of the microgrid, this also allowed for proper power sharing among the participating power sources.

6.2 Modelling of Outer Power Controller

When disturbances occur, rotor angle is deviated from the balance position and this must be corrected by rapid automatic adjustment of the virtual mechanical power. Similarly, the automatic voltage regulation (AVRs) helps to provide the primary voltage control by appropriate adjustment of reactive power, Q [186] which ensures that pole wheel voltage is kept equal to the VISMA voltage set-point, i.e. $E_{po}^{*} = E_0$. Q_v, is the reactive power injected at the virtual bus which is compared with reactive power reference Q^* generated from the reactive droop control. Control loop for Q is only provided here for the benefit of the readers but is not included in the analysis since excitation is assumed constant. In an n-VISMA microgrid, static droop coefficients $(m_p \; and \; m_q)$ are used to actuate power sharing among the DGs. In this control model, each VISMA is equipped with one AVR and one governor model. The power reference P_i^* is obtained based on the conventional droop and is given by:

$$w_i - w_o = -m_{pi}(P_i^* - P_{mo,i}) \tag{6.1}$$

Where P_{mo}, is the set point of the virtual mechanical power input to the VISMA. The PI controller ensures that the power actually fed in the steady state corresponds to the setpoints without any deviation. The adjusted virtual mechanical power input reference to the VISMA is defined by (6.2) as follows:

$$P_{mi}^* = (P_i^* - P_{e,i})\left(K_{p,i} + \frac{K_{i,i}}{s}\right) + P_i^* \tag{6.2}$$

Where $K_{p,i}, K_{i,i}$ respectively defines proportional and integral controller gains of the active power controller.

Let

$$\frac{d\gamma_i}{dt} = P_i^* - P_{e,i} \tag{6.3}$$

so that;

$$P_{mi}^* = K_{p,i}(P_i^* - P_{e,i}) + K_{i,i}\,\gamma + P_i^* \tag{6.4}$$

The dynamic behavior of n-VISMA system can be established by modelling the acceleration of each VISMA as the difference between the controlled mechanical input power P_{mi}^* and actual electrical output power P_{ei}, which is governed by the following swing equation [27, 57, 163];

$$2H_i \frac{dw_{ri}}{dt} = P_{mi}^* - P_{ei} - D_i \frac{d\delta_i}{dt} \; and \; \frac{d\delta_i}{dt} = w_b(w_{ri} - w_s) \tag{6.5}$$

By linearizing and manipulating (6.2) – (6.5), and also putting relative rotor angles into consideration, the following equations are derived:

$$\frac{d\Delta\gamma_i}{dt} = -\frac{\Delta w_i}{m_{pi}} - \Delta P_{e,n-1} \tag{6.6}$$

$$\frac{d\Delta w_i}{dt} = \frac{1}{T_{a,i}}\left[K_{i,i}\,\Delta\gamma - \left(\frac{K_{p,i}+1}{m_{pi}} + D_i\right)\Delta w_i - \left(K_{p,i}+1\right)\Delta P_{e,n-1}\right] \tag{6.7}$$

The linearized state space model representing n-VISMA microgrid when external active power controller dynamics is included is formulated as:

$$\frac{dx}{dt} = \dot{x} = A = \begin{bmatrix} A_{11} & A_{12} & A_{13} & A_{14} & A_{15} \\ A_{21} & A_{22} & A_{23} & A_{24} & A_{25} \\ A_{31} & A_{32} & A_{33} & A_{34} & A_{35} \\ A_{41} & A_{42} & A_{43} & A_{44} & A_{45} \\ A_{51} & A_{52} & A_{53} & A_{54} & A_{55} \end{bmatrix} x \tag{6.8}$$

The elements of **A** matrix are defined in the appendix while x is the system state variables and is defined as;

$$x = \left[\begin{array}{cccc:cccc:c:cccc:c} \Delta\delta_{1n} & \Delta\delta_{2n} & \cdots & \Delta\delta_{(n-1),n} & \Delta w_1 & \Delta w_2 & \cdots & \Delta w_{n-1} & \Delta w_n & \Delta\gamma_1 & \Delta\gamma_2 & \cdots & \Delta\gamma_{n-1} & \Delta\gamma_n \end{array}\right]^T \tag{6.9}$$

Evaluation of the eigen properties of system matrix **A** provides vital information concerning the stability characteristics of the dynamic system. The interaction between the internal nodes of the n-VISMA with decentralized control is illustrated in Fig. 6.2.

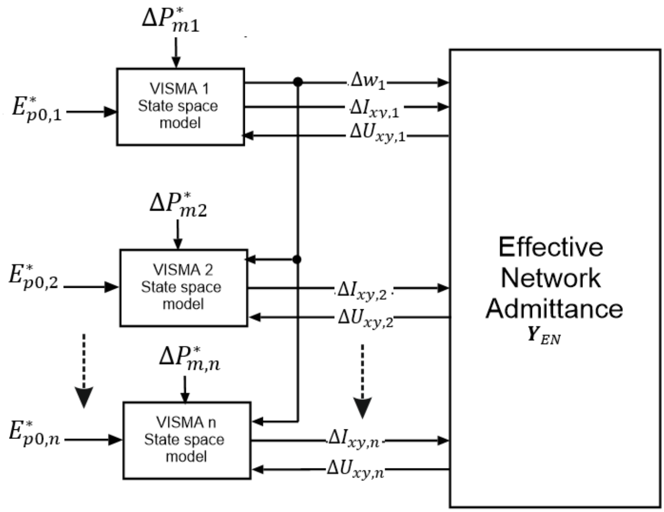

Figure 6.2. Internal node interactions between *n*-VISMA with decentralized PLC controller

6.3 Comparative System Eigenvalues Analysis between VISMA with and without active PLC

The small-signal model is further used here to investigate the dynamic stability condition of the VISMA microgrid incorporating an externally added decentralized control. The effect of damping on the system response is investigated by considering three different damping representation in a way similar to that obtained in chapter 5. Table 6.1 shows the system eigenvalues for VISMA with an externally controlled power loop. A negative real eigenvalue corresponds to an aperiodic response while the complex mode which often appears as complex conjugate represents an oscillatory mode.

Table 6.1. System Eigenvalues

	Damping	Mode	Eigenvalues	Frequency (Hz)	Damping ratio
Case 1	$D_1 = 0$	Mode 1	-2.3355 $\pm$13.0976i	2.0846	0.1756
	$D_1 = 0$	Mode 2	-2.5145 $\pm$ 7.7479i	1.2331	0.3087
	$D_1 = 0$	Mode 3	-2.5492	0.0000	1.0000
Case 2	$D_1 = 30$	Mode 1	-4.6329 $\pm$12.5477i	1.9970	0.3464
	$D_1 = 30$	Mode 2	-3.0112 $\pm$ 6.8476i	1.0898	0.4025
	$D_1 = 30$	Mode 3	-4.9228	0.0000	1.0000
Case 3	$D_1 = 150$	Mode 1	-42.1582	0.0000	1.0000
	$D_2 = 200$	Mode 2	-19.1160	0.0000	1.0000
	$D_3 = 250$	Mode 3 Mode 4	-2.6152$\pm$ 5.0781i -6.0706	0.8082 0.0000	0.4579 1.0000

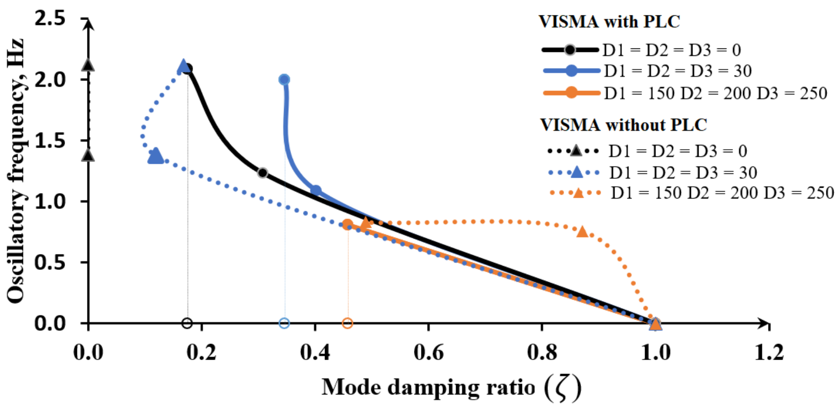

Figure 6.3. Impact of damping on system pole locations.

The stability condition is defined by the area bounded by each plot against the ζ axis. The smaller the area under the plot, the better is the system stability.

The plot of oscillatory frequency (f) versus damping ratio (ζ) of the system modes for each damping case is shown in Fig. 6.3 for both VISMA with outer loop power controller and that without external power controller. The region of attraction changes with the operating condition of the power system. From Fig. 6.3, it is obvious that VISMA with outer loop power controller is more stable compared to VISMA without outer loop controller for all the three damping cases considered. Taking damping case 1 (see Table 6.1) as an example for both control configurations, the $f - \zeta$ plot for VISMA with outer loop controller is completely along the oscillatory frequency axis, this means that the system will experience a sustained oscillation. For a similar case of VISMA with outer loop power controller, mode damping ratio exists and thus the system experiences underdamped characteristics and it is said to be stable. This example case is also validated by time domain simulation shown in Fig. 6.4. Under perturbed, stable conditions the instantaneous system frequency varies about the synchronously rotating speed reference $w_o = 1\,pu$ rad/sec of the system. As shown in Figure 6.4, the low frequency oscillations about the stationary point is more when VISMA is used without PLC (Fig. 6.4 a) than when it was used with PLC (Fig. 6.4 b).

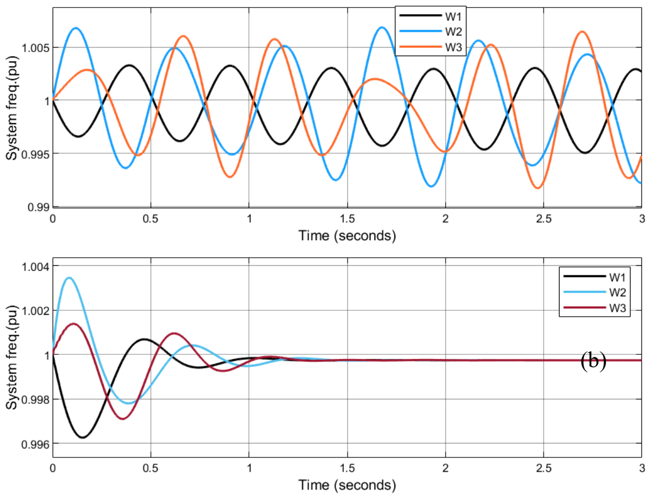

Figure 6.4. Impact of power loop controller on frequency stability (a) VISMA without PLC (b) VISMA with PLC.

6.4 Parameter sensitivities and participation factor in small signal stability analysis of *n*-VISMA Microgrid

Knowing that the stability of a dynamical system is often indicated by the real part of the system poles, only the real side of the sensitivity matrix has been studied. A specific damping case-3 (shown in the upper part of Fig. 6.5) has been considered for parameter sensitivity and PF analysis.

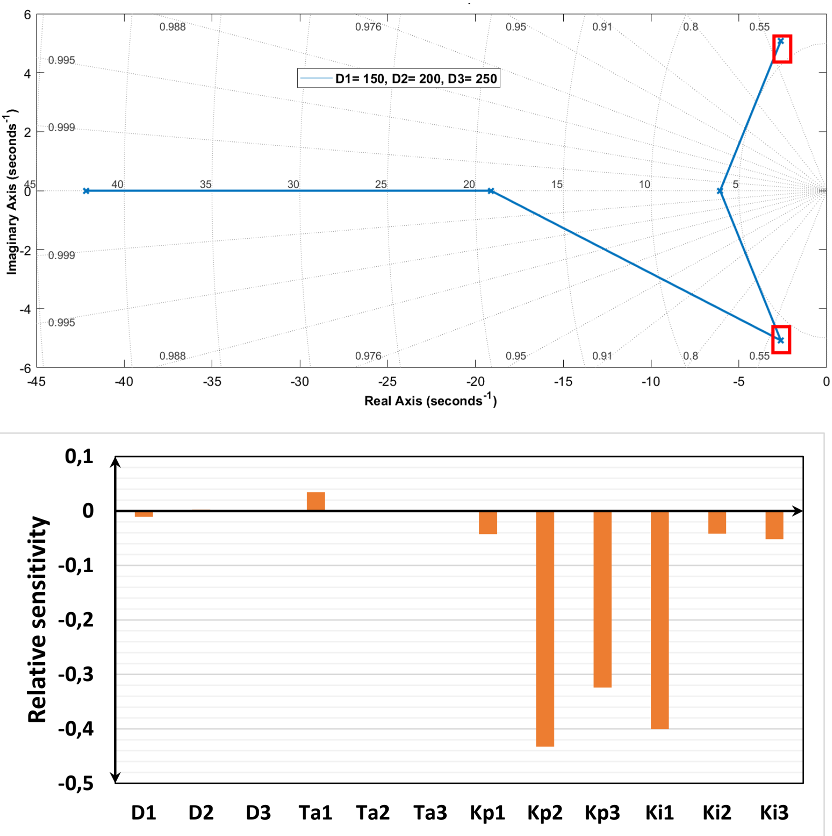

Figure 6. 5. Parameter sensitivity of the Dominant system pole (Case 3).

Fig. 6.5 illustrate sensitivities of case-3, mode-3. The mode is heavily impacted by k_{p2}, k_{p3}, k_{i1} and lightly impacted by $k_{i2}, k_{i3}, T_{a1}, D_{1,}T_{a2}$ and k_{p1}. The dynamic response of the microgrid can however be improved by reducing T_{a1} or increasing either of other stated parameters. The contribution of this pole to the transient response may be significant but is not severe as to induce instability in the system.

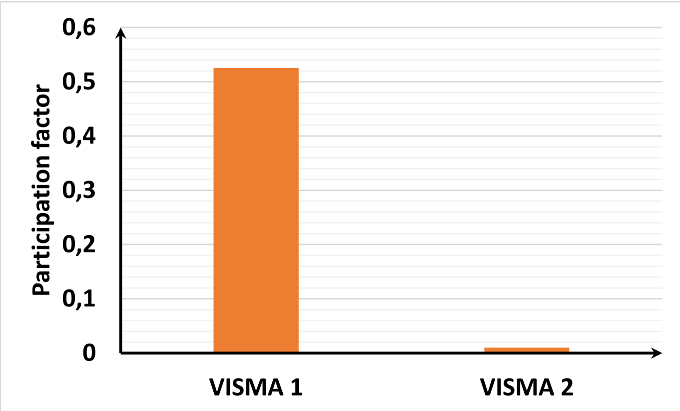

Figure 6.6. Degree of relative participation in rotor swinging due to the dominant mode.

Fig. 6.6 show the relative participation of VISMA1 and VISMA2 rotor angles with respect to VISMA3. Obviously, the swinging of the virtual rotor of VISMA 1 is highly heavy when compared with that of VISMA 2 rotor, thus, adjusting the local control parameters of VISMA 1 will play a significance role in improving the stability of the microgrid. Although, there are more heavily impacting parameters on the microgrid stability as shown in Fig. 6.5, I have rather decided to consider D_1 and T_{a1} to demonstrate the effect of their opposing actions on the microgrid dynamic performance. Fig. 6.7 (a) and Fig. 6.8 (a) respectively show the plot of inertia and Damping for VISMA 1 on the dominant mode while Fig. 6.7 (b) and Fig. 6.8 (b) demonstrate the eigenvalue movement on the PZ map. Due to the effect of reduced inertia on the general microgrid stability, it would be preferable to keep the machine inertia constant and increased its damping, since the resultant effect is to increase damping to inertia ratio. Increasing $\mathrm{D}_1/\mathrm{T}_1$ pushes the oscillatory mode away from the origin.

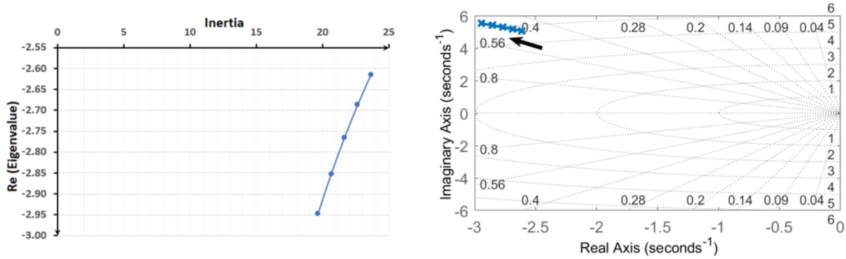

(a) (b)

Figure 6.7. Effect of reduced inertia on the dominant mode (a) Inertia Vs real (Eigenvalue) (b) eigenvalue trajectory

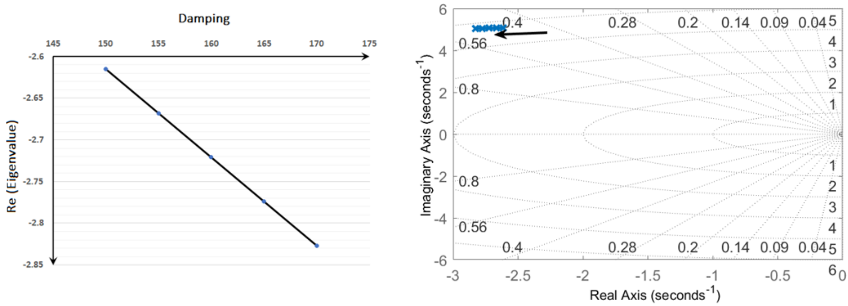

(a) (b)

Figure 6.8. Effect of increased damping on the oscillatory mode (a) Damping Vs real (Eigenvalue) (b) eigenvalue trajectory

6.5 Stability Limit

This is often used to define the maximum power that can be transmitted on the microgrid, under specified operating conditions in the steady state, without loss of synchronism. In order to study the steady stability of the investigated VISMA microgrid, disturbance is introduced in the form of linear increase/decrease in virtual torque input. VISMA 2 and VISMA 3 were made to operate in generator mode (i.e. positive slope) while VISMA1 was employed as a motor with negative input torque (i.e. negative slope). Ref. [188] reported that the disturbance should be slow and steady, as a result, the slow change in torque is accompanied by a slow adjustment of the rotor angles of the VISMAs without oscillation and thus VISMA is still able to keep the island frequency constant despite increasing governor set point. As shown in in Fig 6.9, instability sets in when VISMA is no longer able to balance the sum of the active power generated with the scheduled load power. Fig. 6.9 a and Fig 6.9 b respectively show the behaviour of active power and reactive power at the virtual buses, the three VISMAs loses synchronism at a different time. The results consolidate synthetic inertia to microgrid as the VISMA with the least synthetic inertia loses synchronism first (see Table 6.2).

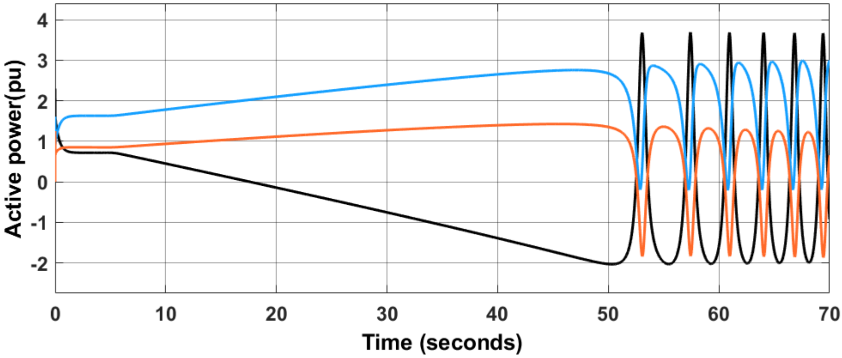

(a)

(b)

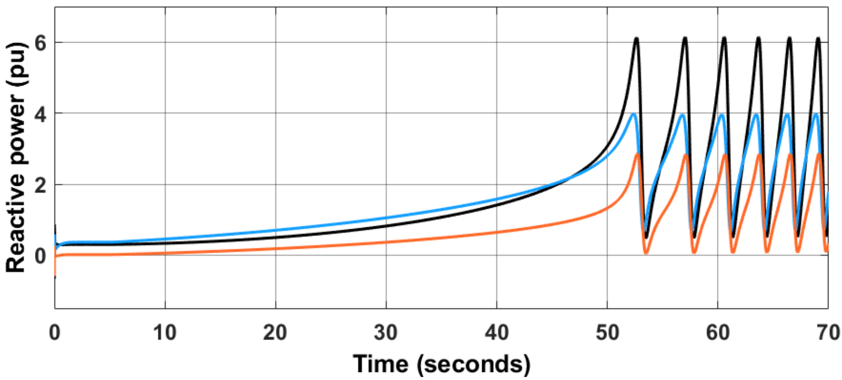

Fig. 6.9 c and 6.9 d respectively depict the corresponding behaviour of the relative rotor angle of the VISMAs and the voltage at the virtual buses.

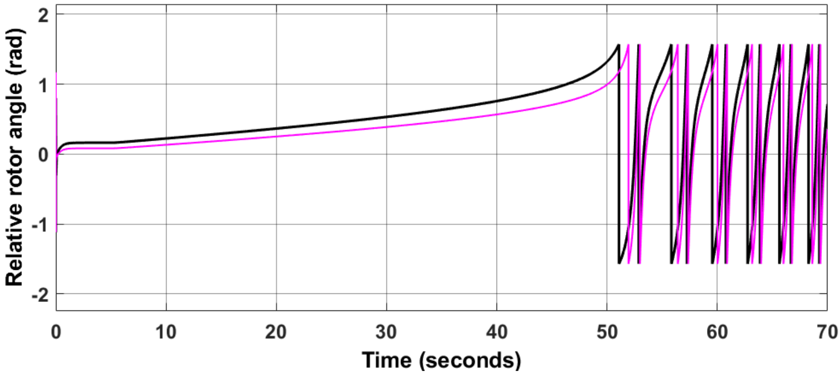

(c)

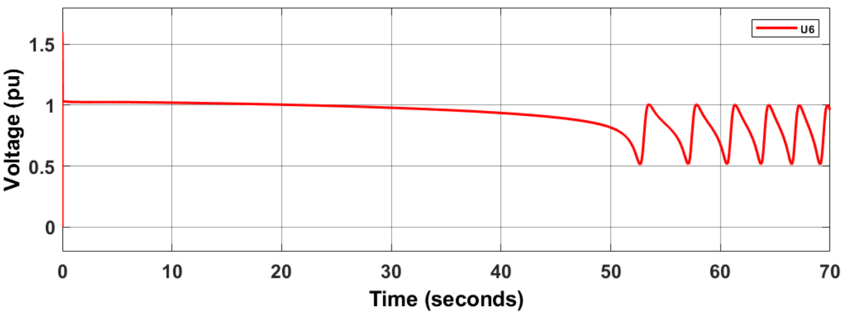

(d)

Figure 6.9. Stability limit (a) output power at virtual buses (b) reactive power at virtual buses (c) relative rotor angle (d) voltage at bus 6.

Table 6.2. Maximum operating points of the VISMAs

Power source	Operational Mode	Steady state active power (pu)	Maximum power limit (pu)	Time of losing synchronism (sec)	Inertia (sec)
VISMA 1	Motor	0.716	-2.021	50.343	23.64
VISMA 2	Generator	1.630	2.759	47.206	6.40
VISMA 3	Generator	0.850	1.432	45.049	3.01

** VISMA 3 acting as a dynamic load is varied from 0.716 to 2.5 pu

7. Conclusion and Outlook

7.1 Conclusion

The paradigm shifts in energy generation from the well-known synchronous machine to now inverter-based has been on the rise, this scenario helps to reduce energy import and enhances the nation's economy by fully internalising the possible expenditure on the external costs. In this work, the dynamic rotor angle stability of the simplified abc model type multi-VISMA model in autonomous mode of operation has been examined both with and without external power loop control. Since the rotor angle is directly related to the active power control, the effect of automatic voltage regulator (AVR) has been ignored in the stability analysis. Two categories of abc VISMA model exist; Voltage-Current VISMA model and Current-Voltage VISMA model. In this research work, only the former has been considered for analysis because of its less vulnerability to disturbance amplification when compared to the later. The stability analysis was preceded by an evaluation of stationary operating points of all dynamic nodes in the system using a new concept of virtual swing bus. The proposed concept employs the use of constant amplitude of virtual excitation and virtual torque localized to each VISMA for load flow formulation. The effectiveness of the proposed algorithm was tested on IEEE-9 bus 100%-VISMA microgrid (i.e. microgrid where all traditional synchronous machines are replaced with VISMA system) and a two VISMA low voltage system for both VISMA with inherent characteristic and VISMA with artificial droop control extension. Investigation reveals that the average absolute errors are quite higher for low voltage system compared to high voltage (i.e. IEEE-9 bus VISMA) system. The increased error in the low voltage (LV) system can be attributed to the resistive characteristic present in the network that tends to creates a coupling between the active and reactive power on the grid. Further findings from the algorithm investigation reveal that steady state operating points are independent of the virtual inertia but are rather dependent on the system damping. The frequency stability on the network also improves when local droop control is added externally to each VISMA system. Generally, the proposed method is simple to implement and computationally very effective but the effectiveness is wholesomely dependent on the level of coupling between the active and reactive power on the grid. This approach can thus be of immense benefit during planning and operation of 100% dominated VISMA microgrid. In the investigation of the rotor angle stability of 100% dominated VISMA microgrid to small disturbances, small-signal approach has been adopted. A linearized small-signal state-space model of the entire power system consisting of the basic VISMA control of the power electronic interface converter, network, and load have been formulated in Synchronously-rotating Reference Frame (SRF). Results reveal that the developed linearized small-signal model is sufficient to reliably characterize the behaviour of dynamic 100% VISMA microgrid when operated in autonomous mode. The small-signal model was further extended to investigate the dynamic stability condition of the VISMA microgrid incorporating an externally added decentralized control. Eigenvalues analysis for both control configurations reveals that system modes moved further away from the imaginary axis when outer power loop controller is added to the natural VISMA for all the three damping cases considered. At all-zero damping case for example, negative real part exists in the system modes (stable system) of the externally controlled VISMA as against uncontrolled VISMA where all modes are oscillatory (unstable system). Further analysis shows that under perturbed, stable conditions, the instantaneous system frequency varies about the synchronously rotating speed reference $w_o = 1\,pu$ of the system (i.e. around 5%) for uncontrolled VISMA configuration. But for VISMA with artificial control (i.e. PLC), the low frequency oscillations about the stationary point disappears due to the active damping characteristics introduced by the PLC. In the numerical time domain analysis using the concept of system matrix diagonalization by eigenvalues and eigenvectors, it was revealed that arbitrary increase in damping of VISMA to damp out oscillations has a limitation. The adjustment of damping should always be considered concurrently with the inertia of the same VISMA. If $\frac{D_i}{T_{ai}}$ (where $i = 1,2,3 \ldots$) is too large for a particular VISMA i, then, time taken for the VISMAs to synchronize after perturbation may be elongated which is not too palatable for system stability. The need for system inertia in the modern power grid was consolidated upon by the steady state stability limit study, where it was demonstrated that VISMA with the least synthetic inertia loses synchronism with the grid first. This action means that VISMA with higher inertia will tend to resist motion caused by power imbalance in the system. On the assessment of stability margin expressed in terms of load power increase from an operating point to the maximum power transfer (onset of instability), results show that IEEE-9 bus with 100% VISMA system has the ability to withstand at least 68% load increase before loss of synchronism. This operating point assessment however demonstrate that there is feasibility of operating multi-source power grids with 100% VISMA control and with such an assured small-signal stability.

7.2 Outlook

The followings are recommendations for future work on stability analysis of VISMA dominated microgrid;

1. Since small-signal stability problems are likely to be aggravated when the power system is 100% dominated by power electronics interfaced distributed energy sources, the problems of inertia are expected to be more pronounced, and as such multi-faceted approaches to enhance damping in a short period of time are required. One suggested approach to improve the small-signal stability is the appropriate tuning of the power system stabilizers.
2. Control implementation that enhances fault ride through capability of VISMA and transient stability analysis most especially during faults is highly recommended for investigation.
3. Development of control strategies that allows self-synchronized operation of VISMA to completely eliminate the nonlinear effects of PLL is recommended.
4. The virtual swing bus algorithm could be improved upon to reduce the errors associated with low voltage system. The possible idea is to formulate the mathematical model such that the resistance of the virtual stator impedance is retained instead of assuming that the virtual stator is purely inductive.
5. The use of Vehicle to grid (V2G) is one of the newest strategic way to control grid frequency (both primary and secondary frequency control) especially during peak period. This research aims to combine the technology of both VISMA control and electric vehicles (EVs) technologies to achieving dynamic stability, grid resiliency and energy efficiency of the power system.

References

[1] REA. (2022, 02.03.2024). *Key Facts about the Energy Transition in Germany*. Available: https://www.energydialogue.berlin/app/uploads/2022/03/betd_factsheet_2022.pdf

[2] Bundesnetzagentur. (2024, 02.02.2024). *Growth in renewable energy in 2023*. Available: https://publications.iass-potsdam.de/rest/items/item_1478144_9/component/file_1504190/content

[3] Bundesnetzagentur. (2024, 01.09.2024). *Statistiken ausgewählter erneuerbarer Energieträger zur Stromerzeugung* Available: https://www.bundesnetzagentur.de/SharedDocs/Downloads/DE/Sachgebiete/Energie/Unternehmen_Institutionen/ErneuerbareEnergien/ZahlenDatenInformationen/EEStatistikMaStR.pdf?__blob=publicationFile&v=13

[4] R. Hesse, D. Turschner, and H.-P. Beck, "Micro grid stabilization using the virtual synchronous machine (VISMA)," in *Proceedings of the International Conference on Renewable Energies and Power Quality (ICREPQ'09), Valencia, Spain*, 2009, pp. 15-17.

[5] F. Izuegbunam, O. Nduka, H. Nwaichi, and K. Oguanya, "Simulink Simulation of Synchronous Generator Load Angle Estimation via Linearized Rotor Dynamic Equation," *International Journal of Applied Engineering Research,* vol. 6, pp. 1411-1424, 2011.

[6] X. Meng, J. Liu, and Z. Liu, "A generalized droop control for grid-supporting inverter based on comparison between traditional droop control and virtual synchronous generator control," *IEEE Transactions on Power Electronics,* vol. 34, pp. 5416-5438, 2018.

[7] R. Lalwani, R. Sahu, V. Kumar, B. Tyagi, and R. K. Calay, "Optimal Droop Control for Current Sharing among Different Types of Battery Energy Storage Systems," in *2024 Third International Conference on Power, Control and Computing Technologies (ICPC2T)*, 2024, pp. 715-720.

[8] A. Kannan, M. Nuschke, and D. Strau-Mincu, "LFC model for frequency stability analysis of prospective power systems with high shares of inverter based generation," in *2019 IEEE Milan PowerTech*, 2019, pp. 1-6.

[9] Y. Sun, E. De Jong, X. Wang, D. Yang, F. Blaabjerg, V. Cuk*, et al.*, "The impact of PLL dynamics on the low inertia power grid: A case study of Bonaire Island power system," *Energies,* vol. 12, p. 1259, 2019.

[10] J. Xiao, Y. Jia, B. Jia, Z. Li, Y. Pan, and Y. Wang, "An inertial droop control based on comparisons between virtual synchronous generator and droop control in inverter-based distributed generators," *Energy Reports,* vol. 6, pp. 104-112, 2020.

[11] B. Burger. (2024, 11.03.2024). *Electricity generation in Germany in 2023*. Available: https://www.energy-charts.info/downloads/electricity_generation_germany_2023.pdf

[12] A. Robb. (2019, 25.08.2021). *Grid inertia: why it matters in a renewable world*. Available: https://www.renewableenergyworld.com/baseload/grid-inertia-why-it-matters-in-a-renewable-world/

[13] O. Mohammed, A. Otuoze, S. Salisu, O. Ibrahim, and N. Rufa'i, "Virtual synchronous generator: an overview," *Nigerian Journal of Technology,* vol. 38, pp. 153-164, 2019.

[14] AEMO, "Power system requirements," ed. Australian Energy Market Operator, Melbourne, Australia, 2020, p. 23.

[15] A. Sajadi, R. W. Kenyon, and B.-M. Hodge, "Synchronization in electric power networks with inherent heterogeneity up to 100% inverter-based renewable generation," *Nature communications,* vol. 13, p. 2490, 2022.

[16] H. Bevrani, "Robust power system frequency control," 2014.

[17] H.-P. Beck and R. Hesse, "Virtual synchronous machine," in *2007 9th International Conference on Electrical Power Quality and Utilisation*, 2007, pp. 1-6.

[18] Y. Chen, "Virtuelle Synchronmaschine (VISMA) zur Erbringung von Systemdienstleistungen in verschiedenen Netzbetriebsarten," PhD, Institute of Electrical Power Engineering, TU Clausthal-Zellerfeld, Germany, 2016.

[19] P. Kundur, J. Paserba, V. Ajjarapu, G. Andersson, A. Bose, C. Canizares*, et al.*, "Definition and classification of power system stability IEEE/CIGRE joint task force on stability terms and definitions," *IEEE transactions on Power Systems,* vol. 19, pp. 1387-1401, 2004.

[20] Y. Chen, R. Hesse, D. Turschner, and H.-P. Beck, "Comparison of methods for implementing virtual synchronous machine on inverters," in *International conference on renewable energies and power quality*, 2012, pp. 414-424.

[21] S. D'Arco, J. A. Suul, and O. B. Fosso, "Control system tuning and stability analysis of virtual synchronous machines," in *2013 IEEE Energy Conversion Congress and Exposition*, 2013, pp. 2664-2671.

[22] Q.-C. Zhong and G. Weiss, "Synchronverters: Inverters that mimic synchronous generators," *IEEE transactions on industrial electronics,* vol. 58, pp. 1259-1267, 2010.

[23] M. Blau and G. Weiss, "Synchronverters used for damping inter-area oscillations in two-area power systems," in *Int. Conf. on Renew. Energies and Power Quality (ICREPQ)*, 2018.

[24] K. Sakimoto, Y. Miura, and T. Ise, "Stabilization of a power system with a distributed generator by a virtual synchronous generator function," in *8th International Conference on Power Electronics-ECCE Asia*, 2011, pp. 1498-1505.

[25] P. Rodriguez, I. Candela, J. Rocabert, and R. Teodorescu, "United States Patent Application Publication: Synchronous power controller for a generating system based on static power converters," *US,* vol. 49228, p. A1, 2014.

[26] D. Gautam, V. Vittal, and T. Harbour, "Impact of increased penetration of DFIG-based wind turbine generators on transient and small signal stability of power systems," *IEEE Transactions on power systems,* vol. 24, pp. 1426-1434, 2009.

[27] A. Monti, F. Milano, E. Bompard, and X. Guillaud, *Converter-based dynamics and control of modern power systems*: Academic Press, 2020.

[28] A. E. Motter, S. A. Myers, M. Anghel, and T. Nishikawa, "Spontaneous synchrony in power-grid networks," *Nature Physics,* vol. 9, pp. 191-197, 2013.

[29] V. Mallemaci, F. Mandrile, S. Rubino, A. Mazza, E. Carpaneto, and R. Bojoi, "A comprehensive comparison of Virtual Synchronous Generators with focus on virtual inertia and frequency regulation," *Electric Power Systems Research,* vol. 201, p. 107516, 2021.

[30] J. Liu, Y. Miura, and T. Ise, "Dynamic characteristics and stability comparisons between virtual synchronous generator and droop control in inverter-based distributed generators," in *2014 International Power Electronics Conference (IPEC-Hiroshima 2014-ECCE ASIA)*, 2014, pp. 1536-1543.

[31] J. Liu, Y. Miura, and T. Ise, "Comparison of dynamic characteristics between virtual synchronous generator and droop control in inverter-based distributed generators," *IEEE Transactions on Power Electronics,* vol. 31, pp. 3600-3611, 2015.

[32] T. Kerdphol, M. Watanabe, Y. Mitani, D. Turschner, and H.-P. Beck, "Stability Assessment of Multiple Virtual Synchronous Machines for Microgrid Frequency Stabilization," in *2020 IEEE Power & Energy Society General Meeting (PESGM)*, 2020, pp. 1-5.

[33] T. Kerdphol, F. S. Rahman, M. Watanabe, Y. Mitani, K. Hongesombut, V. Phunpeng*, et al.*, "Small-signal analysis of multiple virtual synchronous machines to enhance frequency stability of grid-connected high renewables," *IET Generation, Transmission & Distribution,* vol. 15, pp. 1273-1289, 2021.

[34] S. D'Arco, J. A. Suul, and O. B. Fosso, "Automatic tuning of cascaded controllers for power converters using eigenvalue parametric sensitivities," *IEEE Transactions on Industry Applications,* vol. 51, pp. 1743-1753, 2014.

[35] S. D’Arco, J. A. Suul, and O. B. Fosso, "Small-signal modeling and parametric sensitivity of a virtual synchronous machine in islanded operation," *International Journal of Electrical Power & Energy Systems,* vol. 72, pp. 3-15, 2015.

[36] F. Blaabjerg, R. Teodorescu, M. Liserre, and A. V. Timbus, "Overview of control and grid synchronization for distributed power generation systems," *IEEE Transactions on industrial electronics,* vol. 53, pp. 1398-1409, 2006.

[37] J. Saleem. (2023). *Grid Forming vs Grid Following*. Available: https://energycentral.com/c/iu/grid-forming-vs-grid-following

[38] Z. Yang, M. Zhan, D. Liu, C. Ye, K. Cao, and S. Cheng, "Small-signal synchronous stability of a new-generation power system with 100% renewable energy," *IEEE Transactions on Power Systems,* 2023.

[39] J. D. Glover, M. S. Sarma, and T. Overbye, *Power system analysis & design, SI version*: Cengage Learning, 2012.

[40] P. Kundur, "Power system stability," *Power system stability and control,* pp. 7-1, 2007.

[41] U. Tamrakar, D. Shrestha, M. Maharjan, B. P. Bhattarai, T. M. Hansen, and R. Tonkoski, "Virtual inertia: Current trends and future directions," *Applied sciences,* vol. 7, p. 654, 2017.

[42] V. Vittal, J. D. McCalley, P. M. Anderson, and A. Fouad, *Power system control and stability*: John Wiley & Sons, 2019.

[43] P. Rodriguez, I. Candela, and A. Luna, "Control of PV generation systems using the synchronous power controller," in *2013 IEEE Energy Conversion Congress and Exposition*, 2013, pp. 993-998.

[44] W. Sang, W. Guo, S. Dai, C. Tian, S. Yu, and Y. Teng, "Virtual synchronous generator, a comprehensive overview," *Energies,* vol. 15, p. 6148, 2022.

[45] F. Blaabjerg, *Control of Power Electronic Converters and Systems: Volume 2* vol. 2: Academic Press, 2018.

[46] F. Jenni and D. Wüest, *Steuerverfahren für selbstgeführte Stromrichter*: vdf Hochschulverlag AG, 1995.

[47] T. Nguyen-Van, R. Abe, and K. Tanaka, "Digital adaptive hysteresis current control for multi-functional inverters," *Energies,* vol. 11, p. 2422, 2018.

[48] Guosong Lin and H.-P. Beck, "Stability analysis of inverter networks with virtual synchronous machine function (VISMA) ", G. Clausthal University of Technology, Ed., unpublished research work ed, 2021.

[49] Y. Chen, R. Hesse, D. Turschner, and H.-P. Beck, "Investigation of the virtual synchronous machine in the island mode," in *2012 3rd IEEE PES Innovative Smart Grid Technologies Europe (ISGT Europe)*, 2012, pp. 1-6.

[50] O. W. Paul C. Kraus, Scott D. Sudhoff, *Analysis of Electric Machinery and Drive Systems*, third ed. Hoboken, New Jersey: John Wiley & Sons, Inc., 2013.

[51] F. Milano and Á. O. Manjavacas, *Converter-interfaced energy storage systems: Context, modelling and dynamic analysis*: Cambridge University Press, 2019.

[52] L. Wang, S. Chai, D. Yoo, L. Gan, and K. Ng, *PID and predictive control of electrical drives and power converters using MATLAB/Simulink*: John Wiley & Sons, 2015.

[53] M. J. Gibbard, P. Pourbeik, and D. J. Vowles, *Small-signal stability, control and dynamic performance of power systems*: University of Adelaide press, 2015.

[54] J. Machowski, Z. Lubosny, J. W. Bialek, and J. R. Bumby, *Power system dynamics: stability and control*: John Wiley & Sons, 2020.

[55] D. Abakar, A. Abouelsoud, M. J. Saulo, and S. S. Sitati, "Improving Rotor Angle Stability of the Multimachine Power System Using Constrained Optimal Control," in *15th European Workshop on Advanced Control and Diagnosis*, 2018, pp. 491-509.

[56] D. Mondal, A. Chakrabarti, and A. Sengupta, *Power system small signal stability analysis and control*: Academic Press, 2020.

[57] J. H. Chow and J. J. Sanchez-Gasca, *Power system modeling, computation, and control*: John Wiley & Sons, 2020.

[58] V. O. Kostiuk and T. O. Kostyuk, "Power System Steady-state Stability Criteria and the Jacobian of Dynamical Systems," in *IEEE EUROCON 2021-19th International Conference on Smart Technologies*, 2021, pp. 523-530.

[59] T. Qoria, Q. Cossart, C. Li, X. Guillaud, F. Colas, F. Gruson*, et al.*, "WP3–Control and Operation of a Grid with 100% Converter-Based Devices. Deliverable 3.2: Local control and simulation tools for large transmission systems," *MIGRATE Project,* 2018.

[60] H. Bevrani, B. François, and T. Ise, *Microgrid dynamics and control*: John Wiley & Sons, 2017.

[61] A. Yazdani and R. Iravani, *Voltage-sourced converters in power systems: modeling, control, and applications*: John Wiley & Sons, 2010.

[62] J. Liu, Y. Miura, H. Bevrani, and T. Ise, "Enhanced virtual synchronous generator control for parallel inverters in microgrids," *IEEE Transactions on Smart Grid,* vol. 8, pp. 2268-2277, 2016.

[63] J. Liu, "Studies on improving dynamic performance of microgrids by applying virtual synchronous generator control to distributed generators," *Osaka University,* 2016.

[64] M. Baruwa, "Design and Control of Virtual Synchronous Machine Based Energy Systems," 2021.

[65] Q.-C. Zhong and G. Weiss, "Static synchronous generators for distributed generation and renewable energy," in *2009 IEEE/PES Power Systems Conference and Exposition*, 2009, pp. 1-6.

[66] M. Van Wesenbeeck, S. De Haan, P. Varela, and K. Visscher, "Grid tied converter with virtual kinetic storage," in *2009 IEEE Bucharest PowerTech*, 2009, pp. 1-7.

[67] V. Karapanos, Z. Yuan, S. De Haan, and K. Visscher, "A control algorithm for the coordination of multiple virtual synchronous generator units," in *Proceedings of the IEEE Powertech conference, June*, 2011, pp. 19-23.

[68] Y. Hirase, K. Abe, K. Sugimoto, and Y. Shindo, "A grid-connected inverter with virtual synchronous generator model of algebraic type," *Electrical Engineering in Japan,* vol. 184, pp. 10-21, 2013.

[69] Y. Hirase, K. Sugimoto, K. Sakimoto, and T. Ise, "Analysis of resonance in microgrids and effects of system frequency stabilization using a virtual synchronous generator," *IEEE Journal of Emerging and Selected Topics in Power Electronics,* vol. 4, pp. 1287-1298, 2016.

[70] H. Bevrani, T. Ise, and Y. Miura, "Virtual synchronous generators: A survey and new perspectives," *International Journal of Electrical Power & Energy Systems,* vol. 54, pp. 244-254, 2014.

[71] M. Shadoul, R. Ahshan, R. S. AlAbri, A. Al-Badi, M. Albadi, and M. Jamil, "A comprehensive review on a virtual-synchronous generator: Topologies, control orders and techniques, energy storages, and applications," *Energies,* vol. 15, p. 8406, 2022.

[72] M. Abuagreb, M. F. Allehyani, and B. K. Johnson, "Overview of virtual synchronous generators: existing projects, challenges, and future trends," *Electronics,* vol. 11, p. 2843, 2022.

[73] P. R. CORTÉS, J. I. C. García, J. R. Delgado, and R. Teodorescu, "Virtual controller of electromechanical characteristics for static power converters," ed: Google Patents, 2014.

[74] W. Zhang, A. Luna, I. Candela, J. Rocabert, and P. Rodriguez, "An active power synchronizing controller for grid-connected power converters with configurable natural droop characteristics," in *2015 IEEE 6th International Symposium on Power Electronics for Distributed Generation Systems (PEDG)*, 2015, pp. 1-7.

[75] K. S. Ratnam, K. Palanisamy, and G. Yang, "Future low-inertia power systems: Requirements, issues, and solutions-A review," *Renewable and Sustainable Energy Reviews,* vol. 124, p. 109773, 2020.

[76] C. Verdugo, J. I. Candela, and P. Rodriguez, "Re-synchronization strategy for the synchronous power controller in hvdc systems," in *2017 IEEE Energy Conversion Congress and Exposition (ECCE)*, 2017, pp. 5186-5191.

[77] W. Zhang, D. Remon, A. Mir, A. Luna, J. Rocabert, I. Candela*, et al.*, "Comparison of different power loop controllers for synchronous power controlled grid-interactive converters," in *2015 IEEE energy conversion congress and exposition (ECCE)*, 2015, pp. 3780-3787.

[78] M. Ashabani, F. D. Freijedo, S. Golestan, and J. M. Guerrero, "Inducverters: PLL-less converters with auto-synchronization and emulated inertia capability," *IEEE Transactions on Smart Grid,* vol. 7, pp. 1660-1674, 2015.

[79] K. Sakimoto, K. Sugimoto, Y. Shindo, and T. Ise, "Virtual synchronous generator without phase locked loop based on current controlled inverter and its parameter design," *IEEJ Transactions on Power and Energy,* vol. 135, pp. 462-471, 2015.

[80] R. F. Idan, A. J. Mahdi, and T. M. Abdul Wahhab, "Review on Virtual Inertia Control Topologies for Improving Frequency Stability of Microgrid," *Engineering and Technology Journal,* vol. 41, pp. 345-358, 2023.

[81] G. P. da Silva Júnior, T. F. do Nascimento, and L. S. Barros, "Comparison of virtual synchronous generator strategies for control of distributed energy sources and power system stability improvement," *Simpósio Brasileiro de Sistemas Elétricos-SBSE,* vol. 1, 2020.

[82] W. Yao, M. Chen, J. Matas, J. M. Guerrero, and Z.-M. Qian, "Design and analysis of the droop control method for parallel inverters considering the impact of the complex impedance on the power sharing," *IEEE Transactions on Industrial Electronics,* vol. 58, pp. 576-588, 2010.

[83] J. Liu, M. Yushi, T. Ise, J. Yoshizawa, and K. Watanabe, "Parallel operation of a synchronous generator and a virtual synchronous generator under unbalanced loading condition in microgrids," in *2016 IEEE 8th International Power Electronics and Motion Control Conference (IPEMC-ECCE Asia)*, 2016, pp. 3741-3748.

[84] A. Jaber, M. Yushi, and I. Toshifumi, "Evaluation of virtual synchronous generator (VSG) operation under different voltage sag conditions," *電気学会研究会資料. PSE, 電力系統技術研究会,* vol. 2012, pp. 41-46, 2012.

[85] T. Shintai, Y. Miura, and T. Ise, "Reactive power control for load sharing with virtual synchronous generator control," in *Proceedings of The 7th International Power Electronics and Motion Control Conference*, 2012, pp. 846-853.

[86] J. Liu, Y. Miura, and T. Ise, "Fixed-parameter damping methods of virtual synchronous generator control using state feedback," *IEEE Access,* vol. 7, pp. 99177-99190, 2019.

[87] J. Alipoor, Y. Miura, and T. Ise, "Power system stabilization using virtual synchronous generator with alternating moment of inertia," *IEEE journal of Emerging and selected topics in power electronics,* vol. 3, pp. 451-458, 2015.

[88] L. Huang, H. Xin, W. Dong, and F. Dörfler, "Impacts of grid structure on PLL-synchronization stability of converter-integrated power systems," *IFAC-PapersOnLine,* vol. 55, pp. 264-269, 2022.

[89] O. Stanojev, U. Markovic, P. Aristidou, and G. Hug, "Improving stability of low-inertia systems using virtual induction machine synchronization for grid-following converters," *IEEE Transactions on Power Systems,* vol. 38, pp. 2290-2303, 2023.

[90] W.-L. Ming and Q.-C. Zhong, "Synchronverter-based transformerless PV inverters," in *IECON 2014-40th Annual Conference of the IEEE Industrial Electronics Society*, 2014, pp. 4396-4401.

[91] R. Aouini, B. Marinescu, K. B. Kilani, and M. Elleuch, "Synchronverter-based emulation and control of HVDC transmission," *IEEE Transactions on Power Systems,* vol. 31, pp. 278-286, 2015.

[92] R. Aouini, B. Marinescu, K. B. Kilani, and M. Elleuch, "Interconnection of two very weak AC systems by synchronverter based HVDC," in *2nd International Conference on Automation, Control, Engineering and Computer Science (ACECS-2015) Proceedings of Engineering & Technology (PET)*, 2015.

[93] R. Aouini, I. Nefzi, K. B. Kilani, and M. Elleuch, "Exploitation of synchronverter control to improve the integration of renewable sources to the grid," *J. Electr. Syst,* vol. 13, pp. 543-557, 2017.

[94] P.-L. Nguyen, Q.-C. Zhong, F. Blaabjerg, and J. M. Guerrero, "Synchronverter-based operation of STATCOM to mimic synchronous condensers," in *2012 7th IEEE conference on industrial electronics and applications (ICIEA)*, 2012, pp. 942-947.

[95] L. do Nascimento Gomes, A. J. G. Abrantes-Ferreira, R. F. da Silva Dias, and L. G. B. Rolim, "Synchronverter-based statcom with voltage imbalance compensation functionality," *IEEE Transactions on Industrial Electronics,* vol. 69, pp. 4836-4844, 2021.

[96] A. J. Sonawane and A. C. Umarikar, "Voltage and Reactive Power Regulation with Synchronverter-Based Control of PV-STATCOM," *IEEE Access,* 2023.

[97] Q.-C. Zhong, P.-L. Nguyen, Z. Ma, and W. Sheng, "Self-synchronized synchronverters: Inverters without a dedicated synchronization unit," *IEEE Transactions on power electronics,* vol. 29, pp. 617-630, 2013.

[98] K. R. Vasudevan, V. K. Ramachandaramurthy, T. S. Babu, and A. Pouryekta, "Synchronverter: A comprehensive review of modifications, stability assessment, applications and future perspectives," *IEEE Access,* vol. 8, pp. 131565-131589, 2020.

[99] L. Lu and N. A. Cutululis, "Virtual synchronous machine control for wind turbines: A review," in *Journal of Physics: Conference Series*, 2019, p. 012028.

[100] V. Natarajan and G. Weiss, "Synchronverters with better stability due to virtual inductors, virtual capacitors, and anti-windup," *IEEE Transactions on Industrial Electronics,* vol. 64, pp. 5994-6004, 2017.

[101] P. Piya and M. Karimi-Ghartemani, "A stability analysis and efficiency improvement of synchronverter," in *2016 IEEE Applied Power Electronics Conference and Exposition (APEC)*, 2016, pp. 3165-3171.

[102] R. Rosso, S. Engelken, and M. Liserre, "Robust stability analysis of synchronverters operating in parallel," *IEEE Transactions on Power Electronics,* vol. 34, pp. 11309-11319, 2019.

[103] G. Weiss and V. Natarajan, "Modifications to the synchronverter algorithm to improve its stability and performance," in *2017 International Symposium on Power Electronics (Ee)*, 2017, pp. 1-6.

[104] R. Hariharan and M. K. Mishra, "An Improved Synchronverter Control for DERs Under Grid Voltage Variations," in *2021 IEEE 2nd International Conference on Smart Technologies for Power, Energy and Control (STPEC)*, 2021, pp. 1-6.

[105] B. W. França, M. Aredes, L. F. da Silva, G. F. Gontijo, T. C. Tricarico, and J. Posada, "An enhanced shunt active filter based on synchronverter concept," *IEEE Journal of Emerging and Selected Topics in Power Electronics,* vol. 10, pp. 494-505, 2021.

[106] S. D'Arco, J. A. Suul, and O. B. Fosso, "A Virtual Synchronous Machine implementation for distributed control of power converters in SmartGrids," *Electric Power Systems Research,* vol. 122, pp. 180-197, 2015.

[107] M. Ashabani, A.-R. M. Yasser, M. Mirsalim, and M. Aghashabani, "Multivariable droop control of synchronous current converters in weak grids/microgrids with decoupled dq-axes currents," *IEEE Transactions on Smart Grid,* vol. 6, pp. 1610-1620, 2015.

[108] W. Zhang, A. M. Cantarellas, J. Rocabert, A. Luna, and P. Rodriguez, "Synchronous power controller with flexible droop characteristics for renewable power generation systems," *IEEE Transactions on Sustainable Energy,* vol. 7, pp. 1572-1582, 2016.

[109] W. Zhang, A. Tarraso, J. Rocabert, A. Luna, J. I. Candela, and P. Rodriguez, "Frequency support properties of the synchronous power control for grid-connected converters," *IEEE Transactions on Industry Applications,* vol. 55, pp. 5178-5189, 2019.

[110] W. Zhang, D. Remon, and P. Rodriguez, "Frequency support characteristics of grid-interactive power converters based on the synchronous power controller," *IET Renewable Power Generation,* vol. 11, pp. 470-479, 2017.

[111] N. U. Padmawansa and L. N. W. Arachchige, "Improving Transient Stability of an Islanded Microgrid Using PV Based Virtual Synchronous Machines," in *2020 Moratuwa Engineering Research Conference (MERCon)*, 2020, pp. 543-548.

[112] S. Wang and L. Shang, "Fault ride through strategy of virtual-synchronous-controlled DFIG-based wind turbines under symmetrical grid faults," *IEEE Transactions on Energy Conversion,* vol. 35, pp. 1360-1371, 2020.

[113] Y. Hirase, O. Noro, E. Yoshimura, H. Nakagawa, K. Sakimoto, and Y. Shindo, "Virtual synchronous generator control with double decoupled synchronous reference frame for single-phase inverter," *IEEJ Journal of Industry Applications,* vol. 4, pp. 143-151, 2015.

[114] C. Zhong, Z. Zhang, A. Zhu, and B. Liang, "An Adaptive Virtual Impedance Method for Grid-Connected Current Quality Improvement of a Single-Phase Virtual Synchronous Generator under Distorted Grid Voltage," *Sensors,* vol. 23, p. 6857, 2023.

[115] H. Wu, X. Ruan, D. Yang, X. Chen, W. Zhao, Z. Lv*, et al.*, "Small-signal modeling and parameters design for virtual synchronous generators," *IEEE Transactions on Industrial Electronics,* vol. 63, pp. 4292-4303, 2016.

[116] Y. Hirase, K. Abe, K. Sugimoto, K. Sakimoto, H. Bevrani, and T. Ise, "A novel control approach for virtual synchronous generators to suppress frequency and voltage fluctuations in microgrids," *Applied Energy,* vol. 210, pp. 699-710, 2018.

[117] K.-i. Sakimoto, K. Sugimoto, and Y. Shindo, "Low voltage ride through capability of a grid connected inverter based on the virtual synchronous generator," in *2013 IEEE 10th International Conference on Power Electronics and Drive Systems (PEDS)*, 2013, pp. 1066-1071.

[118] S. Reineke, D. Turschner, I. Hauer, and H.-P. Beck, "Verification of the uninterrupted transition from grid parallel to island grid operation of the Virtual Synchronous Machine in a microgrid," in *21th International Conference on Renewable Energies and Power Quality (ICREPQ'23)*, 2023.

[119] S. M. Ashabani and Y. A.-R. I. Mohamed, "A flexible control strategy for grid-connected and islanded microgrids with enhanced stability using nonlinear microgrid stabilizer," *IEEE Transactions on Smart Grid,* vol. 3, pp. 1291-1301, 2012.

[120] Z. Shuai, W. Huang, C. Shen, J. Ge, and Z. J. Shen, "Characteristics and restraining method of fast transient inrush fault currents in synchronverters," *IEEE Transactions on Industrial Electronics,* vol. 64, pp. 7487-7497, 2017.

[121] Y. Zhang, S. Wu, P. Yang, S. Xiang, S. Li, and S. He, "Research on parallel operation of virtual synchronous generators in microgrid," in *2019 14th IEEE Conference on Industrial Electronics and Applications (ICIEA)*, 2019, pp. 1659-1664.

[122] D. Remon, A. M. Cantarellas, J. Martinez-Garcia, J. M. Escaño, and P. Rodriguez, "Hybrid solar plant with synchronous power controllers contribution to power system stability," in *2017 IEEE Energy Conversion Congress and Exposition (ECCE)*, 2017, pp. 4069-4076.

[123] L. Zhang, L. Harnefors, and H.-P. Nee, "Interconnection of two very weak AC systems by VSC-HVDC links using power-synchronization control," *IEEE transactions on power systems,* vol. 26, pp. 344-355, 2010.

[124] S. D'Arco, G. Guidi, and J. A. Suul, "Embedded limitations and protections for droop-based control schemes with cascaded loops in the synchronous reference frame," in *2014 International Power Electronics Conference (IPEC-Hiroshima 2014-ECCE ASIA)*, 2014, pp. 1544-1551.

[125] P. Shah and B. Singh, "Self-synchronising virtual induction generator without phase-locked loop and proportional–integral regulators," *IET Generation, Transmission & Distribution,* vol. 14, pp. 5080-5092, 2020.

[126] M. Cheah-Mane, A. Egea-Alvarez, E. Prieto-Araujo, H. Mehrjerdi, O. Gomis-Bellmunt, and L. Xu, "Modeling and analysis approaches for small-signal stability assessment of power-electronic-dominated systems," *Wiley Interdisciplinary Reviews: Energy and Environment,* vol. 12, p. e453, 2023.

[127] J. H. Chow, *Power system coherency and model reduction* vol. 84: Springer, 2013.

[128] M. Kouki, B. Marinescu, and F. Xavier, "Exhaustive modal analysis of large-scale interconnected power systems with high power electronics penetration," *IEEE Transactions on Power Systems,* vol. 35, pp. 2759-2768, 2020.

[129] N. E. Costa, G. Revel, D. M. Alonso, and R. D. Fernández, "Subsynchronous control interaction studies in DFIG-based wind farms using selective modal analysis," *International Journal of Electrical Power & Energy Systems,* vol. 123, p. 106291, 2020.

[130] C. Collados-Rodriguez, M. Cheah-Mane, E. Prieto-Araujo, and O. Gomis-Bellmunt, "Stability analysis of systems with high VSC penetration: Where is the limit?," *IEEE Transactions on Power Delivery,* vol. 35, pp. 2021-2031, 2019.

[131] P. S. Kundur and O. P. Malik, *Power system stability and control*: McGraw-Hill Education, 2022.

[132] O. D. Fernández, A. Gusrialdi, A. A. M. García, M. V. Llanes, and O. E. T. Breffe, "Angular stability analysis of a multimachine system with distributed and large-scale photovoltaic generations," in *2021 IEEE PES Innovative Smart Grid Technologies Europe (ISGT Europe)*, 2021, pp. 01-05.

[133] M. Vidyasagar, *Nonlinear systems analysis*: SIAM, 2002.

[134] J. D. Hedengren, "Dynamis and control: Linearization of Differential Equations," ed, 2021.

[135] G. Barbastathis, D. C. Gossard, and F. S. Hofer. (2007, 08.09.2024). *Linearization in dynamical systems*. Available: https://www.flickr.com/photos/mitopencourseware/3028258388

[136] T. He, S. Li, S. Wu, and K. Li, "Small-signal stability analysis for power system frequency regulation with renewable energy participation," *Mathematical Problems in Engineering,* vol. 2021, pp. 1-13, 2021.

[137] J. Ritonja and B. Polajžer, "Analysis of synchronous generators' local mode eigenvalues in modern power systems," *Applied Sciences,* vol. 12, p. 195, 2022.

[138] V. Konoval and R. Prytula, "Participation factor in modal analysis of power systems stability," *Poznan University of Technology Academic Journals. Electrical Engineering,* 2016.

[139] F. Dussaud, "An application of modal analysis in electric power systems to study inter-area oscillations," ed, 2015.

[140] O. Katsuhiko, "Modern control engineering," 2010.

[141] L. Rouco and F. Pagola, "Eigenvalue sensitivities for design of power system damping controllers," in *Proceedings of the 40th IEEE Conference on Decision and Control (Cat. No. 01CH37228)*, 2001, pp. 3051-3055.

[142] P. W. Sauer, M. A. Pai, and J. H. Chow, *Power system dynamics and stability: with synchrophasor measurement and power system toolbox*: John Wiley & Sons, 2017.

[143] F. Mumtaz, M. Syed, M. Al Hosani, and H. Zeineldin, "A simple and accurate approach to solve the power flow for balanced islanded microgrids," in *2015 IEEE 15th International Conference on Environment and Electrical Engineering (EEEIC)*, 2015, pp. 1852-1856.

[144] C. Li, S. K. Chaudhary, J. C. Vasquez, and J. M. Guerrero, "Power flow analysis algorithm for islanded LV microgrids including distributed generator units with droop control and virtual impedance loop," in *2014 IEEE Applied Power Electronics Conference and Exposition-APEC 2014*, 2014, pp. 3181-3185.

[145] A. H. Lone and N. Gupta, "Load Flow Analysis of Islanded Microgrids," in *2021 IEEE 4th International Conference on Computing, Power and Communication Technologies (GUCON)*, 2021, pp. 1-6.

[146] M. Z. Kamh and R. Iravani, "Unbalanced model and power-flow analysis of microgrids and active distribution systems," *IEEE Transactions on Power Delivery,* vol. 25, pp. 2851-2858, 2010.

[147] H. Nikkhajoei and R. Iravani, "Steady-state model and power flow analysis of electronically-coupled distributed resource units," *IEEE Transactions on Power Delivery,* vol. 22, pp. 721-728, 2006.

[148] !!! INVALID CITATION !!!

[149] M. M. A. Abdelaziz, H. E. Farag, E. F. El-Saadany, and Y. A.-R. I. Mohamed, "A novel and generalized three-phase power flow algorithm for islanded microgrids using a newton trust region method," *IEEE transactions on power systems,* vol. 28, pp. 190-201, 2012.

[150] F. Mumtaz, M. Syed, M. Al Hosani, and H. Zeineldin, "A novel approach to solve power flow for islanded microgrids using modified Newton Raphson with droop control of DG," *IEEE Transactions on Sustainable Energy,* vol. 7, pp. 493-503, 2015.

[151] K. Hesaroor and D. Das, "Improved Modified Newton Raphson Load Flow Method for Islanded Microgrids," in *2020 IEEE 17th India Council International Conference (INDICON)*, 2020, pp. 1-6.

[152] A. Esmaeli, M. Abedini, and M. H. Moradi, "A novel power flow analysis in an islanded renewable microgrid," *Renewable energy,* vol. 96, pp. 914-927, 2016.

[153] A. Elrayyah, Y. Sozer, and M. E. Elbuluk, "A novel load-flow analysis for stable and optimized microgrid operation," *IEEE Transactions on Power Delivery,* vol. 29, pp. 1709-1717, 2014.

[154] A. Lima-Silva, F. D. Freitas, and L. F. d. J. Fernandes, "A Homotopy-Based Approach to Solve the Power Flow Problem in Islanded Microgrid with Droop-Controlled Distributed Generation Units," *Energies,* vol. 16, p. 5323, 2023.

[155] A. Arif, Z. Wang, J. Wang, B. Mather, H. Bashualdo, and D. Zhao, "Load modeling—A review," *IEEE Transactions on Smart Grid,* vol. 9, pp. 5986-5999, 2017.

[156] J. M. Guerrero, J. Matas, L. G. de Vicuna, M. Castilla, and J. Miret, "Decentralized control for parallel operation of distributed generation inverters using resistive output impedance," *IEEE Transactions on industrial electronics,* vol. 54, pp. 994-1004, 2007.

[157] A. Gkountaras, *Modeling techniques and control strategies for inverter dominated microgrids* vol. 2: Universitätsverlag der TU Berlin, 2017.

[158] J. Kirtley Jr, "AC Power Flow in Linear Networks," *Introduction to Power Systems, Class Notes,* 2003.

[159] A. Kumar, B. K. Jha, S. Das, and R. Mallipeddi, "Power flow analysis of islanded microgrids: a differential evolution approach," *IEEE Access,* vol. 9, pp. 61721-61738, 2021.

[160] W. Stevenson Jr and J. Grainger, *Power system analysis*: McGraw-Hill Education, 1994.

[161] K. Volkov, *Computational Models in Engineering*: BoD–Books on Demand, 2020.

[162] H. Saadat, *Power system analysis* vol. 2: McGraw-hill, 1999.

[163] T. Nishikawa and A. E. Motter, "Comparative analysis of existing models for power-grid synchronization," *New Journal of Physics,* vol. 17, p. 015012, 2015.

[164] K. De Brabandere, B. Bolsens, J. Van den Keybus, A. Woyte, J. Driesen, and R. Belmans, "A voltage and frequency droop control method for parallel inverters," *IEEE Transactions on power electronics,* vol. 22, pp. 1107-1115, 2007.

[165] L. Zhang, K. Chen, S. Chi, L. Lyu, and G. Cai, "The Hierarchical Control Algorithm for DC Microgrid Based on the Improved Droop Control of Fuzzy Logic," *Energies,* vol. 12, p. 2995, 2019.

[166] N. Pogaku, M. Prodanovic, and T. C. Green, "Modeling, analysis and testing of autonomous operation of an inverter-based microgrid," *IEEE Transactions on power electronics,* vol. 22, pp. 613-625, 2007.

[167] E. A. A. Coelho, P. C. Cortizo, and P. F. D. Garcia, "Small-signal stability for parallel-connected inverters in stand-alone AC supply systems," *IEEE Transactions on Industry Applications,* vol. 38, pp. 533-542, 2002.

[168] D. Dong, B. Wen, D. Boroyevich, P. Mattavelli, and Y. Xue, "Analysis of phase-locked loop low-frequency stability in three-phase grid-connected power converters considering impedance interactions," *IEEE transactions on industrial electronics,* vol. 62, pp. 310-321, 2015.

[169] E. A. Coelho, P. C. Cortizo, and P. F. D. Garcia, "Small signal stability for single phase inverter connected to stiff AC system," in *Conference record of the 1999 IEEE industry applications conference. Thirty-forth IAS annual meeting (Cat. No. 99CH36370)*, 1999, pp. 2180-2187.

[170] J. M. Guerrero, L. G. De Vicuna, J. Matas, M. Castilla, and J. Miret, "A wireless controller to enhance dynamic performance of parallel inverters in distributed generation systems," *IEEE Transactions on power electronics,* vol. 19, pp. 1205-1213, 2004.

[171] Z. Huang, N. Zhou, F. Tuffner, Y. Chen, D. Trudnowski, W. Mittelstadt*, et al.*, "Improving small signal stability through operating point adjustment," in *IEEE PES General Meeting*, 2010, pp. 1-8.

[172] Q. Jia, G. Yan, Y. Cai, Y. Li, and J. Zhang, "Small-signal stability analysis of photovoltaic generation connected to weak AC grid," *Journal of Modern Power Systems and Clean Energy,* vol. 7, pp. 254-267, 2019.

[173] Z. Shuai, Y. Hu, Y. Peng, C. Tu, and Z. J. Shen, "Dynamic stability analysis of synchronverter-dominated microgrid based on bifurcation theory," *IEEE Transactions on Industrial Electronics,* vol. 64, pp. 7467-7477, 2017.

[174] T. Chu, M. Xu, Y. Xie, S. Wang, D. Li, and G. Liu, "Small-Signal Stability Analysis of the Power System Based on Active Support of Renewable Energy VSCs," *Frontiers in Energy Research,* vol. 10, p. 907790, 2022.

[175] Y. Yang, Y. Wang, and X. Zhang, "Research on power system small signal stability analysis and correction based on LightGBM algorithm," *Electrical Engineering,* pp. 1-18, 2024.

[176] Q. Lu, S. Mei, W. Hu, F. F. Wu, Y. Ni, and T. Shen, "Nonlinear decentralized disturbance attenuation excitation control via new recursive design for multi-machine power systems," *IEEE Transactions on Power Systems,* vol. 16, pp. 729-736, 2001.

[177] G. G. Karady, "Improving transient stability using generator tripping based on tracking rotor-angle," in *2002 IEEE Power Engineering Society Winter Meeting. Conference Proceedings (Cat. No. 02CH37309)*, 2002, pp. 1113-1118.

[178] S. Eftekharnejad, V. Vittal, G. T. Heydt, B. Keel, and J. Loehr, "Small signal stability assessment of power systems with increased penetration of photovoltaic generation: A case study," *IEEE transactions on sustainable energy,* vol. 4, pp. 960-967, 2013.

[179] D. Zhang, X. Li, D. Huang, Y. Chen, P. Li, and L. Guoi, "Average Modeling and Stability Analysis of Virtual Synchronous Generator Controlled Modular Multilevel Converters," in *2018 International Conference on Power System Technology (POWERCON)*, 2018, pp. 2902-2909.

[180] J. Xu, A. M. Gole, and C. Zhao, "The use of averaged-value model of modular multilevel converter in DC grid," *IEEE Transactions on Power Delivery,* vol. 30, pp. 519-528, 2014.

[181] M. Prodanovic, T. Green, and H. Mansir, "A survey of control methods for three-phase inverters in parallel connection," in *2000 Eighth International Conference on Power Electronics and Variable Speed Drives (IEE Conf. Publ. No. 475)*, 2000, pp. 472-477.

[182] P. M. Anderson and A. A. Fouad, *Power system control and stability*: John Wiley & Sons, 2008.

[183] C. A. Gross, "Power System Analysis. Canada: Jhon Wiley and Sons," ed: Inc, 1986.

[184] J. J. Grainger, *Power system analysis*: McGraw-Hill, 1999.

[185] M. K. Singh, S. Dhople, F. Dörfler, and G. B. Giannakis, "Time-domain Generalization of Kron Reduction," *IEEE Control Systems Letters,* vol. 7, pp. 259-264, 2022.

[186] M. Yao, S. Roy, and J. L. Mathieu, "Using Demand Response to Improve Power System Small-Signal Stability," *arXiv preprint arXiv:2304.05573,* 2023.

[187] C. M. Martini and T. J. Overbye, "Visualization of oscillation mode shapes and participation factors," *PSERC general publication,* 2000.

[188] E. W. Kimbark, *Power system stability* vol. 1: John Wiley & Sons, 1995.